2015

Time-Resolved Investigations of Continuous Flow Synthesis of Nanomaterials and Catalysis Using Millifluidic Reactors for Biomass Conversion Reactors

Chelliah V Navin
Louisiana State University and Agricultural and Mechanical College

TIME-RESOLVED INVESTIGATIONS OF CONTINUOUS FLOW SYNTHESIS OF NANOMATERIALS AND CATALYSIS USING MILLIFLUIDIC REACTORS FOR BIOMASS CONVERSION REACTIONS

A Dissertation

Submitted to the Graduate Faculty of the
Louisiana State University and
Agricultural and Mechanical College
in partial fulfillment of the
requirements for the degree of
Doctor of Philosophy

in

The Department of Engineering Sciences

by
Chelliah V Navin
B.Tech., Karunya University, 2009
M.S., Louisiana State University, 2012
August 2015

ACKNOWLEDGMENTS

First and foremost I thank the Almighty God for guiding me as per his will.

I thank my parents Mr. C Vijayanathan and Mrs. Jamuna Vijayanathan and my younger brother Aruun for their never ending love, prayers and guidance in all my endeavors.

I thank my Co-Advisors, Dr. Challa S.S.R. Kumar and Dr. Chandra S. Theegala, for the research opportunity and believing in me. Your guidance, kindness, wealth of knowledge and experience has helped my education further. You have always been awesome. Special thanks to Dr. Sai Krishna Katla for his help both as a colleague and as a friend for sharing his time and knowledge pertaining to this research. I thank Dr. James Spivey (Dept. of Chemical Engineering), Dr. David Constant (HOD, Biological and Agricultural Engineering) for their involvement in my Ph.D. committee. I also thank Dr. Justin Ragains (Dept. of Chemistry) for his involvement as the Dean's representative for this research.

I thank the following people for their support and patience in helping with my research: Dr. Steven G. Hall, Ms. Angela Singleton, Ms. Donna Elisar, Dr. Varshini Singh, Dr. Lisa Bovenkamp, Dr. Jeffery T. Miller, Dr. Soma Chattopadhyay, Dr. Tomohiro Shibata, Dr. Yaroslav Losovyj, Dr. Eizi Morikawa, Dr. Wanda LeBlanc, Evan Terrell, Dr. Dong Liu, Dr. Yang Liu (North Carolina State University – Raleigh), Dr. Amar Kambhar (University of North Carolina - Chapel Hill), Dr. Thomas J Balk & Dr. Dali Qian, (University of Kentucky – Lexington), faculty and staff of BAE, LSU and Center for Advances Microstructures and Devices (CAMD).

I thank the funding Sources. This research work was supported as part of the Center for Atomic Level Catalyst Design, an Energy Frontier Research Center funded by the U.S.

Department of Energy, Office of Science, Office of Basic Energy Sciences under Award Number DE-SC0001058 and also supported by Board of Regents under grants award number LEQSF (2009-14)-EFRC-MATCH and LEDSF-EPS(2012)-OPT-IN-15. MRCAT operations were supported by the Department of Energy and the MRCAT member institutions. The use of the Advanced Photon Source at ANL was supported by the U. S. Department of Energy, Office of Science, Office of Basic Energy Sciences, under Contract No. DE-AC02-06CH11357.

Finally, I thank my family and friends without whom my life would have been much harder. I thank all my fellow graduate and undergraduate friends and students for their help and assistance during my stay at LSU.

TABLE OF CONTENTS

ACKNOWLEDGMENTS ii

LIST OF TABLES vi

LIST OF FIGURES vii

ABSTRACT xii

CHAPTER 1: INTRODUCTION 1
1.1 Lab-on-a-chip based synthesis of nanoparticles for catalytic applications 2
1.2 Time resolved investigations for nanocatalyst synthesis using lab-on-a-chip systems 3
1.3 Objective 5

CHAPTER 2: LITERATURE REVIEW 7
2.1 Time resolved experiments using microfluidic devices 7
2.2 Time resolved investigations using millifluidic devices 11
2.3 Time resolved investigations of catalysis reactions 14

CHAPTER 3: USE OF LAB-ON-A-CHIP DEVICES FOR GOLD NANOPARTICLES SYNTHESIS AND THEIR ROLE AS A CATALYST SUPPORT 15
3.1 Introduction 15
3.2 An overview of gold catalysis and current challenges 19
3.3 An overview of flow catalysis devices 21
3.4 Tubular or plug-flow reactors 24
3.5 Lab-on-a-chip systems: Microfluidic and Millifluidics 26
3.6 LOC devices for synthesis gold nanoparticles and their catalysis 30
3.6.1 Overview of LOC synthesis of metal nanocatalysts 30
3.6.2 Synthesis of nanostructured gold catalysts using LOC devices 33
3.6.3 Gold nanocatalysts supported within LOC systems 50
3.7 Conclusions and future perspective 57

CHAPTER 4: MILLIFLUIDICS FOR CONTINUOUS FLOW SYNTHESIS AND TIME-RESOLVED IN-SITU X-RAY ABSORPTION SPECTROSCOPY INVESTIGATION OF PLATINUM-DMSA NANOPARTICLES 59
4.1 Introduction 59
4.2 Materials and Methods 61
4.2.1 Experimental section 61
4.2.1.1 Chemicals 61
4.2.1.2 Millifluidic reactor set-up 61
4.2.2 Experimental concept and design 62
4.2.2.1 Synthesis of ultra-small platinum sulfide nanoparticles using a millifluidic reactor 62
4.2.3 Instrumentation 63

4.2.3.1 X-ray absorption spectroscopy (XAS) 63
4.2.3.2 High Resolution Transmission Electron Microscopy 65
4.2.3.3 X-ray photoelectron spectroscopy (XPS) 65
4.2.3.4 UV-Visible spectroscopy (UV-Vis) 68
4.2.3.5 X-ray diffraction (XRD) 68
4.2.3.6 Fourier Transform Infrared Spectroscopy (FT-IR) 68
4.3 Results and discussion 69
4.4 Conclusions 80

CHAPTER 5: MILLIFLUIDICS FOR TIME-RESOLVED CONTINUOUS FLOW OXIDATION OF 5-(HYDROXYMETHYL)FURFURAL TO 2, 5-FURANDICARBOXYLIC ACID AT AMBIENT CONDITIONS 82
5.1 Introduction 82
5.2 Materials and Methods 85
5.2.1 Experimental section 85
5.2.2.1 Chemicals 85
5.2.2.2 Millifluidic platform set-up 85
5.2.2.3 Catalysis experiments 85
5.2.2.4 Gold catalyst 86
5.2.2.5 Continuous flow oxidation of HMF using millifluidic reactor 86
5.2.2.6 Batch mode oxidation of HMF 86
5.2.2.7 UV-Visible spectroscopy (UV-Vis) 87
5.2.2.8 High Pressure Liquid Chromatography 87
5.3 Results and Discussion 87
5.3.1 HMF oxidation using continuous flow millifluidic reactor 87
5.3.2 HMF oxidation using batch reactor 94
5.3.3 Effect of pressure, temperature, amount of base and catalyst 97
5.4 Conclusions 99

CHAPTER 6: FINAL CONCLUSION 101

REFERENCES 103

APPENDIX 124

VITA 127

LIST OF TABLES

Table 4.1: Calculated atomic percentage concentrations of Pt and S 67

Table 4.2: Results of the EXAFS Analysis Pt L_3-edge for sample investigated at zone 1 72

Table 4.3: Peaks fitting parameters for Pt 4f region 80

Table 4.4: Peaks fitting parameters for sulfur 2p region 80

Table 5.1: Percentage of HMF converted and HMFCA and FDCA detected at different zones of the millifluidic reactor channel 92

Table 5.2: Percentage of HMF converted and HMFCA and FDCA detected using batch reactor as a function of time.....96

Table 5.3: Rate of formation of products and turnover frequency of the reaction using the millifluidic reactor and flask reactor.....97

LIST OF FIGURES

Figure 1.1: In-situ X-ray absorption spectroscopy (XAS) analysis of the Ultra small copper nanoclusters at the outlet of the reactor 5

Figure 2.1: Schematic principle of the in situ XAFS experimental set-up using a microfluidic cell. Fluorescence yield spectra recorded at positions (x, y) along a microreactor channel provide time-dependent XAFS spectra. In the present reaction, precursor flows (TOP-Se and Cd stock solution) are mixed before introducing to a heated microchannel.....8

Figure 2.2: Picture of the microreactor system used by Zinoveva et.al. The points are marked where in-situ XANES spectra were taken 8

Figure 2.3: X-ray beam paths through the microreactor channel. Monochromated X-rays are focused through the window wafer's nitride membrane and into the observation channel of the channel wafer at a 45° angle to the direction of flow. X-ray fluorescence is monitored at a 90° angle to the incident radiation. Due to the 45° angle of incidence, a channel with height h and linear particle velocity V has a time resolution of h/V 9

Figure 2.4: Continuous flow microfluidic reactor used for observation of CdS-Cys NC synthesis at the boundary between two laminar flowing streams. (a) Sketch of microfluidic device (channel width exaggerated); w = 100 mm, L = 2 cm, depth 2h = 20 mm 10

Figure 2.5: Experimental setup for particle synthesis in continuous-flow mode coupling a microstructured static mixer directly to SAXS-analysis in a flow cell.....11

Figure 2.6: TEM results of Au nanoclusters obtained at a) 10 mLh^{-1}, location 1-B11, b) 10 mLh^{-1}, location 2-B12, c) 10 mLh^{-1}, outlet, d) 6 mLh^{-1}, location 1-B21, e) 6 mLh^{-1}, location 2- B22, f) 6 mLh^{-1}, outlet, g) 2 mLh^{-1}, location 1- B31, h) 2 mLh^{-1}, location 2- B21, i) 2 mLh^{-1}, outlet. The bar at the bottom of each picture 5 nm to scale except for (d) where it is 2 nm.....12

Figure 2.7: A schematic representation of the millifluidic platform for the synthesis of UCNCs along with the reaction scheme.....13

Figure 2.8: Schematic showing the different stages of spatially (and time) resolved growth process of gold nanostructures within the millifluidic chip.....13

Figure 2.9: IR absorption microspectroscopy scans along the flow reactor.....14

Figure 3.1: Pictorial representation of using millifluidic reactor for the synthesis and coating of nanoparticles simultaneously.....16

Figure 3.2: A schematic representation of the two types of process for preparing nanocatalysts for flow catalysis. (A) IFC process and (B) CFC process 17

Figure 3.3: A schematic representation of the over view of the direction the field of gold catalysis is moving: from bulk catalysis to atomically precise catalysis 20

Figure 3.4: Layer by layer design of both platforms integrating the LTCC microreactor. (A) Thermal platform; (a) top layer (4×); (b) screen-printed heater (1×); (c) bottom layer (4×). (B) Picture of the thermal platform fabricated. (C) Microfluidic platform; layers (a and f) were fabricated by duplicate; the microfluidic structure was embedded at layer (e). (D) Picture of the microfluidic platform, which includes an exposed section regarding the micromixer.....24

Figure 3.5: Examples of (a) metal, (b) glass/glass, and (c) silicon/Pyrex and microreactors.....28

Figure 3.6: Schematic illustration of reactant feed into the LOC device. Modular microreactor arrangement for flow-through process.....31

Figure 3.7: A gold nanoparticle seed suspension (S) and aqueous reagent solutions (R1 and R2) are separately delivered into one arm of a microfluidic T-junction, and silicone oil is delivered into the other arm. Droplets are pinched off at the T-junction. Reagents and seeds are rapidly mixed by chaotic advection. The oil forms a thin lubricating layer around the translating droplets, and prevents contact between growing particles and the microchannel walls.....32

Figure 3.8: The integrated millifluidic reactor used for gold nanoparticle synthesis and functionalization is shown. (a) Diagram and picture of the rector for AuNPs synthesis. The reactor is composed of multiple modular commercially available components, and fluid flow is driven by the peristaltic pump. (b) In this reactor, mixing of the growth solution and the seed/borohydride solution occurs in a simple polyethylene Y-mixer. (c) The reactor also features an integrated flow-based purification system, in which a commercially available tangential flow filtration cartridge can be attached to an additional peristaltic pump in order to integrated high-throughput approach for nanoparticle purification or functionalization.....36

Figure 3.9: Schematic diagram for the synthesis of PVP-Stabilized Au clusters in a micromixer 38

Figure 3.10: (a) Three dimensional schematic of a radial interdigitated mixer. Each mixer is fabricated in 3-layers. In the first two layers input flows are directed to two circular bus channels which, in turn, split the flow into 8 identical fluid laminae and deliver reagent streams towards a central mixing chamber. The final layer acts as a cap to enclose channels and as a guide for input and output capillaries. The output is from the center of the uppermost layer. (b) Photograph of the fabricated mixer. Microchannels are filled with dye solutions to show different shadings for the different channels.....39

Figure 3.11: Experimental setup for particle synthesis in continuous-flow mode coupling a microstructured static mixer directly to SAXS-analysis in a flow cell.....41

Figure 3.12: Schematic illustration of the millifluidic reactor channel 41

Figure 3.13: Schematic for the formation steps of gold structures within millifluidic reactor.....42

Figure 3.14: (a) Millifluidic chip marked with different zones where in situ XAS was performed. (b) In-situ XAS analysis at different zones within the millifluidic channel. (c) Reaction scheme of precursors.....43

Figure 3.15: Schematic of the experimental setup showing the connectivity of the microreactor (STATMIX 6, area 22 x 14 mm) 45

Figure 3.16: The hydrophobic microchannel (water is the dispersed phase). Fluorescein was added to the aqueous phase to improve the optical resolution.....46

Figure 3.17: Schematic of the experimental setup for the production of gold nanoparticles 47

Figure 3.18: Illustration of the experimental setup. The mixer can be a pressed Teflon tube (millifluidic mixer) (7 or 22 cm length) (left), a Ball-Berger mixer (not shown) or a microfluidic mixer with a butterfly geometry (right) 49

Figure 3.19: The devices with three inlets each connected to a pump, and the in-line ATR-IR and/or UV-Vis flow-cells connected to the outlet 49

Figure 3.20: Micro continuous flow setup (feedstock 1: bis-α-H-ketone solution, feedstock 2: propargylamine solution; M: micro mixer; PBCR1, PBCR2: packed bed capillary reactors (ID: 1mm, 50cm length); P: pressure sensor; T1, T2: temperature sensors; S1, S2: syringe pumps). Inlay: image of the PBCRs 51

Figure 3.21: Flow chemistry set-up schemes for the different reaction regimes A–C. P1, P2 pumps; P(1) pressure sensor; T(1), T(2) temperature sensors; PBCR1 (Montmorillonite K-10) and PBCR2 (Au-NP@Al_2O_3): packed-bed capillary reactors; BPR: back-pressure regulator.....52

Figure 3.22: Microreactor, reactor assembly with temperature control and the schematic of the experimental setup 53

Figure 3.23: Parts of the microreactor showing the microchannel plate coated with a thin film of nanoparticulated ceria 54

Figure 3.24: Immobilization of the gold catalyst. a) Reduction of the cyano group to an amine. b) Preparation of microencapsulated gold. c) Immobilization of the gold catalyst 55

Figure 3.25: Experimental setup of the gold-catalyzed oxidation reactions.....55

Figure 3.26: Schematic of the process (side view). A microfluidic channel with gold nanoparticles attached to a glass support; fluid flows from left to right. (Top) A laser at or near the frequency of the plasmon resonance of the gold nanoparticles is focused on the top of the support, and the subsequent heat generated in the nanoparticles is transferred to the surrounding fluid and forms vapor. The vapor phase components react on the catalyst forming gas bubbles which are carried downstream. (The channel height is 40 μm and the radius of the nanoparticles is ~10 nm).....56

Figure 4.1: Pt(DMSA) nanoparticle k-space EXAFS data (not phase corrected) 64

Figure 4.2. At the close to normal take off angles the shell related signal is larger than at the grazing angles 67

Figure 4.3: Schematic representation of Pt(DMSA) nanoparticles synthesis in a millifluidic reactor chip.....69

Figure 4.4: Pt L_3-edge XANES spectra: Reference H_2PtCl_6 (red), Experimental spectra of Pt(DMSA) obtained at zones 1 and 7 (green and black, respectively), Standard Pt foil (dark yellow), Theoretically calculated reference PtS (blue).....70

Figure 4.5: Pt L_3-edge FT EXAFS spectra of experimental Pt(DMSA) nanoparticles and theoretical platinum sulfide (PtS) from crystal structure.....72

Figure 4.6: UV-Vis spectrum of H_2PtCl_6 (precursor) and Pt(DMSA) nanoparticles colloid indicating the reduction of $[PtCl_6]^{2-}$ ions.....74

Figure 4.7: a) HRTEM image of the quenched Pt(DMSA) nanoparticles. (b) HRTEM image of the unquenched Pt(DMSA) nanoparticles (c) HRTEM image of Pt(DMSA) nanoparticles with clearly visible lattice fringes passivated by Pt and S atoms, (d) HRTEM image of a single Pt(DMSA) nanoparticle with lattice spacing of 2.4 Å, (e) Corresponding size histogram of Pt(DMSA) nanoparticles.....75

Figure 4.8: (a) EDS spectra of the nanoparticles formed after reduction with DMSA showing the presence of both Pt and S; (b) and (c): STEM-EDS images of Pt (left) and S (right) confirming the passivation of Pt and S atoms throughout the sample. The white areas in both images represent the unreacted Pt and S precursor atoms passivated over the crystalline Pt(DMSA) nanoparticles respectively; (d) XRD spectra of the purified Pt(DMSA) nanoparticles.....76

Figure 4.9: SEM image of the Pt(DMSA) microstructures formed within the walls of the millifluidic rector chip after 9 h reaction.....77

Figure 4.10: (a) FTIR spectra of Pt(DMSA) colloidal nanoparticles, b) H_2PtCl_6 and DMSA powder mixture, c) DMSA. Inset shows the expanded version of the –SH– stretching in H2PtCl6-DMSA mixture (blue) and DMSA (pink). The absence of this stretching in spectrum (a) confirms Pt-S bond formation.....78

Figure 4.11: (a) Survey XPS scan of the Pt(DMSA) nanoparticles drop casted onto native SiO_2 surface of the Si(111) wafer. (b) High resolution Pf 4f XRS spectra, black line represents experimental data, red line – generated fit curve, green – Pt^{2+} 4f doublet, blue – Pt^{4+} oxide doublet. (c) High resolution S 2p XPS spectra, blue line $2p_{3/2}$ component, green line – $2p_{1/2}$ component.....79

Figure 5.1: Schematic representation of oxidation of HMF to FDCA using a millifluidic reactor chip coated with nanostructured gold catalyst.....87

Figure 5.2: UV-Vis spectra of the reaction mixtures collected at different zones of the millifluidic reactor channel by dissecting the chip.....88

Figure 5.3: HPLC of the reaction mixtures collected at different zones of the millifluidic reactor channel.....90

Figure 5.4: HMF Oxidation pathway leading to FDCA with HMFCA as the intermediate product 91

Figure 5.5: HMF Oxidation pathway leading to FDCA with DFF as the intermediate product 92

Figure 5.6: Oxidation of HMF to FDCA using a millifluidic reactor chip coated with nanostructured gold catalyst 93

Figure 5.7: Oxidation of HMF to FDCA using flask with gold nanoparticles 96

ABSTRACT

Millifluidics can be used as a simple tool and convenient platform to perform in-situ investigations on nanoparticles synthesis to generate real-time information in a continuous flow fashion. These investigations can be used to observe the relationship between the structure and performance of nanoparticles for catalytic applications as a function of space and time. These improvements in nanoparticles research offer unique advantages to develop catalysts with molecular strategies. In order to showcase these advantages of the millifluidic reactors, here we:

A. Extensively covered a complete literature review on Lab-on-a-chip devices for gold nanoparticle synthesis and as a catalyst support for continuous flow catalysis. This first phase of the work provides detailed information on the synthesis and catalysis applications of nanostructured gold using the lab-on-a-chip systems.

The second phase is an experimental investigation, where the millifluidic reactor was used for:

B. Continuous flow process for production of water-soluble Platinum-Dimercaptosuccinic acid (Pt(DMSA)) nanoparticles at ambient conditions. The process development was based on in-situ synchrotron radiation-based X-ray absorption spectroscopy (XAS) investigations. The XAS revealed that the nucleation and growth of the Pt(DMSA) nanoparticles was extremely fast. Such a fast nucleation and growth process was also found to hinder coating of the channel walls, except at the zone 1 where the reactants first interact.

C. Catalytic oxidation of 5-(Hydroxymethyl)furfural (HMF) to 2,5-Furandicarboxylic acid (FDCA) with nanostructured gold catalyst using millifluidics. The conversion leading from

the reactant to primary and secondary products within the millifluidic reactor was analyzed at various spatial intervals to understand the reaction mechanism. The entire process was carried out using an aqueous phase oxidizing agent, tert-Butyl hydroperoxide (TBHP) at ambient temperature and pressure in a continuous flow conditions. The turnover frequency for the catalytic oxidation of HMF using the millifluidic reactor was obtained in the order of 10^{-26} molecules s^{-1} in for HMFCA and FDCA after 50 minutes. The results demonstrated in this work highlight significant advantages in carrying out time-resolved continuous flow catalytic reactions using millifluidic reactors.

CHAPTER 1: INTRODUCTION

Catalysts play a significant role in numerous applications by promoting energy in a local environment, therefore establishing a chemical reaction (Thomas and Thomas, 1997). Several scientific investigations specifically on the catalyst's electronic structure and chemical properties have led to the evolution of nanocatalysts (Parak et.al., 2003; Murray et. al., 2000; Goswami et.al., 2014; Wang et.al., 1998; Saliba et.al., 1998; Sault et.al., 1986). The nanocatalysts involve the use of nanoparticles due to their high surface area to volume ratio and their use in chemical applications have seen a rapid growth in the last three decades (Richards et.al., 2011; Schmid et.al., 2012). Nanoparticles exhibit unique catalytic activity due to their distinct electronic and physical properties which is different from their bulk counterparts (Haruta et.al., 2003). Over the years, several synthetic techniques have been reported for producing nanoparticles for catalysis with high activity, selectivity and stability. All the techniques require appropriate reactor conditions in order to obtain nanoparticles with controlled surface composition, size, shape, structure, spatial distribution, and electronic structure (An and Smorjai, 2012; Xia et.al., 2009). Failure to maintain appropriate reactor conditions during nanoparticle synthesis will result in inefficient product, therefore leading to poor catalytic performance due to their physico-chemical properties at the nanometer scale. In this regard, scientific improvements in experimental and computational approaches have brought new breakthrough in the controlled synthesis and characterization of nanoparticles. For example, with the invention of the LOCs, it has become easier to maintain and control proper reaction conditions for the synthesis of nanoparticles (Elvira et.al., 2013; Philips et.al., 2014; Krishna et.al., 2013; Song et.al., 2008; Marre et.al., 2010; Edel et.al., 2002; Merkocia and Kutter, 2012). Due to their high signal-to-noise ratio and ease of handling, experimental characterization and computational modeling using the LOCs

have increased the potential to develop nanoparticles with atomic precision (Biswas et.al., 2012). These systems have led scientists to discover the electronic and chemical properties of the atoms and eliminate variations in their reaction dynamics during nanoparticles synthesis (Viefhus et.al., 2012; Teste et.al., 2011; Li et.al., 2912; Krishna et.al., 2013; Krishna et.al., 2013). Furthermore, the LOCs offer the capability to analyze a particular sample in-situ i.e. exactly where the nanoparticles are generated rather than being taken out of the reaction system and transported to a large laboratory facility for further investigation. In addition, these systems provide an interactive environment for researchers to unravel the nanoparticles synthesis in real time as well as accurately model the reaction mechanisms with time resolution as short as 10^{-16} seconds (Wang et.al., 2014). There is a potential scope for reaction scale-up as well as for automation using these devices and can be utilized for any type of scientific experiments provided appropriate reaction conditions are identified.

1.1 Lab-on-a-chip based synthesis of nanoparticles for catalytic applications

Colloidal nanoparticle synthesis through a wet chemical reduction method has shown the highest potential for catalyst design by providing a way to tune size and shape of the particle during the reaction which generally comprise of the following process viz. nucleation and particle growth (Dushkin et.al., 1993; O'Malley and Snook, 2003; Auer and Frenkel, 2001; Sear, 2006; Cacciuto et.al., 2004). Fast nucleation rate and colloidal stability is always desired during wet chemical reduction method in order to prepare well-defined and morphology controlled nanoparticles (Waseda and muramatsu, 2004). By using a wet chemical synthesis method in a LOC platform, the aforementioned advantages can be achieved in a steady state with better control over the reagent addition, mixing and reproducibility compared to the traditional flask

processes. The LOCs use lesser quantity of reagents and have control over the residence time of the fluids within their channels for rapid mixing and efficient heat and mass transfer. There are many reports and demonstrations on the synthesis of nanoparticles within these confined continuous flow based LOCs such as microfluidics and nanofluidics (Philips et.al., 2014; Song et.al., 2008; Merkocia and Kutter, 2012; Biswas et.al., 2012). However, the inability to scale up reagent volumes due to geometric constraints and pressure development within the microfluidic reactor channels at higher flow rates has limited their usage for nanoparticles synthesis. Also, these devices require expensive fabrication techniques such as lithography, etching, etc. as well as complicated reactor designs in order to control the nanoparticle's size and size distribution. Since there are difficulties in manipulating the fluids with high pressure due to constraints in their geometry, the demerits of microfluidics and nanofluidics are being overcome with millifluidics devices (Li et.al., 2012). Millifluidic reactors are inexpensive and easy to fabricate and offer similar control over microfluidic reactors for nanoparticles synthesis. These devices can withstand high pressures and can achieve higher flow rates, thereby creating shorter residence times with a possibility to generate nanoparticles of various morphology and dimensions (Biswas et.al., 2012; Li et.al., 2012; Krishna et.al., 2013). Moreover, due to their channel dimensions, the millifluidic devices have the capability to offer more generalized and efficient platform for time-resolved kinetic studies with higher signal-to-noise ratio than what has been possible so far with microfluidics.

1.2 Time resolved investigations for nanocatalyst synthesis using lab-on-a-chip systems

The use of LOCs for time resolved investigation is a hot topic in current scientific research community for their ability to combine multiple techniques such as synthesis and

characterization of nanomaterials in a single step (Hinsmann et.al., 2001; Schwarz et.al., 2014). Unlike traditional flask based synthesis, the LOCs offer a unique capability to probe scientific instruments to resolve a continuous flow chemical reaction within its confined channel at different spatial intervals with time resolution (Biswas et.al., 2012; Li et.al., 2012; Krishna et.al., 2013). Time resolved measurements using the LOCs are generally carried out using spectroscopic instruments such as X-ray absorption spectroscopy (Biswas et.al., 2012), Fourier Transform Infrared spectroscopy (Schwarz et.al., 2014) etc. These instruments when coupled to the LOCs, can monitor and resolve the dynamics of a chemical process as a function of time (time resolved) (Krishna et.al., 2012) or frequency (frequency resolved) (Gorocs and Ozcan et.al., 2013). The spectral results are obtained either at a single energy or at multiple energy range depending on the absorbance, transmittance, reflectance or electron scattering property of the atom being analyzed over discrete time intervals. It is very crucial to select the correct functions and characterization tools before carrying out a chemical process because there are tremendous possibilities that may lead to no results. A pictorial depiction of the use of an in-situ XAS coupled to a millifluidic reactor to investigate the time resolved synthesis of colloidal nanoparticles is shown in Figure 1.1 (Biswas et.al., 2012).

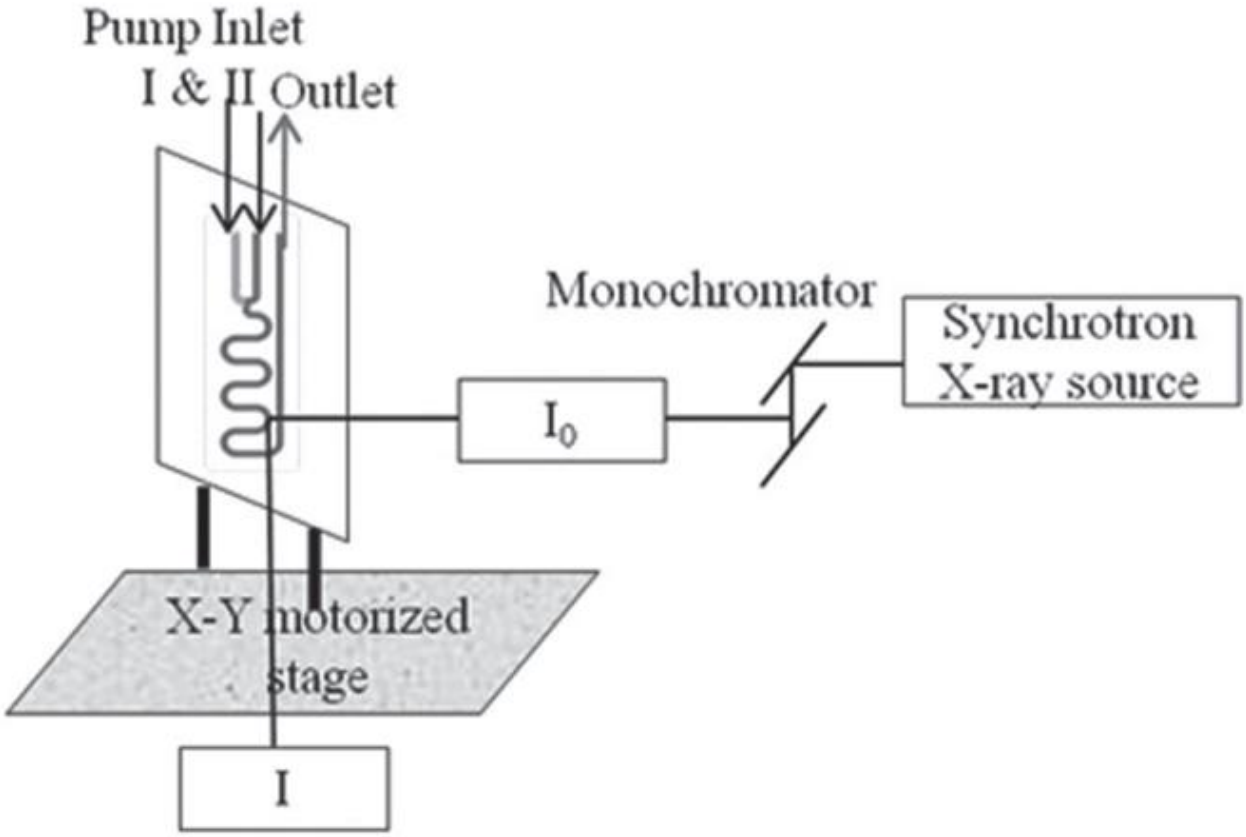

Figure 1.1: In-situ X-ray absorption spectroscopy (XAS) analysis of the Ultra small Copper Nanoclusters at the outlet of the reactor. (Reproduced with permission from Ref. Biswas et. al., Copyright Wiley-VCH Verlag GmbH & Co. KGaA, 2012).

1.3 Objective

The objective of this research is to expand the capability of the millifluidic reactor to carry out time-resolved investigations on the synthesis of various catalytic materials other than gold and demonstrate its utility for biomass conversion reaction catalyzed at ambient temperature and pressure. The first phase of this work will:

A. Extensively cover a complete literature review on Lab-on-a-chip devices for gold nanoparticle synthesis and their role as a catalyst support for continuous flow catalysis.

The second phase will be an experimental investigation, where the millifluidic reactor will be used to carry out time resolved investigations for:

B. Continuous flow Synthesis of platinum sulfide nanoparticles

C. Continuous flow Au catalysis of 5-Hydroxymethyl furfural (HMF) to 2,5-Furandicarboxylic acid (FDCA) as a model reaction for biomass conversions.

CHAPTER 2: LITERATURE REVIEW

2.1 Time resolved experiments using microfluidic devices

Time resolved experiments are useful during nanoparticles synthesis to investigate fundamental properties of atoms with spatial resolution using the LOCs (Biswas et.al., 2012; Krishna et.al., 2013). These experiments can be performed ranging as short as millisecond to femtosecond on atoms with very short lived electronic states. This advancement has facilitated time resolved investigation using the LOCs to drastically evolve for nanoparticles synthesis studies. However, relatively little has been done on the time resolved investigations for nanoparticles synthesis using the LOCs so far. Few investigations have been performed using the microfluidic reactor coupled with spectroscopic tools such as X-ray absorption spectroscopy (XAS) to investigate the growth of nanoparticles (Biswas et.al., 2012; Krishna et.al., 2013). With the evolution of synchrotron based XAS, it is now possible to perform real time in-situ investigations on nanoparticles during synthesis along the LOCs channel. The acquired XAS data is later Fourier transformed to deliver information on the chemical kinetics and bonds on the chemical reaction. Oyanagi et.al. successfully demonstrated the use of micromixer to investigate the bond formation kinetics using in-situ X-ray absorption fine structure (XAFS) to monitor the growth of CdSe particles (Oyanagi et.al., 2011). They performed the experiment using a microfluidic cell coupled with in-situ XAFS apparatus to probe the reaction in real time at discrete time intervals of 30 s. Their investigation indicated the presence of CdSe particles in amorphous state during the initial stages of the reaction, therefore contradicting the hypothesis of the classical nucleation theory. Figure 2.1 illustrates the micromixer set-up used for time dependent studies by Oyanagi and his coworkers.

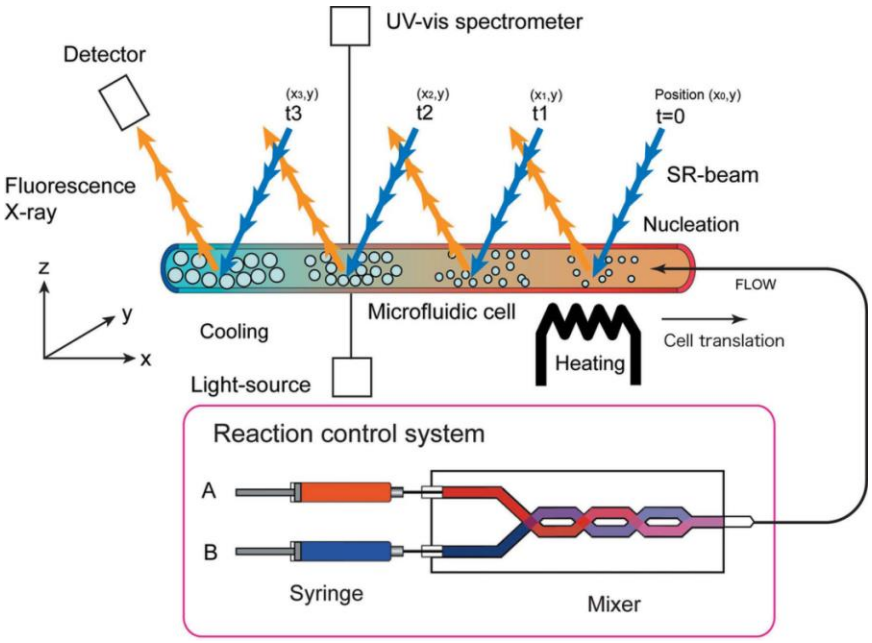

Figure 2.1: Schematic principle of the in situ XAFS experimental set-up using a microfluidic cell. Fluorescence yield spectra recorded at positions (x, y) along a microreactor channel provide time-dependent XAFS spectra. In the present reaction, precursor flows (TOP-Se and Cd stock solution) are mixed before introducing to a heated microchannel. (Reproduced with permission from Ref. Oyanagi et.al., Copyright International Union of Crystallography, 2011).

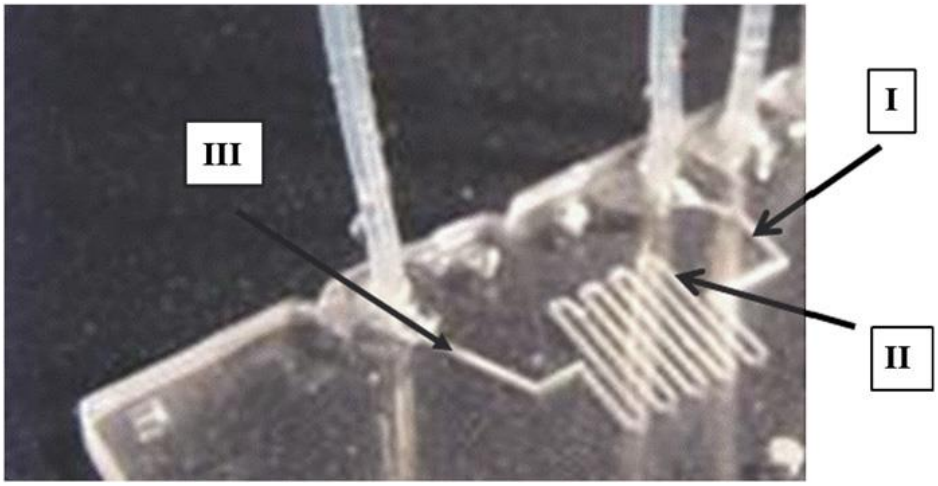

Figure 2.2: Picture of the microreactor system used by Zinoveva et.al. The points are marked where in-situ XANES spectra were taken (Reproduced with permission from Zinoveva et.al., Copyright Elsevier, 2007).

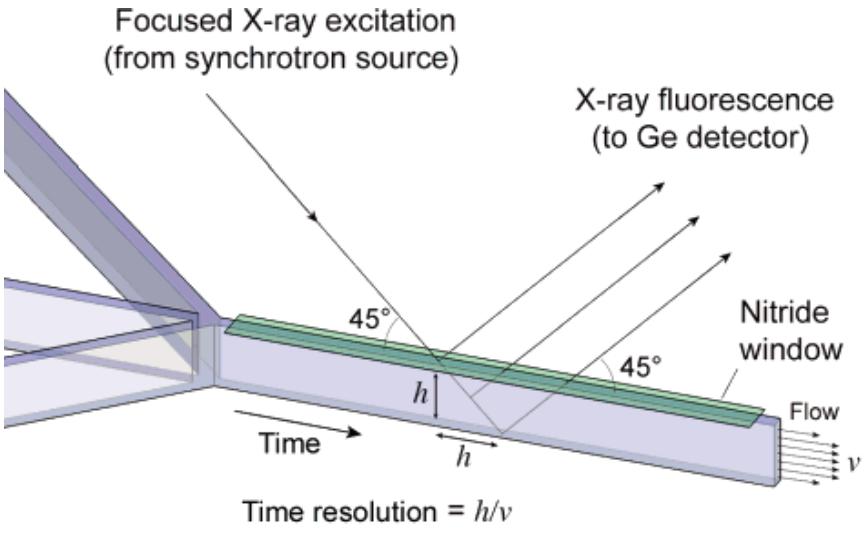

Figure 2.3: X-ray beam paths through the microreactor channel. Monochromated X-rays are focused through the window wafer's nitride membrane and into the observation channel of the channel wafer at a 45° angle to the direction of flow. X-ray fluorescence is monitored at a 90° angle to the incident radiation. Due to the 45° angle of incidence, a channel with height h and linear particle velocity V has a time resolution of h/V. (Reproduced with permission from Ref. Chan et.al., Copyright ACS Publications, 2007).

Zinoveva et.al, reported in-situ X-ray absorption near edge spectroscopy (XANES) investigation of cobalt nanoparticles synthesis using a microreactor system as shown in Figure 2.2. The changes in the reaction dynamics during the cobalt nanoparticles synthesis were observed with time resolution in the order of milliseconds by measuring the XANES spectra at various points along the microreactor (Zinoveva et.al., 2007). Similarly, Chan et.al, demonstrated the use of microfluidic reactor to investigate the kinetics of CdSe-to-Ag_2Se nanocrystal cation exchange reaction using in-situ micro-XAS at different spatial coordinates with millisecond time resolution (Chan et.al., 2007). Their investigation highlighted the applicability of in-situ X-ray synchrotron technique to study the chemical transformation of nanomaterials using flow focused LOCs as shown in Figure 2.3. Another study by Sournat et.al. showed the spatially resolved examination of cysteine-capped CdS quantum dot nanocrystals synthesis between two interdiffusing reagent streams using a microfluidic reactor at continuous flow conditions. They

performed the experiments using the microreactor with photoluminescence imaging and spectroscopy to acquire the kinetic and mechanistic data on CdS-Cys nanoparticles. Their investigation revealed a binary shift in the nanoparticle emission spectrum and showed that the nanoparticle nucleation was diffusion limited which occurred at the boundary between the two laminar streams on a longer time scale as depicted in Figure 2.4 (Sournat et.al., 2007). Likewise, Polte et.al. used a microstructured static mixer to prepare gold nanoparticles under continuous flow conditions. They used an in-house small angle X-ray scattering setup to characterize and screen the gold nanoparticles synthesized within the micromixer with time resolution. Their results were the first to show the use of continuous flow small angle X-ray scattering technique to carry out time resolved investigation of gold nanoparticles formation without the use of synchrotron facility (Polte et.al., 2010). Figure 2.5 illustrates the continuous flow mode microstructured static mixer set-up for time dependent investigation using small angle X-ray scattering (SAXS) by Polte and his coworkers.

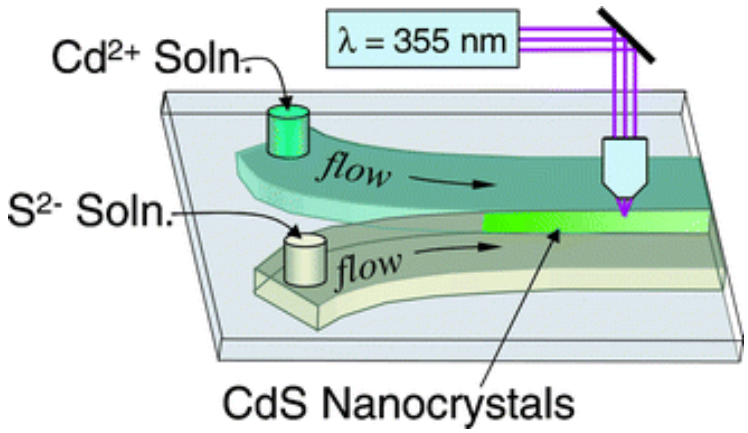

Figure 2.4: Continuous flow microfluidic reactor used for observation of CdS-Cys NC synthesis at the boundary between two laminar flowing streams. (a) Sketch of microfluidic device (channel width exaggerated); w = 100 mm, L = 2 cm, depth 2h = 20 mm. (Reproduced with permission from Ref. Sournat et.al., Copyright RSC Publishing, 2007).

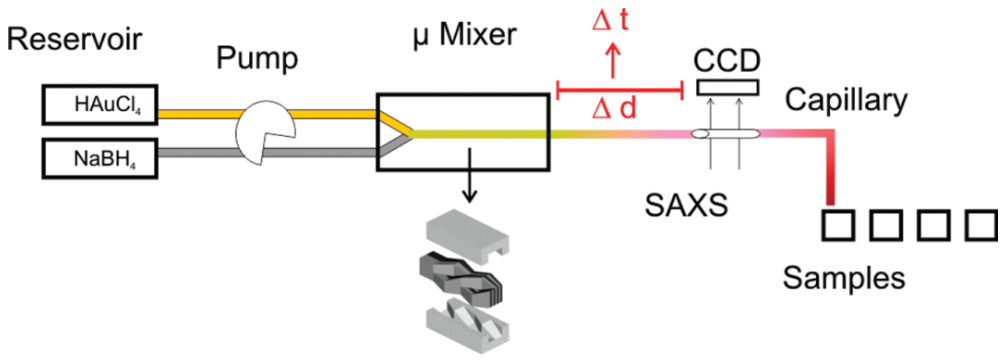

Figure 2.5: Experimental setup for particle synthesis in continuous-flow mode coupling a microstructured static mixer directly to SAXS-analysis in a flow cell. (Reproduced with permission from Ref. Polte et.al., Copyright ACS Publications, 2010).

2.2 Time resolved investigations using millifluidic devices

Although the above reports demonstrate the synthesis of nanoparticles using microfluidic reactors, the use of millifluidic devices have started to gain importance due to the possibility to have higher concentrations that will enable a better signal-to-noise ratio as well as for the possibility to dissect their channels to collect samples for time resolved investigations. Li et.al. developed a novel technique to examine the time resolved growth of gold nanoparticles using a millifluidic chip at various spatial distributions (Li et.al., 2012). The colloidal samples of gold nanoparticles were collected by dissecting the millifluidic chip at different spatial intervals and examined using transmission electron microscope (TEM) as shown in Figure 2.6; therefore taking advantage of the possibility to convert spatially resolved information into time resolved information. Their investigation involved numerical simulations to predict the dependence of flow rates in order to control the size and size distribution of the gold nanoparticles within the channel of the millifluidic reactor. Similarly, Biswas et.al. demonstrated a reproducible, high throughput and controlled synthesis of ultra-small copper nanoclusters using the millifluidic reactor as shown in Figure 2.7 (Biswas et.al., 2012). In addition, their numerical simulated

results supported their experiments results, therefore showing the capability of the millifluidic reactor to bridge the gap between theoretical and experimental investigations of nanoparticles of size less than 10 nm. The ultra-small copper nanoclusters were characterized using in-situ XAS and TEM. Another investigation by Krishna et.al. showed the use of the millifluidic chip reactor to demonstrate the time resolved mapping of the growth of gold nanostructures within its channel using in-situ XAS with a time resolution of 5 ms (Krishna et.al., 2013). Their investigation also explored the changes in the morphology of the gold nanostructures coated on the millifluidic reactor channel at different time intervals using scanning electron microscope as shown in Figure 2.8. In addition, they demonstrated that the gold nanostructures coated within the millifluidic reactor channel were catalytically active for 4-nitrophenol to 4-aminophenol reaction, therefore proving the potential of the millifluidic reactor for time resolved analysis of catalytic reactions.

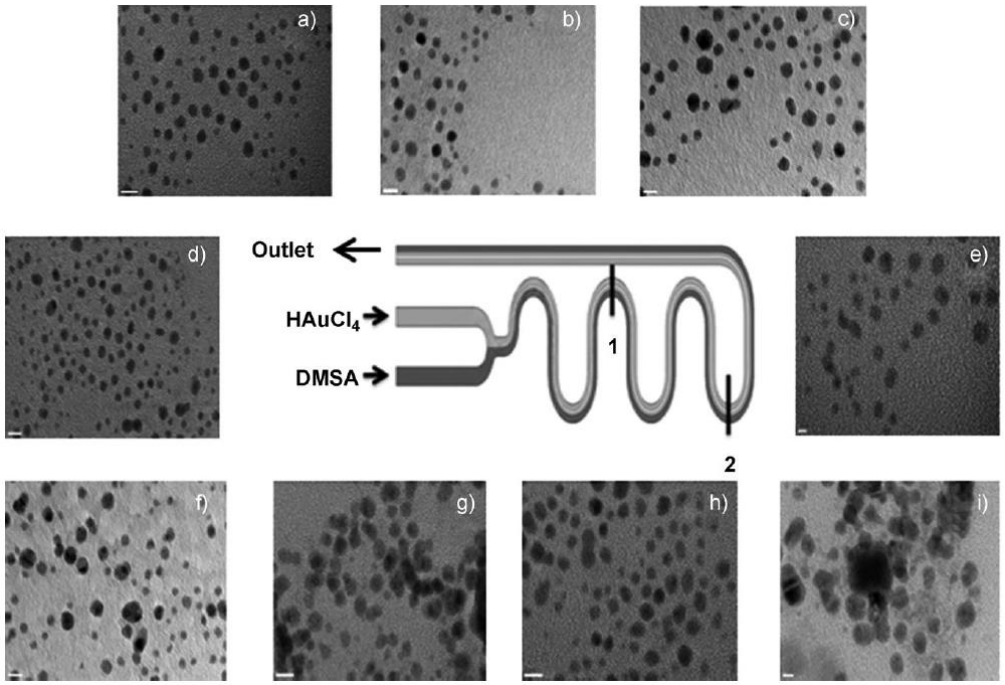

Figure 2.6: TEM results of Au nanoclusters obtained at a) 10 mLh^{-1}, location 1-B11, b)10 mLh^{-1}, location 2-B12, c) 10 mLh^{-1}, outlet, d) 6 mLh^{-1}, location 1-B21, e) 6 mLh^{-1}, location 2- B22, f) 6 mLh^{-1}, outlet, g) 2 mLh^{-1}, location 1- B31, h) 2 mLh^{-1}, location 2- B21, i) 2 mLh^{-1}, outlet. The bar at the bottom of each picture 5 nm to scale except for (d) where it is 2 nm. (Reproduced with permission from Ref. Li et.al., Copyright Wiley-VCH Verlag GmbH & Co. KGaA, 2012)

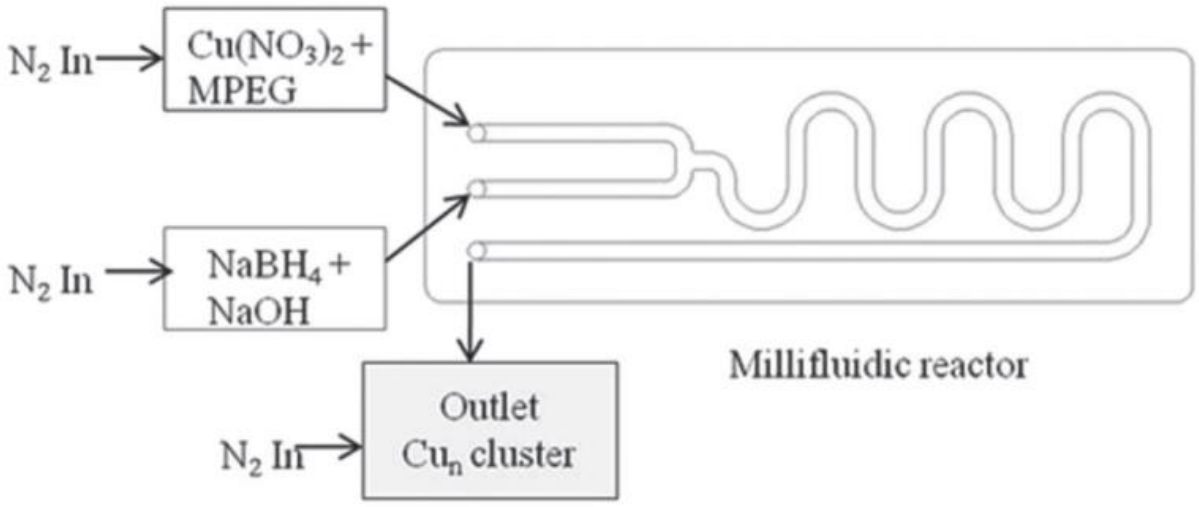

Figure 2.7: A schematic representation of the millifluidic platform for the synthesis of UCNCs along with the reaction scheme. (Reproduced with permission from Ref. Biswas et.al., Copyright Wiley-VCH Verlag GmbH & Co. KGaA, 2012)

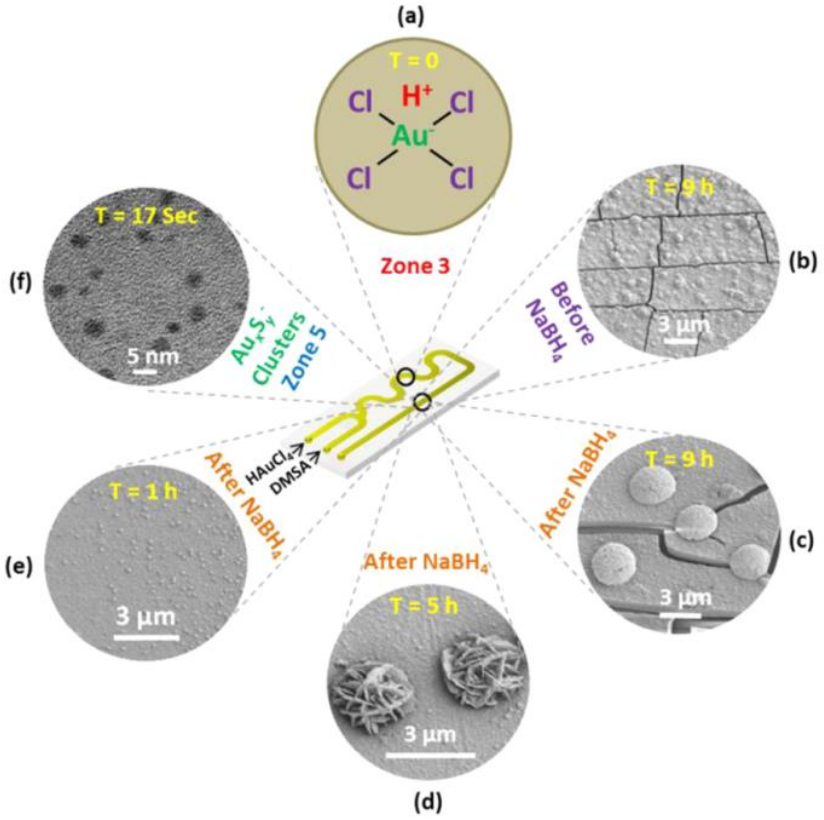

Figure 2.8: Schematic showing the different stages of spatially (and time) resolved growth process of gold nanostructures within the millifluidic chip. (Reproduced with permission from Ref. Krishna et.al., Copyright ACS Publications, 2013)

2.3: Time resolved investigations of catalysis reactions

In addition to nanoparticles synthesis for catalytic applications, the LOC based systems such as microfluidics and millifluidics, can facilitate convenient nanoparticles loading into their system (Wang, et.al., 2009; Adelman et.al., 2009; Abahmane et.al., 2009; Cao et.al., 2011), therefore providing an easy way to examine the kinetics of a catalysis reaction in-situ. It should be noted that while investigating a catalytic reaction, most ex-situ time resolved experiments lose track of reaction dynamics once the samples are taken out of the reaction system therefore limiting the identity of the species in real time. However, with the possibility to load nanoparticles into the LOCs, time resolved kinetic information on the catalytic reactions can be obtained at various spatial intervals along its channel. Furthermore, high product selectivity and recyclability can be achieved using these systems, therefore enhancing the sustainability of a catalyst. For example, Gross et.al. investigated the catalytic organic transformation reaction for dihydropyran formation with Au nanoclusters using a microreactor (Gross et.al., 2014). The kinetic evolution of the reaction intermediates and products were mapped using synchrotron based microspectroscopy with spatial resolution as shown in Figure 2.9. Their investigation revealed a direct correlation between the properties of the catalyst and the reaction mechanism in real time.

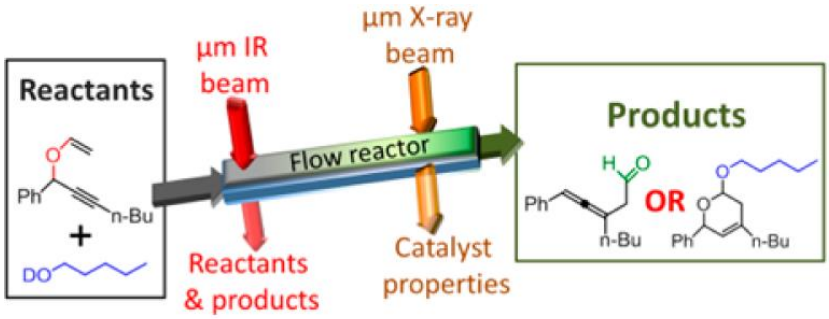

Figure 2.9: IR absorption microspectroscopy scans along the flow reactor. (Reproduced with permission from Ref. Gross et.al. Copyright ACS Publications, 2014)

CHAPTER 3: USE OF LAB-ON-A-CHIP DEVICES FOR GOLD NANOPARTICLES SYNTHESIS AND THEIR ROLE AS A CATALYST SUPPORT

3.1 Introduction

Gold catalysts have been receiving a lot of interest from researchers since the time Haruta and co-workers observed that gold nanoparticles (less than 5 nm in size) supported on metal oxides offered considerable enhancement to the catalytic activity and selectivity for low temperature oxidation of CO (Haruta, 1997; Haruta, 1987). Catalysis using gold nanomaterials (*i.e.* using both supported and unsupported gold nanoparticles as catalysts) is often preferred due to several reasons such as mild reaction conditions, less need for additives, better chemo selectivity, and the ability to carry out a variety of reactions (Thompson, 2007). Quantum size effects, presence of high densities to low coordinate atoms, excess electronic charge, and active perimeter sites are few models that were proposed to explain high catalytic activity of gold nanoparticles (Cho, 2003). Another important criterion for modulating catalytic activity is shape of the catalyst, which can be tuned by controlling the reaction conditions. Since most catalytic reactions occur at the perimeter interfaces around the nanoparticles, high surface area catalysts such as porous materials contain large number of surface active sites and generally yield higher catalytic activity. Gold nanoparticles supported over high surface area substrates play crucial role in chemical reactions by enhancing the chemical performance of the catalyst and in preventing agglomeration of the supported nanoparticles (Shaikhutdinov et.al., 2003). Ability to easily make changes to the design and carry out their synthesis depending on the type of chemical reaction to be catalyzed is an advantage these catalysts offer over others. Gold nanocatalysts synthesis has been advancing from the use of traditional co-precipitation and impregnation to the use of modern LOC techniques such as microfluidics and millifluidics (as shown in Figure 3.1). These

new techniques have significantly enhanced controlled synthesis and application of gold nanocatalysts in recent times (Cuenya, 2010).

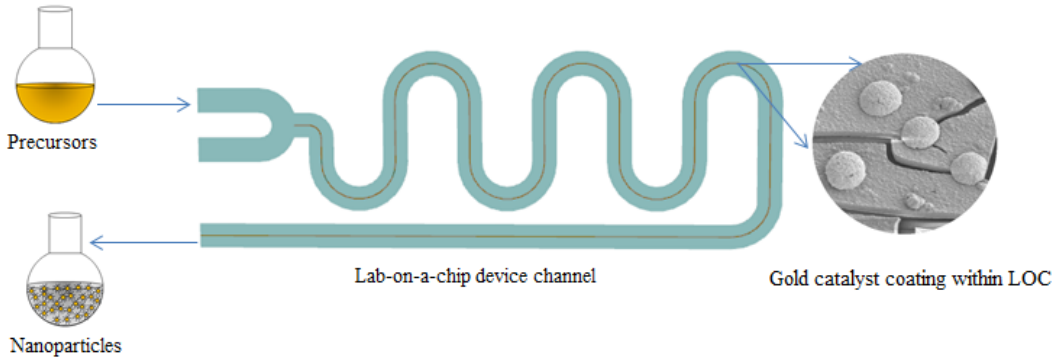

Figure 3.1: Pictorial representation of using millifluidic reactor for the synthesis and coating of nanoparticles simultaneously.

Based on the way the nanocatalysts are created within the LOC devices, the catalysis can be broadly categorized into two types. The first type can be named as Impregnated Flow Catalysis (IFC) in which the metal catalysts are prepared in a separate step and then incorporated within the flow reactor. In the second type, the nanocatalysts are grown (as a coating) within the flow reactor using bottom up approaches and can be named as Coated Flow Catalysis (CFC). In a recent review by Frost and Mutton et al., advancements in the design of flow catalysis reactors with a variety of supported catalysts have been utilized to promote a range of reactions including Heck, Sonogashira, Suzuki, Kumada, olefin metathesis, hydrogenation, and benzannulation reactions. These two generalized approaches for supporting catalysts in a flow reactor, schematically represented in Figure 3.2, are also applicable in the case of continuous flow nanostructured gold catalysis.

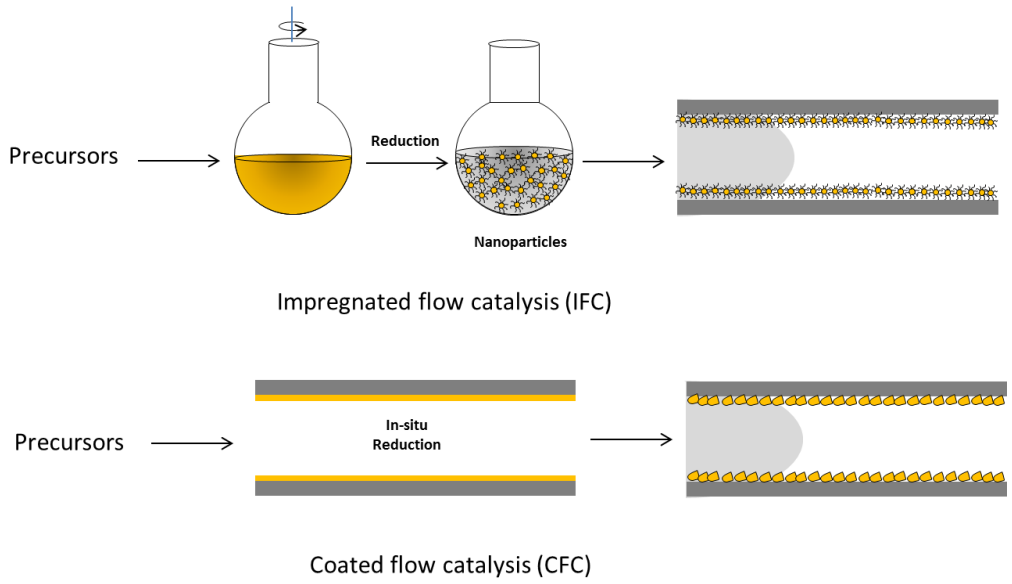

Figure 3.2. A schematic representation of the two types of process for preparing nanocatalysts for flow catalysis. (A) IFC process and (B) CFC process.

Some of the most recent reviews related to nanostructured gold catalysis and synthesis can be summarized as follows: Barakat and co-workers (Barakat et.al., 2013) reviewed gold catalysis for environmental applications; for oxidation of CO and volatile organic compounds (VOCs) and in water-gas shift (WGS) reaction for production of hydrogen. Ma and co-workers (Ma and Dai, 2011) highlighted gold nanocatalysts of various sizes and shapes, including unsupported or supported, those encapsulated in an inorganic matrix, post-modified gold catalysts, gold-based alloy catalysts, and gold catalysts with additional interfacial sites (or metal oxide components). A number of review articles on gold nanoparticle catalysis of organic reactions have also been published. For example, reduction reactions including chemo selective hydrogenation of nitro aromatic compounds (Serna et.al., 2011) and hydrogenation of multiple double bonds (Corma and Serna, 2012; Pan et.al., 2013), selective oxidation of organics (Wu et.al., 2011; Zhang and Toshima, 2013; Kusema and Murzin, 2013), complex organic transformations such as rearrangement of ω-alkynylfurans to phenols and the benzannulation of

O-ethynyl benzaldehydes (Stratakis and Garcia, 2012), and in formation of Nitrogen-containing compounds (Mielby et.al., 2012). Catalytic activity of unsupported gold nanoparticles for CO oxidation, aerobic oxidation of alcohols and diols, borohydride reductions and carbon–carbon cross coupling reaction among other reactions has also been recently reviewed (Mikami et.al., 2013). Surprisingly, not many investigations have been reported on nanogold catalysis in either in-flow conditions or using LOC devices (Jamal et.al., 2012; Abahmane et.al., 2011; Abahmane et.al., 2011; Wang et.al., 2007). The topic also has not been completely reviewed except for being a small part in the analysis of the field of LOC devices for synthesis of inorganic nanomaterials and quantum dots for biomedical applications (Krishna et.al., 2013). While the latest exhaustive review on gold nanoparticle catalysis was reported in the year 2008 (Corma and Garcia, 2008), it did not include any continuous flow catalysis. On the other hand, a thorough analysis of the advantages and disadvantages of flow chemistry and continuous processing in general has just been published (Newman and Jensen, 2013), and this analysis demonstrates how flow methods of synthesis can be greener than batch synthesis and that these are applicable over different scales of synthesis. Therefore, in this review we present an analysis of the most recent literature on synthesis and application of gold nanocatalysts from the view point of flow chemistry in general and LOC systems in particular. Although there have been several reports on using LOC's for synthesis of gold nanoparticles, this review article covers only on the catalytic aspect of gold nanomaterials and not on their other applications related to biosensing, nanomedicine, biochemical analysis, diagnostics, drug discovery, microscopy, and spectroscopy etc. The review is divided into four major sections including the introduction, overview of catalysis, and two flow catalysis systems, namely plug-flow reactors and LOC reactors based on tubular or chips.

3.2 An overview of gold catalysis and current challenges

The selection of appropriate gold catalyst is influenced by various factors such as the amount of reactants, product properties, size of the reactor, operating costs, energy required for the chemical conversion, etc. Therefore, a proper understanding of the catalyst-reactant interaction and dynamics is needed to have a good influence on the structure and bonding of species involved in the catalyzed conversions. Loss of activity and selectivity due to deactivation, decomposition, and fouling with a need for catalyst regeneration is a challenge for traditional flask-based, as well as flow-based catalysis in LOC devices (Dunnewijk et.al., 2004; Taniike et.al., 2007).

Gold nanocatalysis is a rapidly evolving research field which involves the use of gold-based nanomaterials as catalysts. The main aspect of the gold nanocatalysts revolves around complex interplay of physicochemical properties at the nanometer scale. The modulations of selectivity, activity, energy barrier, etc. are a few important factors that have to be considered before choosing a gold nanocatalyst for any chemical conversion. These are in-turn governed by the physical and chemical properties of the catalyst at nanoscale *viz.* size, shape, spatial distribution, surface composition, electronic structure, and also whether the catalyst is homogeneous or heterogeneous (Chaturvedi et.al., 2012).

An important factor when synthesizing gold nanocatalysts to be used in a solutions is to prevent agglomeration, which is known to decrease its surface area. This has been accomplished using stabilizers or surfactants that prevent agglomeration either through steric or charge repulsion. However, the challenge is to have sufficient access to the surface for enhanced

catalytic activity. Yet another challenge is to separate the gold nanocatalysts from the reaction solution without the need for tedious post-processing steps to completely recover the products (Chaturvedi et.al., 2012; Polshettiwar et.al., 2011). In the case of heterogeneous gold nanocatalysis, the gold nanocatalysts are immobilized on a solid support, and the supported catalysts can be recovered and recycled (Chaturvedi et.al., 2012; Polshettiwar et.al., 2011). However, the challenge here is to prevent agglomeration when the supported catalysts are subjected to high-temperature reaction conditions (Gaur et.al., 2012). While several of these challenges remain to be addressed, the field of gold catalysis has been moving clearly in the direction of gold nanocatalysis, which in turn is going in the direction of the atomically precise gold catalysis (Liu et al. 2013, Gaur et al., 2012; Zhu et al., 2010; MacDonald et al., 2010; Jin et al., 2010; Zhu et al., 2011; Jin et al., 2011; Wu et al., 2011; Qian et al., 2012; Qian et al., 2012). The traditional batch catalysis has already seen developments in this direction (Figure 3.3). However, there has yet to be an investigation reported of flow catalysis utilizing atomically precise catalysts, in general, or atomically precise gold catalysts, in particular.

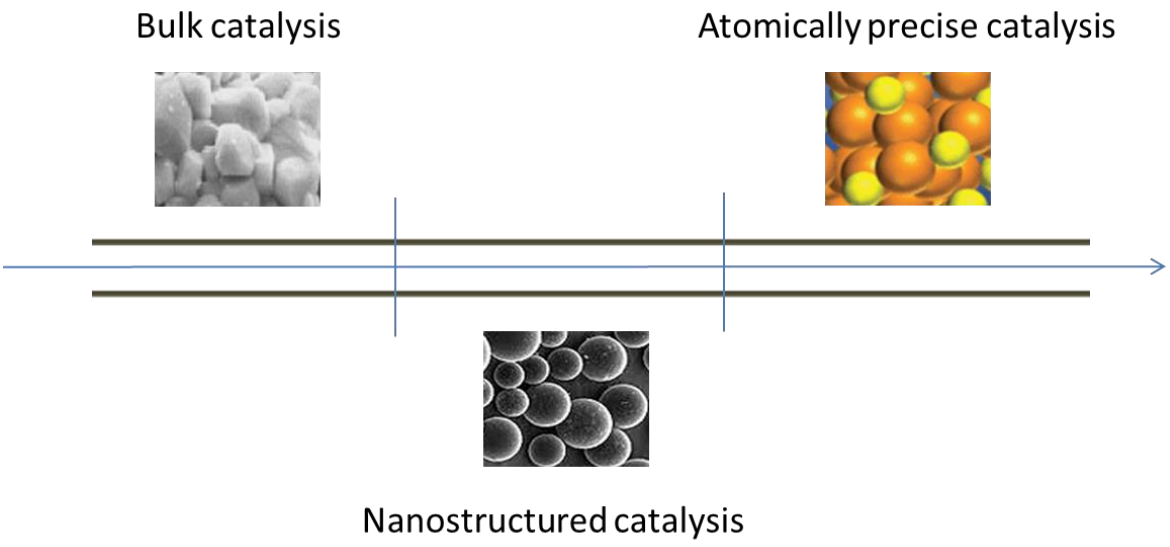

Figure 3.3. A schematic representation of the over view of the direction the field of gold catalysis is moving: from bulk catalysis to atomically precise catalysis.

In addition to the above challenges in terms of modulating the morphology of the gold catalyst, there are also several challenges with respect to preparation of supported gold catalysts. In general, some of the currently used approaches for preparing supported gold catalysts and their drawbacks are as follows (DeJong, 2009): In the first approach, typically, a catalyst is immobilized on a support and tested in a reaction flask. The disadvantage with this approach is the need for preparing the supported catalyst, and it needs to be separated and reused after the reaction (Gaur et.al., 2012; Turner et.al., 2008). The other disadvantage is the reproducibility of the supported catalyst preparation. In the second approach, catalysts are supported within large columns, and the reagents are flown through such fixed bed reactor columns (DeJong, 2009). The disadvantage with this approach is the lack of control over the structure of the catalyst (micro- and nano-precision) and, hence, the surface area of the catalysts. In the third approach, the catalysts are embedded within microfluidic channels, and catalysis is carried out as in the previous case (Ismagilov et.al., 2008). However, fabrication of microfluidic catalyst beds require sophisticated equipment and is expensive.

3.3 An overview of flow catalysis devices

Currently, most chemical conversion reactions need a catalyst to enhance their reaction rate in order to increase yield and selectivity in a shorter span of time. The process of catalysis is carried out using two methods: (a) batch catalysis and (b) flow catalysis. Both the batch and the flow catalytic systems use homogeneous and heterogeneous catalysts for chemical conversion. In a typical batch catalysis, a catalyst either in homogeneous phase or heterogeneous phase is added to the reaction mixture initially, and the products are collected after the reaction is complete. The catalyst is then recovered and recycled for the next batch. In contrast, in a flow catalytic system,

the reaction mixture is treated with the catalyst either in homogeneous or heterogeneous phase continuously and the product is collected separately as they form. In most cases, flow catalytic systems use heterogeneous catalyst, as the separation of the catalyst and the product happens easily without any further processing, thereby, reducing the time and effort required for recovery of the catalyst (Donati and Paludetto, 1999; Liu et.al., 2012).

The flow catalytic systems offer a number of advantages over batch catalytic systems; which are more relevant in the case of heterogeneous catalysts. Using them, the reaction processes can be controlled easily, allowing for the specific conversion of a reactant to the desired products. They are flexible enough to be designed and modified depending on the type of reaction and reaction conditions as the reaction progresses, leading to a better control of the products formed in a reaction. They also facilitate the scale up of processes, and the catalyst regeneration can be made simpler. For reactions involving the production of secondary products, they offer a possibility for their continuous removal without interfering with the main catalytic process. Several recent innovations have been reported in the design and fabrication of flow catalysis systems. Some of these are continuous flow silicon-pyrex microreactor for catalytic oxidation and hydrogenation (Liu et.al., 2012), macroporous monolithic microreactors for the synthesis of fine chemicals (Sachse et.al., 2011), *in-situ* continuous flow MAS NMR coupled with hyperpolarized ^{129}Xe for investigating reaction mechanisms and kinetics in heterogeneous catalysis (Zhang et.al., 2012), and spinning disc microreactors for oxidation of alcohols, axial flow, spherical packed bed reactor for methanol synthesis (Rahimpour et.al., 2011). Jensen and group reported a variety of flow catalysis reactors with unique capabilities for carrying out multiphase catalytic reactions, such as gas-liquid trickle bed reactor, porous silicon posts, cross-

flow packed bed, and parallel packed bed with integrated temperature sensors (Nagy and Jensen, 2011). An interesting new concept for the immobilization of nano-sized catalyst on microreactor walls was described by Stubenrauch et al. (Stubenrauch et.al., 2006) and Roumanie et al. (Roumanie et.al., 2008). Both authors made use of black-silicon microneedles in order to increase the active surface area of the silicon microsystems, which enhanced the reactor wall surface. The needle arrays were used for direct immobilization of catalytic metals as well as to stabilize a catalytic wash coat.

Brivio and co-workers (Brivio et.al., 2006) highlighted a variety of innovative flow reactors utilized for catalysis of a number of organic reactions. These range from flow reactors with electro-osmotically driven fluidics systems to those that have low dead volume connectors. In addition, the designs include those containing independent microfluidic units in a parallel configuration to "pile-up" reactors with a number of piled-up glass plates and those for combinatorial flow catalysis. Yet another novel design is a set of modular and monolithic microreactors based on the integration of microfluidics and a thermal platform (Martinez-Cisneroz et.al., 2012) as shown in Figure 3.4. The key point here is the immense potential in developing newer reactor designs to meet the requirements of any catalytic reaction.

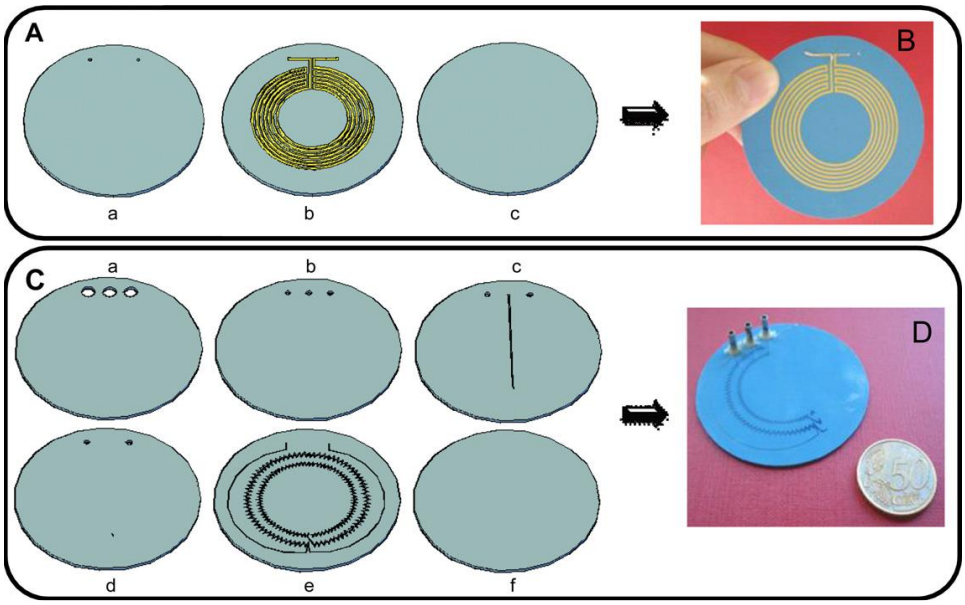

Figure 3.4. Layer by layer design of both platforms integrating the LTCC microreactor. (A) Thermal platform; (a) top layer (4×); (b) screen-printed heater (1×); (c) bottom layer (4×). (B) Picture of the thermal platform fabricated. (C) Microfluidic platform; layers (a and f) were fabricated by duplicate; the microfluidic structure was embedded at layer (e). (D) Picture of the microfluidic platform, which includes an exposed section regarding the micromixer. (Reproduced with permission from ref Martinez-Cisneros et.al., Copyright Elsevier, 2013)

The flow catalytic reactors can be broadly classified into plug flow (or tubular) reactors and chip-based reactors. The chip-based reactors are traditionally called as LOC devices. However, a more inclusive definition of LOC devices could cover both tubular as well as chip-based devices with channel dimensions in the micro to millimeter range. These could also be easily distinguished from flow systems with larger dimensions for large-scale synthesis. A brief description of these different types of flow reactors for catalysis is given below.

3.4 Tubular or plug-flow reactors

Plug flow reactors are tubular reactors that are utilized for continuous chemical processes. These types of reactors are filled with the desired catalyst for chemical conversion to take place. The geometry of a plug flow reactor plays an important role depending on the type of

chemical reaction, required selectivity and conversion efficiency. They also have the ability to add multiple reactant mixtures at different points if needed. Usually, a plug flow reactor is called a packed bed reactor when it is packed with a solid material, in most cases, a solid catalyst. The reactant to product conversion within the plug flow reactor is measured with respect to the residence time of the plug, which is a function of its position in the reactor. Plug flow reactors have the ability to run for extended periods and have high volumetric unit conversion. In a plug flow reactor, a stable concentration profile can be obtained at steady state with concentrations varying in space as the reaction happens in the flow path. The heat transfer rate can be controlled with ease when the reactor is packed with thinner tubes or fewer thicker tubes packed parallel. Another advantage of using a plug flow reactor is its low operational cost. However, undesired thermal gradients, poor temperature control, gas exchange limitations in a sealed reactor and expensive maintenance are some of the current challenges (Walter et.al., 1995). A typical millifluidic tubular reactor is made up of polymer or glass capillaries with a diameter in the order of millimeters. Tubular millifluidic reactors has also been utilized to produce hierarchically organized multiple emulsions or particles with a good control over sizes and shapes (Lorber et.al., 2011).

The other types of reactors such as gas-liquid trickle bed reactor, crossflow packed bed, parallel packed bed with integrated temperature sensors (Nagy and Jensen, 2011), flow cell reactor (Huang et.al., 1992), drip flow reactor (Goeres et.al., 2009), capillary reactor (Powell and Slater, 1983), membrane reactors (Tosti et.al., 2003), etc. are few examples of tubular or plug flow reactors that can be used for biological, chemical, physical analyses, and studies.

3.5 Lab-on-a-chip systems: Microfluidics and Millifluidics

A LOC device is a single chip designed to have components with varying dimensions. The size of this device can range from a few centimeters to nanometers and can handle lesser volumes of fluid. Various laboratory functions can be integrated into a LOC device when all the components are precisely positioned in order to have reliable and repeatable reaction conditions (Li et.al., 2012). Some of the challenges in tubular reactors such as requirement for larger space, unavoidable zero dead fluid volume, longer response time, higher power consumption, lower reproducibility, higher waste, and so on can be addressed using chip-based LOC devices (Gravesen et.al., 1993; Jensen, 2001). A variety of designs of chip-based LOC devices have been reported demonstrating flow principles, mixers, and traps ranging from the simplest form of the T-section systems, where two fluid inputs enter through channels at the bottom and slowly diffuse over the length of the microchannel to tangential microchannels, where the channels can exchange fluid through the shared area of contact (Chrimes et.al., 2013). More sophisticated designs include a pillar array PDMS-based microfluidic channel for the SERS detection of hazardous materials to microfluidic traps using optical, mechanical, dielectrophoretic, electrophoretic, acoustic, and magnetic forces.

In a LOC device, scaling up of the reaction conditions is simple and straightforward, which is done either by carrying out the reaction in continuous flow mode or by increasing the throughput through parallel processing. The use of LOC devices can also decrease the time for process transfer from lab to pilot-plant and then to industrial scale, and the products can be monitored online (Jensen, 2001). The kinetics, selectivity, and the product yield can also be improved easily, given that the external parameters like pressure, temperature, and reactant

mixing is taken into account (Ratner et.al., 2005). As the volume needed for the LOC experiments is much less, i.e., in the range of microliters to nanoliters, miniaturization of the flow channels allows us to change the experimental conditions along the reaction path in a shorter time (milli- to microseconds). Hence, LOC devices allow systematic investigation for the development of new synthetic strategies for investigating larger parameters if an online readout is available (Boleininger et.al., 2006).

To overcome the disadvantages of conventional-based methods for nanoparticle preparation, LOCs can be operated at optimized and steady state with control over the reaction conditions like reagent addition, mixing, temperature, and scaling higher throughputs involving parallel operation of multiple reactor units (Jensen, 2001; DeMello, 2006). There have been reports demonstrating wet chemical synthesis of semiconducting, metallic, dielectric, magnetic, and core shell NPs using the microfluidic methods (Chan et.al., 2003; Edel et.al., 2002; Nakamura et.al., 2002; Abou Hassan et.al., 2008; Khan and Jensen, 2007; Shalom et.al., 2007; Song et.al., 2008). However, prohibiting the NPs from growing over the walls of the LOCs is a challenge in the continuous flow reactor while preparing colloidal metal dispersions. Significant deposition of NPs and aggregation over the reactor walls has been attributed to the high surface to volume ratios (Boleininger et.al., 2006) For reactions happening at laminar flow within a microreactor, by selecting the appropriate choice of reaction conditions and microreactor wall material, polymer additives, and developing concentric laminar flow patterns, the issue over the particle deposition and aggregation can be overcome or minimized (Boleininger et.al., 2006; Wagner and Kohler, 2005; Wagner et.al., 2004; Kohler et.al., 2005; Takagi et.al., 2004). It

should also be noted that broader particle size distributions within a millifluidic or microfluidic reactor can be achieved with higher residence time of reactants (Duraiswamy and Khan, 2009).

LOC devices such as the microfluidic systems are constructed to perform chemical reactions, which are designed in such a way to maximize the efficiency of the reaction conditions. The significant aspect of performing a reaction in a microfluidic reactor is that the reaction conditions can be controlled desirably according to flow rate, concentration, pressure, etc. Early microfluidic devices had stainless steel and polymer tubing to provide reactant flow into the reactor. However, with repeated experiments, silica tubing is being used nowadays to achieve proper mixing and preparing hydrodynamic micro- and nanostructures. Other advantages of using microfluidic devices are low fluid volumes, good process control, quicker analysis, compact, safe, and reproducible results (Fair et.al., 2007). Especially for flow catalysis, an ideal microfluidic reactor should be capable of working at the desired working conditions (pressure, temperature, chemical compatibility, concentration, etc.) without breaking the system. A few examples of such microfluidic reactors are shown in Figure 3.5 (Marre et.al., 2012).

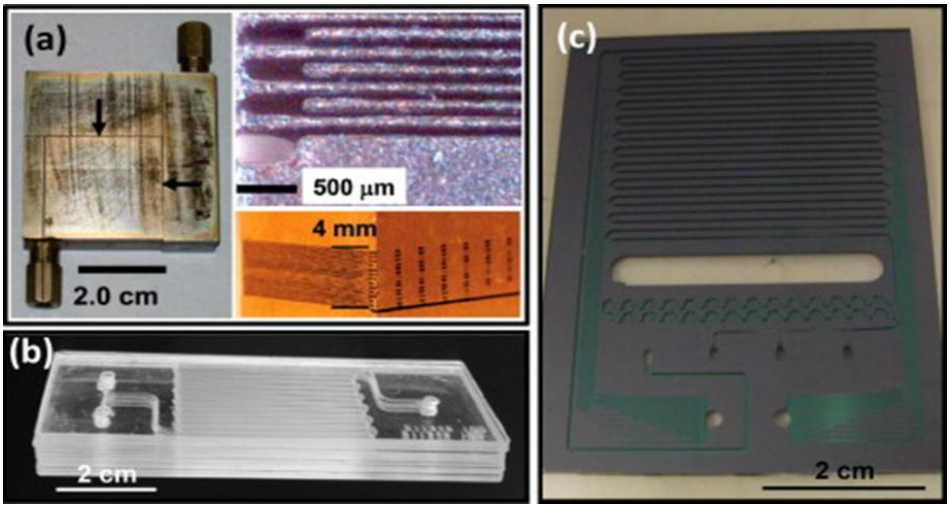

Figure 3.5. Examples of (a) metal, (b) glass/glass, and (c) silicon/Pyrex and microreactors. Reproduced with permission from ref. Marre et.al., copyright Elsevier, 2012)

Millifluidic devices can be considered as low-cost LOC devices that have been utilized for synthesis of a variety of micro- and nanomaterials. They offer more advantages over the microfluidic devices. For example, larger quantities of NPs can be produced with good control over their size-distribution and shape. They do not require expensive lithography for their fabrication. They can also be used as flow reactors with potential opportunities to manipulate and functionalize the products at different stages of synthesis (Engl et.al., 2007). The flow rates of the reactants that are fed into the millifluidic reactor can be increased, thereby, reaching easy scale up by integrating several reactors on a single platform. Owing to the continuous reaction conditions and low-cost methodology, millifluidic devices are used as a potential production tool in industries. The millifluidic devices can be easily assembled and disassembled without any expensive techniques such as lithography or etching for fabrication. As the channel dimensions are increased when compared to the microfluidic reactor, channels are less prone to clogging in a millifluidic reactor, thereby, resulting in lesser residence time of the reactants. The millifluidic devices can also be used to prepare atomically precise nanomaterials and study their *in situ* formation in order to obtain time-resolved kinetic details of the nanomaterials formed. A chip-based LOC is a device that is made up of polymer or glass as a substrate. These devices can be fabricated into any desirable shape, which can be fully integrated to analytical equipment for characterization, identification, and separation processes. Moreover, the reaction channels in a chip-based LOC can be designed into various shapes (e.g. zigzag, spiral-shaped, serpentine-shaped channels) according to the experimental conditions. To summarize, a simple millifluidic device bridges the gap between a microfluidic device and bulk reactor. A traditional microfluidic device has a channel dimension in micrometer scale and can hold a fluid volume of a few nanoliters to a few microliters. In contrast, a millifluidic device has a channel dimension in

millimeter scale, which can carry fluid volume of several milliliters and offers high throughput without compromising on the flow properties. In addition, it offers superior *in-situ* monitoring capabilities due to higher signal-to noise ratio than traditional microfluidic devices.

3.6 LOC devices for synthesis gold nanoparticles and their catalysis

3.6.1 Overview of LOC synthesis of metal nanocatalysts

Many inorganic and organic nanocatalysts have been synthesized in a continuous manner with more control over the particle size distribution, shape, and quality of the nanomaterial. LOC devices for synthesis of inorganic nanomaterials have recently been reviewed (Krishna et.al., 2013). A variety of metal NPs, metal oxide NPs, semiconductor NPs, quantum dot (QD) core-shell-structured micro-, and nanostructures are few types of nanomaterials synthesized using the LOC devices. Most often, reducing agents such as sodium borohydride, lithium hydrotriethyl borate, 3-(*N*,*N*dimethyldodecylammonia) propane sulfonate, and sodium citrate are used as the reducing salts for synthesizing metal NPs. Ligands, though required to stabilize NPs from agglomeration, have a deleterious effect on the catalytic activity of NPs. For example, the most commonly used ligands like thiols, phosphines, amines, etc., for gold NPs synthesis hinder the reactant to reach the metal surface when they are in heterogeneous phase, thereby, reducing their catalytic activity. A well-known example for heterogeneous-phase gold catalysis is the gas-phase CO oxidation reaction (Gaur et.al., 2013). However, in solution-based homogeneous catalysis, the ligands tend to disperse in the solvent, thereby allowing the reactants to reach the metal surface and hence resulting in increased catalytic activity, for example, styrene oxidation in toluene (Zhu et.al., 2010). In general, these ligands can be removed from the NP surface by several methods like calcination (Liu et.al., 2013), oxygen treatment (Nie et.al., 2012), and ozone

treatment (Lope-Sanchez et.al., 2011). The synthesis of metal nanocatalysts within the LOC devices is carried out in two ways. In, the first method the metal precursors are fed into the reactor followed by the addition of the second reactant into it as shown in Figure 3.6 (Wagner et.al., 2005). To reduce the risk of agglomeration, ligands and surfactants are passed through the reactor in the final step. The disadvantage of using this approach is that the reactants are fed into the LOC sequentially, which leads to a large residence time distribution. Owing to the continuous single-phase reaction condition, the possibility of reactant clogging within the channel is high, thereby, resulting in loss of optical and absorption information. The second approach toward the synthesis of metal nanocatalyst using the LOC devices is that the reaction solutions are fed simultaneously within the reactor through separate inlets as shown in Figure 3.7 (Duraiswamy and Khan, 2009). These reactants mix together within the LOC device, where the nucleation and the growth of the nanocatalyst take place. The second approach is preferred due to its short residence time distribution and less chances of clogging (Liu et.al., 2012).

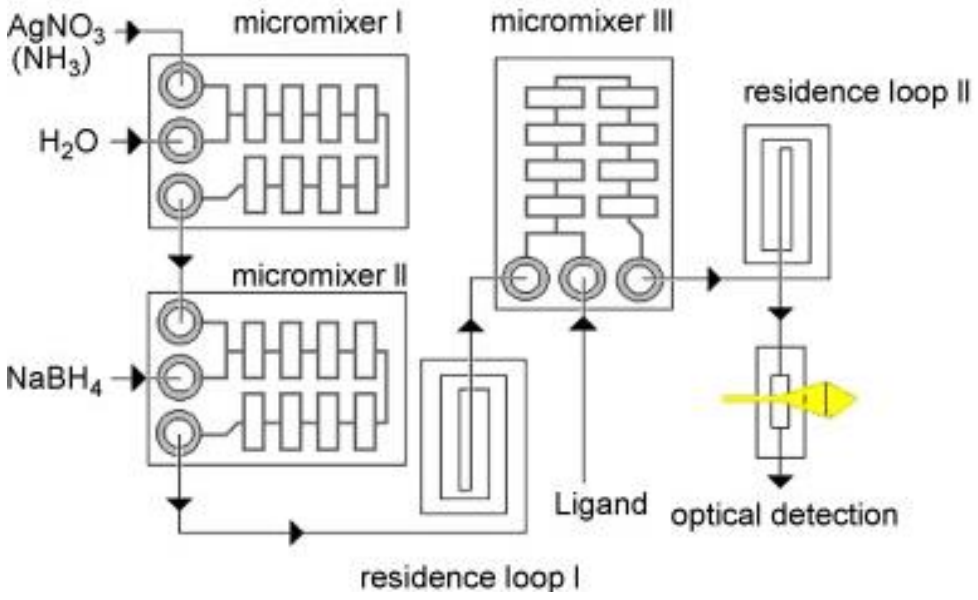

Figure 3.6. Schematic illustration of reactant feed into the LOC device. Modular microreactor arrangement for flow-through process: (Reproduced with permission from ref Wagner et al., copyright Elsevier2008)

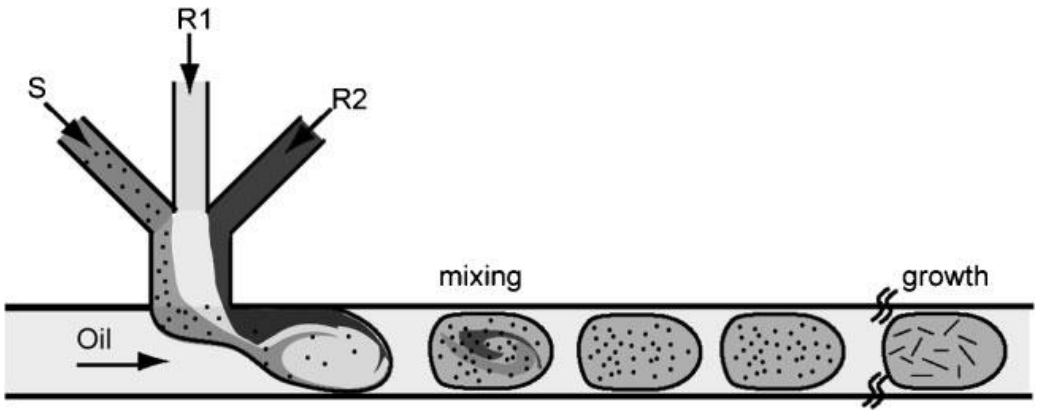

Figure 3.7. A gold nanoparticle seed suspension (S) and aqueous reagent solutions (R1 and R2) are separately delivered into one arm of a microfluidic T-junction, and silicone oil is delivered into the other arm. Droplets are pinched off at the T-junction. Reagents and seeds are rapidly mixed by chaotic advection. The oil forms a thin lubricating layer around the translating droplets, and prevents contact between growing particles and the microchannel walls (Reproduced with permission from ref Wagner et al., Copyright Wiley-VCH Verlag GmbH & Co. KGaA 2009)

Several metal nanocatalysts have been synthesized using the microfluidic devices. A few common nanocatalysts that were prepared using the microfluidic devices are gold NPs and nanorods (Boleininger et al., 2006, Shalom et al., 2007; Kohler et al., 2005; Duraiswamy and Khan, 2009), silver NPs (Liu et al., 2012) and nanorods (Boleininger et al., 2006; Wagner et al., 2005; Kohler et al., 2008), copper NPs (Song et al., 2005), palladium NPs (Song et.al., 2004; Torigoe et.al., 2010), CdSe@ZnS (Torigoe et.al., 2010), CdSe@ZnSe (Yen, 2007), SiO_2@TiO_2 (Khan and Jensen, 2007), γ-Fe_2O_3@SiO_2 (Abou-Hassan et.al., 2009), [CdSe@ZnS] in PLGA microgels and microcapsules (Chang et.al., 2007), γ-Fe_2O_3 in microhydrogels (Hwang et.al., 2008), γ-Fe_2O_3 or QDs in PNIPAM microcapsules (Kim et.al., 2007), and superparamagnetic Janus particles (Yuet et.al., 2009). The syntheses of these nanocatalysts vary accordingly with respect to the temperature and the type of microfluidic reactor used. SU-8-PEEK, glass capillary, PVC and PEEK tubing, silicon Pyrex, silica capillary, PDMS glass, PDMS glass+aluminum

reflectors, etc., are few types of microreactors that were used to prepare these nanocatalysts (Marre and Jensen, 2010).

Although millifluidic devices prove to be an efficient tool in continuous flow catalysis, there are only a few reports on millifluidic nanocatalysts, and these are discussed in this Thesis. Millifluidic systems offer similar reaction conditions for the synthesis of metal nanocatalysts like that of the microfluidic systems. Unlike microfluidic devices, metal nanocatalysts synthesized using millifluidic reactors withstand higher pressures and velocity distribution confined to the width of the interfacial zone (Biswas et.al., 2012; Li et.al., 2012; Krishna et.al., 2013).

3.6.2. Synthesis of nanostructured gold catalysts using LOC devices

Owing to its intrinsic value and properties, gold has always been considered as a noble metal of all the elements (Hammer and Norskov, 2002). When gold catalyst is in nanoparticulate form, it possesses several unique properties. At nanoscale, gold can be used to transform carbon monoxide to carbon dioxide. It is used to remove toxins from exhaust gases. Gold NPs have different properties from those of bulk gold (Eustis and El-Sayed, 2006; Chen and Goodman, 2004; Valden et.al., 1998). A number of reactions have been efficiently catalyzed by gold NPs. For example, carbon monoxide oxidation (Haruta, 1987), catalytic combustion of hydrocarbons (Haruta, 1997), hydrochlorination of ethyne (Conte et.al., 2007), hydrogen sulfide and sulfur dioxide removal, oxidation of glucose to gluconic acid (Ma et.al., 2013), oxidative decomposition of dioxins, oxidative removal of mercury, ozone decomposition (Zhang et.al., 2009), reduction of NOx with propene (Seker and Gulari, 2002), carbon monoxide or hydrogen, selective oxidation, e.g., epoxidation of olefins, selective hydrogenation (McEwana et.al., 2010),

e.g., of alkynes and dienes to mono-olefins, vinyl acetate synthesis from ethene, acetic acid, and oxygen, etc. However, atomically precise gold NPs catalysts have been explored for their effectiveness in only few of these reactions (Li and Jin, 2013; Liu et.al., 2013).

Capping agents such as ligands, surfactants, polymers, and dendrimers are commonly used to confine the growth of the gold NPs in a controlled synthesis (Frens, 1973; Brust et.al., 1994; Jana et.al., 2001; Nikoobakht and El-Sayed, 2003; Sun and Xia, 2002; Ahmadi et.al., 1996; Porel et.al., 2005; Sun et.al., 2005). A good control over the growth of NPs with respect to its size, diameters < 150 nm were seen in the reduction of tetrachloroaurate ions in aqueous solution along with a reducing agent. In most cases, sodium borohydride has been used as the reducing agent, which is one of the most preferred reducing agent to synthesize spherical gold NPs. Various other methods that were carried out for synthesis of gold NPs were by using poly(*N*-vinyl-2-pyrrolidone) as a protective agent in ethylene glycol for shape control (Sun and Xia, 2002). A seed-mediated growth approach was carried out with the surfactant cetyltrimethylammonium bromide (CTAB) as the directing agent in order to prepare gold nanorods in aqueous solution (Jana et.al., 2001; Murphy and Jana, 2002). Another method of preparation involved the use of $[Au(SO_3)_2]^{3-}$, which was decomposed and precipitated under acidic conditions to synthesize the quasi monodisperse gold microspheres (Li et.al., 2007). Also, gold spheres with diameters of more than 1 mm were synthesized in a controlled flower-like fashion using a simple electrochemical route (Guo et.al., 2007). Reactants like poly(sodium 4-styrene sulfonate) was used as an emulsifier, water treatment agents like dispersants, flocculation agents, sulfur exchange resin, etc. have been used along with various gold salts for preparing the gold NPs (Shan et.al., 2010).

Owing to the smaller dimension of the microfluidic devices, characterization of gold NPs in order to study its morphology and structural chemistry becomes tedious. In recent times, this disadvantage is overcome by synthesizing catalytically active gold micro- and nanostructures in a millifluidic platform. Gold catalysts prepared using this method offered a greater scope for spectroscopic probing of catalysis reactions as they happens. A comparative study between millifluidics-based synthesis and traditional flask-based synthesis of gold micro-/nanostructures shows that size and morphology of the gold can be better controlled by varying the flow rates using millifluidic systems (Li et.al., 2012). There have been several reports on the synthesis of gold NPs using LOC devices. Influence in the reaction conditions such as flow rate, temperature, reducing agent, concentration, catalyst support, etc., play a vital role in particle synthesis using the LOC devices. Gold NPs of different sizes and shapes have been synthesized using stabilizing agents. These agents help in preventing particle agglomeration during the synthesis. Tetraoctylammonium bromide (TOAB), 1-dodecanethiol, 11-mercaptoundecanoic acid, polyvinyl pyrolidone (PVP), etc., are few reagents that have been used in the preparation of ligand-stabilized gold NPs.

Lohse and coworkers studied high-throughput synthesis and functionalization of gold NPs with different sizes and shapes using a simple bench top reactor system (Lohse et.al., 2013). A flow reactor assembly (Figure 3.8) was used to operate for the synthesis of gold NPs by modifying previously reported synthetic procedures (Dahl et.al., 2007; Gole and Murphy, 2004). Citrate-stabilized gold NPs of size 4 nm were synthesized by mixing tetrachloroauric acid and sodium citrate with a residence time of 3 min to obtain a reddish brown solution. An experiment

based on the Brust-Schiffrin procedure was also carried out to synthesize 3 nm of mercaptohexanoic acid-stabilized gold NPs (Sweeney et.al., 2006; DeMenech et.al., 2008; Murphy, 2008) and CTAB-stabilized Au NP growth procedures (Orendorff and Murphy, 2006). CTAB-stabilized 2- and 8-nm gold NPs were synthesized by mixing tetrachloroauric acid and CTAB with sodium borohydride solution to give deep brown and vibrant red color solutions, respectively. They have used the 8-nm gold NPs as seeds for the synthesis of the 20-nm gold NPs, and in a similar fashion, 20-nm gold NPs were used as seeds for the synthesis of 40-nm gold NPs. All the gold seeds and NPs were stabilized using CTAB in solution.

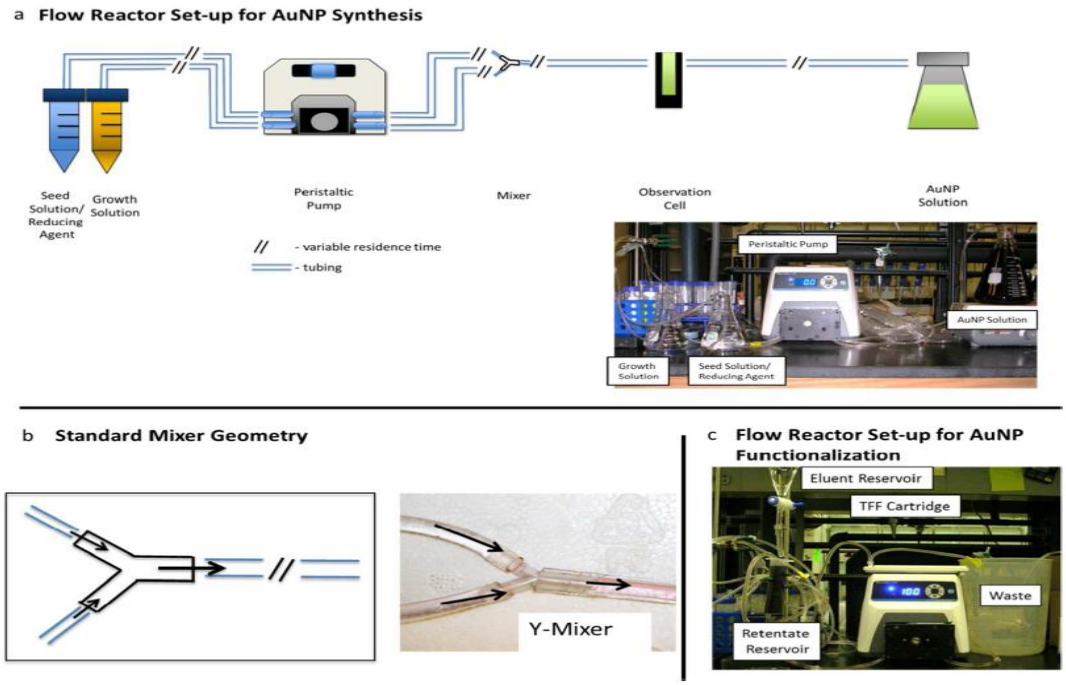

Figure 3.8. The integrated millifluidic reactor used for gold nanoparticle synthesis and functionalization is shown. (a) Diagram and picture of the reactor for AuNPs synthesis. The reactor is composed of multiple modular commercially available components, and fluid flow is driven by the peristaltic pump. (b) In this reactor, mixing of the growth solution and the seed/borohydride solution occurs in a simple polyethylene Y-mixer. (c) The reactor also features an integrated flow-based purification system, in which a commercially available tangential flow filtration cartridge can be attached to an additional peristaltic pump in order to integrated high-throughput approach for nanoparticle purification or functionalization (Reproduced with permission from ref. Lohse et.al, Copyright ACS Publications, 2013)

Lohse and coworkers (Lohse et.al., 2013) have also reported the synthesis of gold nanorods using different synthesis protocols. They synthesized gold nanorods with the flow reactor by the seeded growth approach (Murphy, 2008; Orendorff and Murphy, 2006; Sau and Murphy, 2004), where growth solutions containing tetrachloroauric acid, silver nitrate, and l-ascorbic acid were mixed with aqueous CTAB solution. These solutions that were prepared were fed into the flow reactor at 50 ml/min having a residence time of 3 min where they mix with each other within the reactor before they get deposited into a conical flask. Similarly, gold nanorods were prepared by using borohydride and ascorbic acid method within the flow reactor using the reported procedures (Jana, 2005; Si et.al., 2010; Ali et.al., 2012). Gold nanorods with dog bone structure and nanorods with large transverse diameters were prepared by modifying the isotropic overgrowth with the increased ascorbic acid addition (Gou and Murphy, 2005; Ni et.al., 2008; Song et.al., 2005). As before, the growth solution was prepared by mixing tetrachloroauric acid with silver nitrate and L-ascorbic acid. CTAB solution was mixed with 4 nm of gold seed dispersion, and the mixture was aged for 2 h to prepare the seed solution. The growth and the seed solutions were then fed within the flow reactor at 50 ml/min and deposited into a conical tube. The nanorods formed through this procedure were 1.2 nm in size.

Tsunoyama and coworkers (Tsunoyama et.al., 2008) reported the synthesis of gold clusters of size ~1 nm stabilized by PVP using a microfluidic reactor. Syringes were used to feed the aqueous $HAuCl_4$ and PVP solutions into the microfluidic reactor kept in a methanol bath at 0°C. The individual solutions were overlaid in an interdigital arrangement in region I (Figure 3.9), where the solutions were laminated into 16 sub-streams, and region II had wide multilamellar flow, which was compressed into a single 0.5-mm-wide stream. An Erlenmeyer

flask was used to collect the mixed solution eluted from the outlet in an ice bath and was stirred for 1 h. Au clusters stabilized by PVP were obtained by ultrafiltration after subsequent deionization.

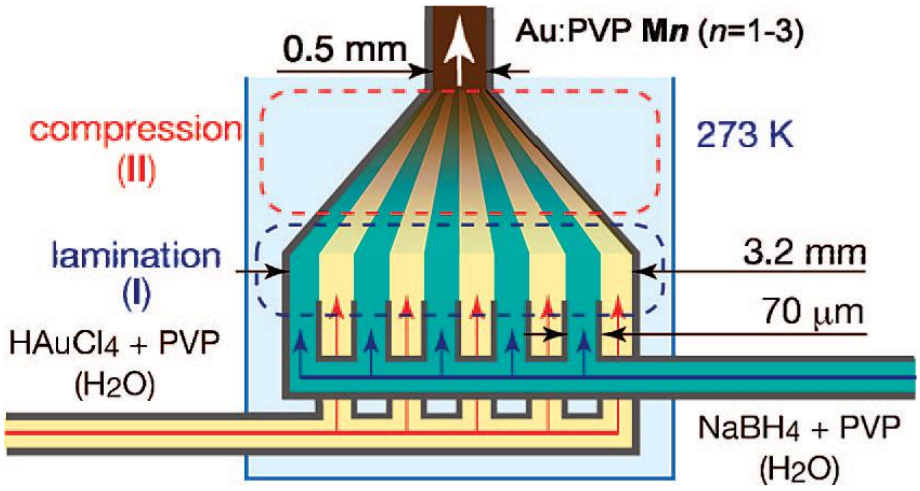

Figure 3.9. Schematic diagram for the synthesis of PVP-Stabilized Au clusters in a micromixer (Reproduced with permission from Ref Tsunoyama et.al. Copyright ACS Publications, 2008).

Shalom and coworkers (Shalom et.al., 2007) also reported the synthesis of thiol-stabilized gold NPs of sizes ranging from 2.9 to 3.7 nm with standard deviations of particles of size range between 0.6 and 0.9 nm respectively, using the microfluidic reactor. The thiol-functionalized gold NPs were often called as monolayer-protected clusters (MPCs). The gold-thiolate polymer was prepared by phase transfer of $HAuCl_4$ into toluene using TOAB followed by the addition of 1-dodecanetiol. A three-layer micromixer (Figure 3.10) was used to mix the thiol-stabilized gold NPs with $NaBH_4$, which acts as the reducing agent (Brust et.al., 1994). Different mole ratios of gold-thiolate polymer were fed into the microfluidic device with $NaBH_4$ to produce the monolayer-protected NPs.

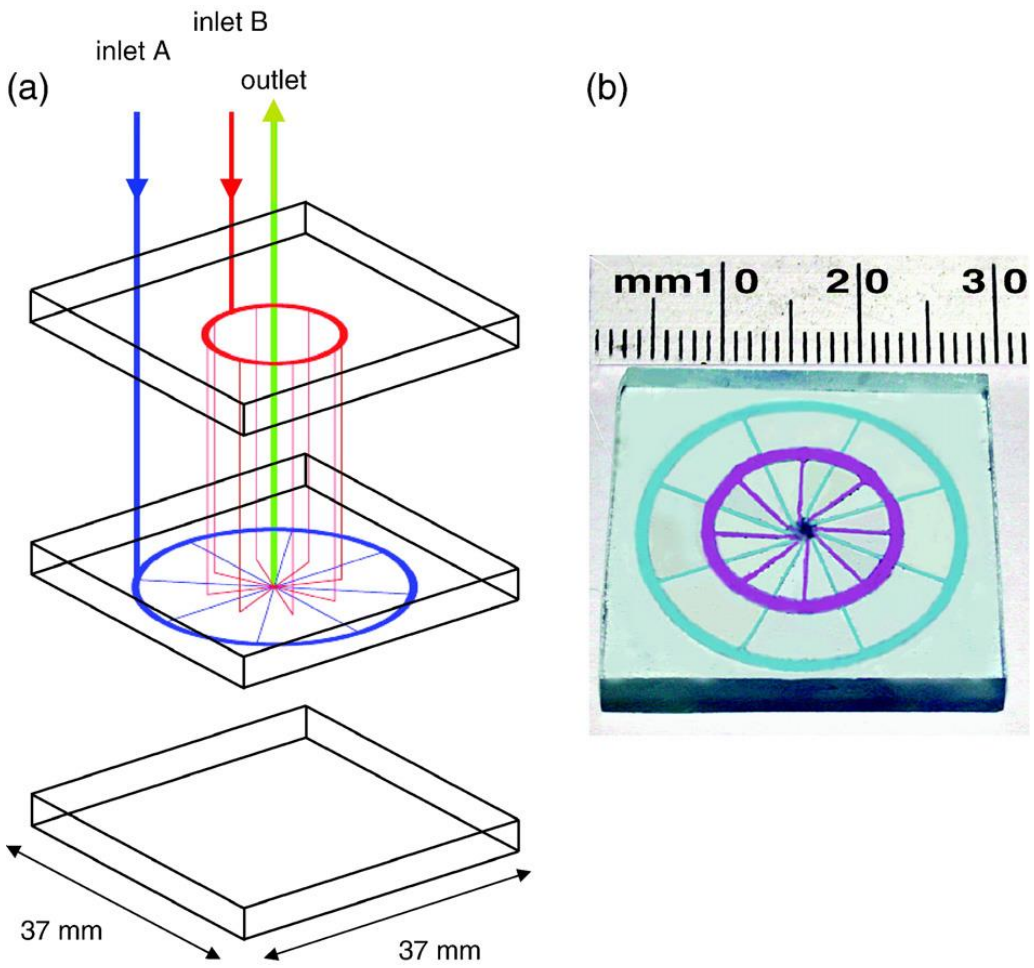

Figure 3.10. (a) Three-dimensional schematic of a radial interdigitated mixer. Each mixer is fabricated in 3-layers. In the first two layers input flows are directed to two circular bus channels which, in turn, split the flow into 8 identical fluid laminae and deliver reagent streams towards a central mixing chamber. The final layer acts as a cap to enclose channels and as a guide for input and output capillaries. The output is from the center of the uppermost layer. (b) Photograph of the fabricated mixer. Microchannels are filled with dye solutions to show different shadings for the different channels. (Reproduced with permission from Ref Shalom et.al. Copyright Elsevier, 2007)

Pedro and coworkers (Pedro et.al., 2010) reported similarly prepared gold NPs with an average diameter of 2.7 nm stabilized by 11-mercaptoundecanoic acid (MUA) using microfluidics. In their report, the gold colloid was prepared by single phase reaction by reducing gold (III) chloride with $NaBH_4$ prior to stabilizing it with MUA. Syringes were used to control the flow rate of the reactants within the microfluidic device fabricated by low-temperature co-

fired ceramics technology (LTCC). A multilayer design of 3D structures was integrated into these static mixers along with electric, mechanic, and fluidic components using LTCC technology. With this static microfluidic mixer, the overall process of MUA-stabilized gold NPs synthesis was split into two steps. The first step involved the preparation of gold NPs, where the respective reactants, gold (III) chloride and $NaBH_4$ were hydraulically focused in a laminar fashion within the microfluidic device. The gold chloride solution was then fed into the microfluidic device between two streams of $NaBH_4$ in order to have efficient mixture. In the next step, the as-formed gold NPs were stabilized by feeding MUA into the microfluidic device through a separate inlet. The resulting solution collected out from the device was found to be fully MUA protected gold NPs.

Polte and coworkers (Polte et.al., 2010) also reported a different method for growth of gold NPs with an average radius of 0.8 nm to about 2 nm using a microstructured static mixer. These gold NPs were prepared at room temperature by homogeneously mixing aqueous tetrachloroauric acid ($HAuCl_4$) with $NaBH_4$ within the static micromixer (Figure 3.11). Different residence times were applied to synthesize the gold NPs. At an increased residence time, it was observed that there was no apparent effect on the particle size suggesting that the growth of the particles happens at a shorter scale. The experimental setup was used successfully for gold NPs synthesis using the sodium borohydride as the reducing agent. It was analyzed that the gold nuclei Au^0 was formed initially at a rapid complete conversion from the gold precursor when the setup was coupled to X-ray absorption near-edge spectroscopy (XANES). These gold nuclei coalesced into larger particles, and within 100 ms, the gold precursor was completely converted to metallic gold due to rapid mixing within the microstructure mixer

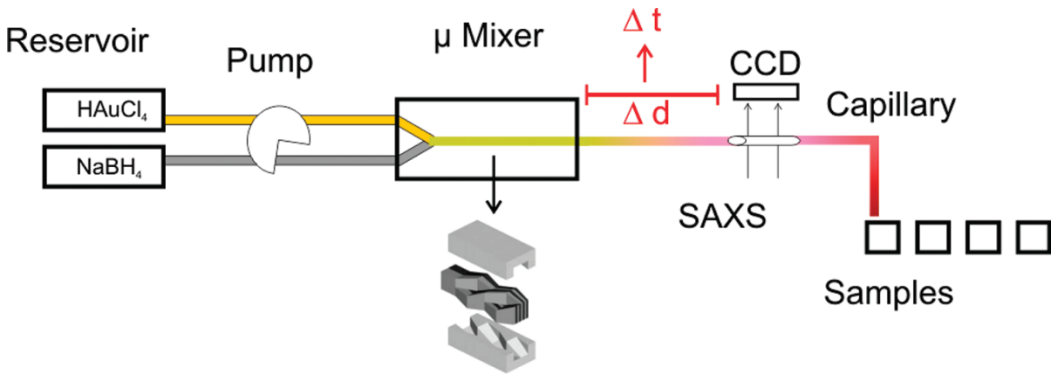

Figure 3.11. Experimental setup for particle synthesis in continuous-flow mode coupling a microstructured static mixer directly to SAXS-analysis in a flow cell. (Reproduced with permission from Ref Polte et.al., Copyright ACS Publications, 2010)

A similar time-resolution study on the size evolution of gold NPs with an average particle size of 2.53 nm in a millifluidic reactor was reported by Li and coworkers (Li et.al., 2012). Different residence times of the reactants $HAuCl_4$ and $NaBH_4$ were applied to prepare the gold NPs using a millifluidic device, and the spatially resolved size evolution of the gold NP was investigated using transmission electron microscope. They prepared the gold NPs by mixing aqueous $HAuCl_4$ and DMSA within the millifluidic device followed by the addition of $NaBH_4$. The flow of the reactants was controlled using a syringe pump (Figure 3.12). It was observed that the gold NPs showed a broader size distribution at a residence time of 3.53 s, and the control of particle size was much easier with a milliscale LOC device when compared to the conventional-based synthesis of gold NPs.

Figure 3.12. Schematic illustration of the millifluidic reactor channel (Reproduced with permission from Ref. Li et.al., Copyright Wiley-VCH Verlag GmbH & Co. KGaA, 2012)

Krishna et al. (Krishna et.al., 2013) have reported on the time-resolved mapping of the growth of gold nanostructures using similar millifluidic chip. The millifluidic chip used in their study had serpentine channel through which $HAuCl_4$ and DMSA solutions were fed at different flow times (such as 1, 3, 5, 7, and 9 h) to form different gold nano/ microstructures (Figure 3.13). The mixing of the precursors resulted in the formation of gold sulfide clusters of size 1–2 nm, which were later reduced by washing them with $NaBH_4$ solution. The authors have studied the *in situ* X-ray absorption spectroscopy (XAS) of the formation process of the gold nanoclusters (Figure 3.14) and also their further growth into microstructures. They have also demonstrated flow catalysis using the gold-deposited chips for the reduction of 4-nitrophenol and ferricyanide.

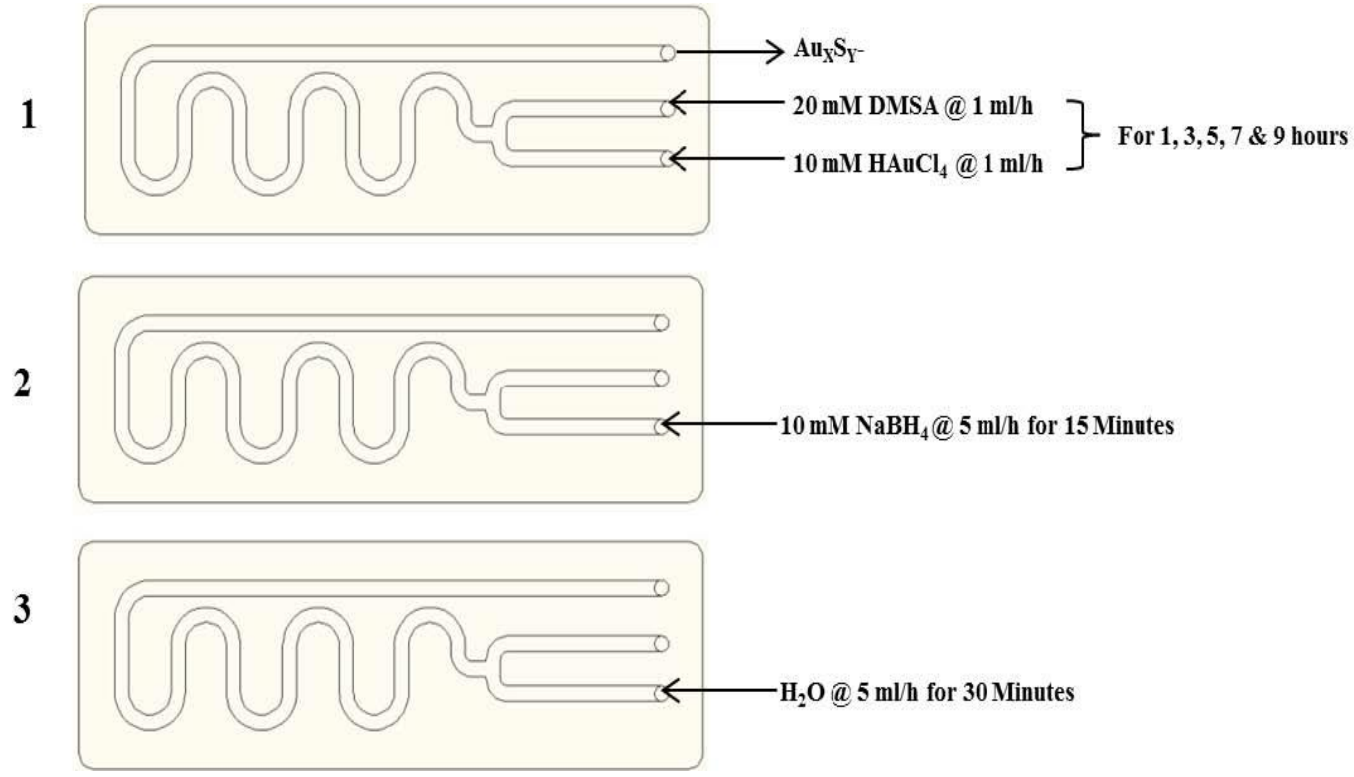

Figure 3.13. Schematic for the formation steps of gold structures within millifluidic reactor.

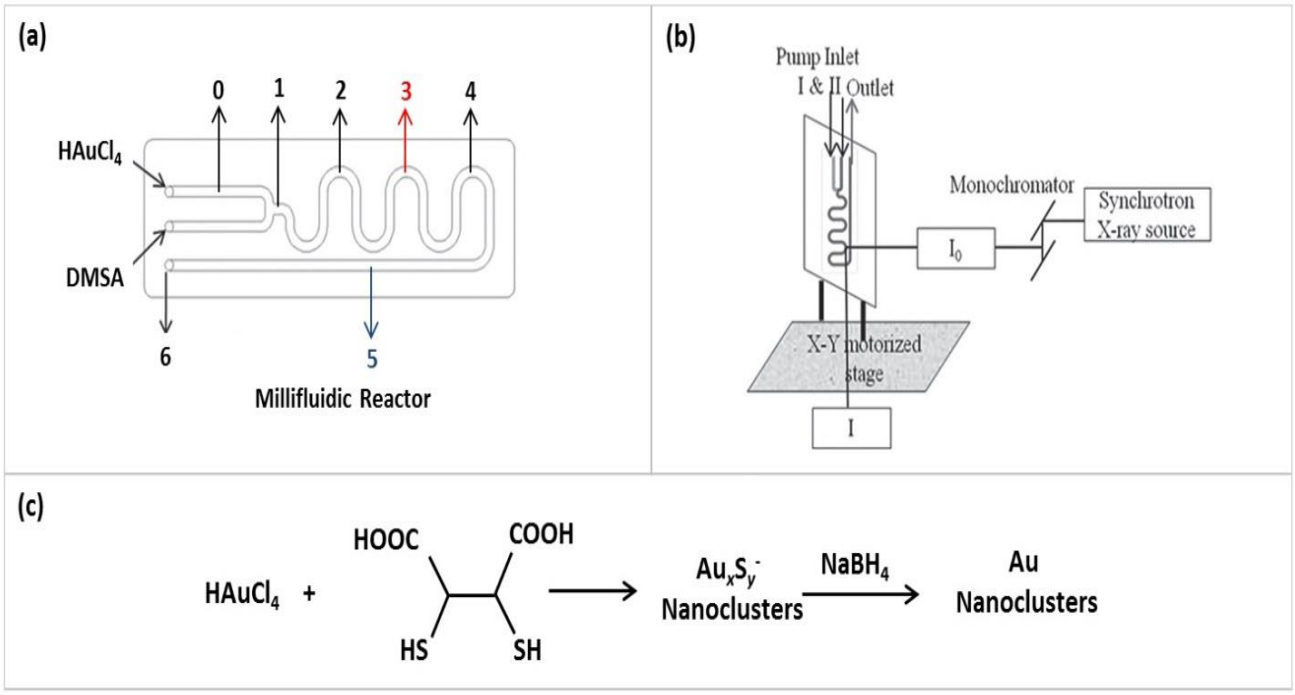

Figure 3.14. (a) Millifluidic chip marked with different zones where *in situ* XAS was performed. (b) *In-situ* XAS analysis at different zones within the millifluidic channel. (c) Reaction scheme of precursors. (Reproduced with permission from ref. Krishna et.al., Copyright ACS Publications, 2013)

Synthesis of gold NPs of size 5.6 nm using multistep microfluidic reaction system was reported by Ishizaka and coworkers (Ishizaka et.al., 2012). They used facile methods to synthesize highly dispersed gold NPs using three micromixers, which had two inlets each in order to prepare the gold NPs by $NaBH_4$ reduction. The precursor solutions, $HAuCl_4$ and N, N-dimethylacetamide (DMAc) solution of the poly-(amic acid) (PAA), were fed into the first Y-shaped micromixer using pumps to prepare a homogeneous mixed solution. This homogenous mixed solution was then fed simultaneously with the $NaBH_4$ solution to form the homogeneously dispersed gold NPs in the PAA solutions. Finally, a microemulsion was formed by feeding the resulting solution along with n-hexane. The microemulsion was then collected and heated in a

microheat exchanger, and a dispersion of the liquid containing polyimide NPs confining Au NPs were obtained after several processing procedures.

Kohler and coworkers (Kohler et.al., 2005) also reported a three-step mixing synthesis of gold NPs at room temperature using a microflow channel. Unlike the previous case, gold NPs synthesized by these authors used ascorbic acid as the reducing agent. There were three mixing zones for their synthesis process. In the first zone, the reducing agent, *i.e.,* the ascorbic acid (educt solution 1) and Fe (II) sulfate (educt solution 2) were mixed at low flow rates within the micromixer. The Fe (II) was then added to polyvinyl alcohol solution before the first mixing step. The second mixing zone had sodium metasilicate solution (educt solution 3) reacting with the mixture from the first step. Finally, 1 mM of $HAuCl_4$ (educt solution 4) was introduced to the mixture from the second step to form 5nmsized Au NPs.

Wagner and coworker (Wagner and Kohler, 2005) reported the synthesis of gold NPs with size ranges of about 5 to 50 nm using a hydrophobic continuous flow microreactor channel. The microreactor channel walls were made hydrophobic using trichloro (1H, 1H, 2H, 2H-perfluoro-octyl) silane. In their procedure, 1 mM of aqueous $HAuCl_4$ containing PVP was mixed with ascorbic acid within a microreactor as shown in the Figure 3.15. The reactant solutions were then fed into the micromixer by polypropylene syringe pumps, and the gold sol was collected separately through the mixer outlet. The pH of the reactant solution was altered in order to suppress microreactor fouling.

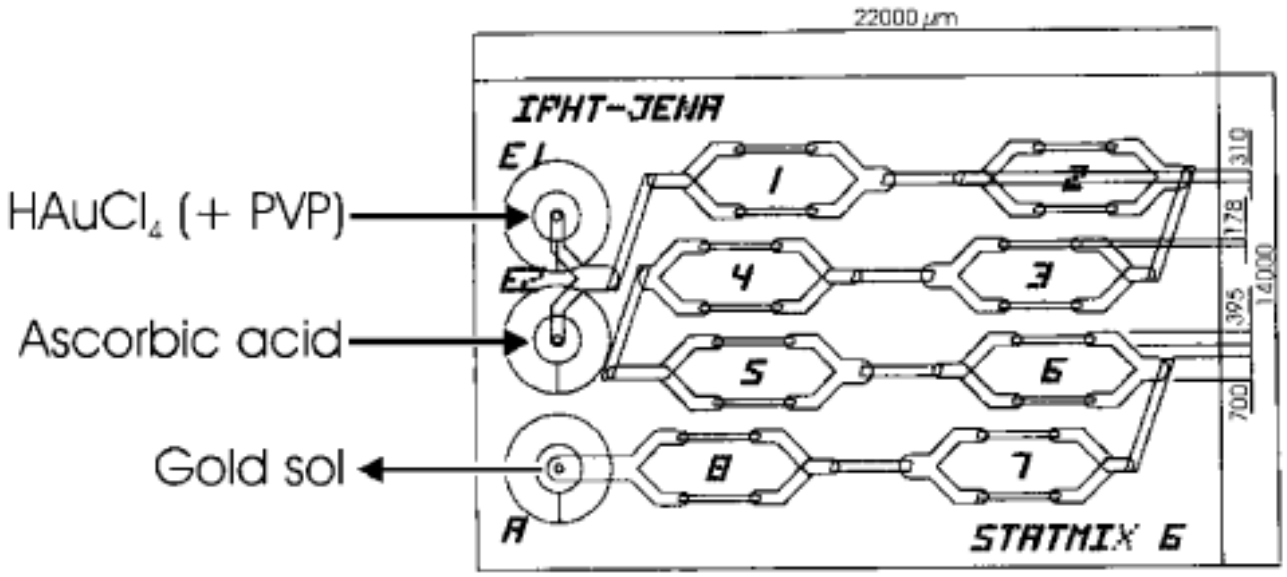

Figure 3.15. Schematic of the experimental setup showing the connectivity of the microreactor (STATMIX 6, area 22 x 14 mm). (Reproduced with permission from Ref Wagner et.al., Copyright ACS Publications, 2005)

Similar to the work carried out by Wagner and group (Wagner and Kohler, 2005), Cabeza and coworkers (Cabeza et.al., 2012) also synthesized gold NPs by controlling their size with a segmented flow microfluidic platform under hydrophobic conditions (Figure 3.16). The channel of the microfluidic platform was pre-coated with poly(tetrafluoroethylene) (PTFE) hydrophobic layer in order to study the effect of axial dispersion of the gold NPs size distribution. Segmented flow of reagents were achieved by feeding three separate streams of reactants *viz*. $NaBH_4$, aqueous mixture of chloroauric acid and tetracyltrimethylammonium bromide (TTABr), and the third stream had either air, toluene, or silicone oil. The process was carried out for 10, 20, and 40 s, and different flow rates were maintained for each reagent to get particle sizes of 3.8 ± 0.3, 4.6 ± 2.1, and 4.9 ± 3.0 nm, respectively

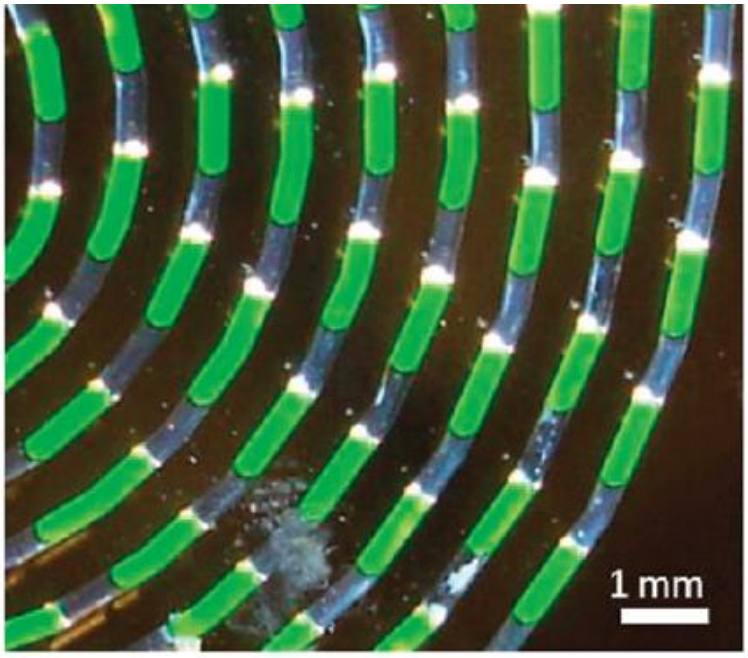

Figure 3.16. The hydrophobic microchannel (water is the dispersed phase). Fluorescein was added to the aqueous phase to improve the optical resolution. (Reproduced with permission from Ref Cabeza et.al., Copyright ACS Publications, 2012)

Yet another hydrophobic-channeled poly(dimethylsiloxane) (PDMS) microfluidic device was used by Lazarus and coworkers (Lazarus et.al., 2010) for synthesizing monodisperse gold NPs of size 4.3 ± 0.5 nm. In this process, an interdiffusion between the two reagent streams, *i.e.*, chloroauric acid/1-methylimidazole and $NaBH_4$ in 1-butyl-3-methylimidazolium tetrafluoroborate (BMIM-BF_4) was achieved by injecting a stream of pure BMIM-BF_4 using a syringe pump at various flow rates through different inlets. In addition, inert oil (polychlorotrifluoroethylene) was pumped into the microfluidic device to define the flow regimes of the reagent stream, and the final product was collected through the outlet in ethanol.

In a different procedure, Duraiswamy and coworkers (Duraiswamy and Khan, 2009) reported the synthesis of gold NPs of sizes < 5 nm using droplet microfluidics in order to prevent the contact between the solutions and the microreactor channel walls. Their procedure involved

the production of zero-valent gold (Au^0) NPs by reducing trivalent gold (Au^{3+}) chloride with ascorbic acid in the presence of CTAB as the surfactant. The seed and the reagent solutions were fed into the microfluidic mixer at equal flow rates. The gold NP seed suspension and the aqueous reagent solutions were mixed rapidly by chaotic advection within the T-junction microfluidic device to form droplets. Silicone oil was fed along with the seed and the growth solutions through a separate arm of the T-junction device (Figure 3.17), which prevented contact of the growing particles with the microchannel walls by forming a thin lubricating layer around the droplets. The droplets were then collected separately in a sampling reservoir and aged to ensure growth completion.

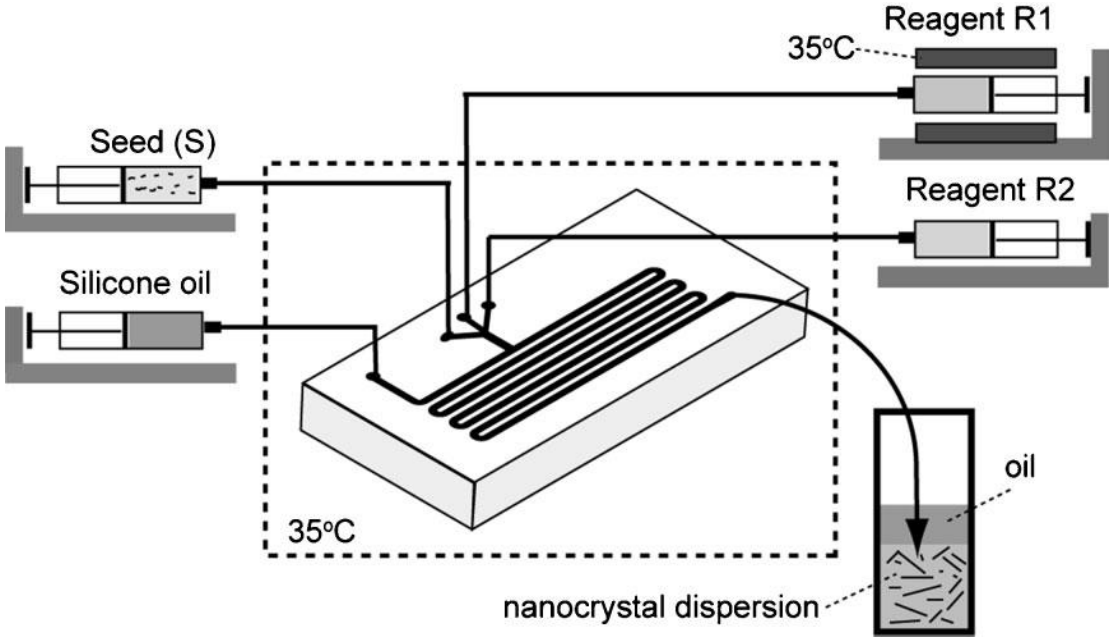

Figure 3.17. Schematic of the experimental setup for the production of gold nanoparticles. (Reproduced with permission from Ref Duraiswamy et.al., Copyright John Wiley and Sons 2009)

Boleininger and coworkers (Boleininger et.al., 2006) used microfluidic mixers to synthesize gold NPs with a high concentration of CTAB, which acts as the surfactant for forming

rod-shaped gold particles. Millimolar concentration of the spherical metal seed crystals in aqueous growth solution ($HAuCl_4$) was mixed with ascorbic acid in the micromixer. These metal seeds were produced by reducing the metal salt with freshly prepared $NaBH_4$. The flow rates of the growth solution and the seeds were maintained independently using the syringe pumps. The seed crystals were allowed to grow at a fixed temperature by directing the seed and the growth solution mixture from the microfluidic device through a temperature-controlled tubing and collected separately.

Another report by Jun and coworkers (Jun et.al., 2012) describes the synthesis of gold NPs of final size range from 3 to 35 nm (Andreescu et.al., 2006) through a wet chemical synthesis technique using both millifluidic and microfluidic mixers at room temperature (Figure 3.18). The precursor solution $HAuCl_4$ was mixed with ascorbic acid (whose pH was adjusted with a calculated amount of NaOH). Rapid mixing of these solutions was achieved by feeding them into the millifluidic mixer aided by two syringe pumps. A separate glass vessel was used to collect the colloidal gold solution for further analysis. The reactants were mixed at various flow rates in order to investigate its effect on the gold NPs synthesis. Ball-Berger mixer was used to achieve very fast mixing conditions for high flow rate reactions (Berger et.al., 1968), whereas a butterfly mixer built with poly(dimethylsiloxane) (PDMS) microchip was connected to the syringe pump for low flow rate reactions (Lu et.al., 2010), and the colloidal gold solution obtained was collected through the microtube outlet.

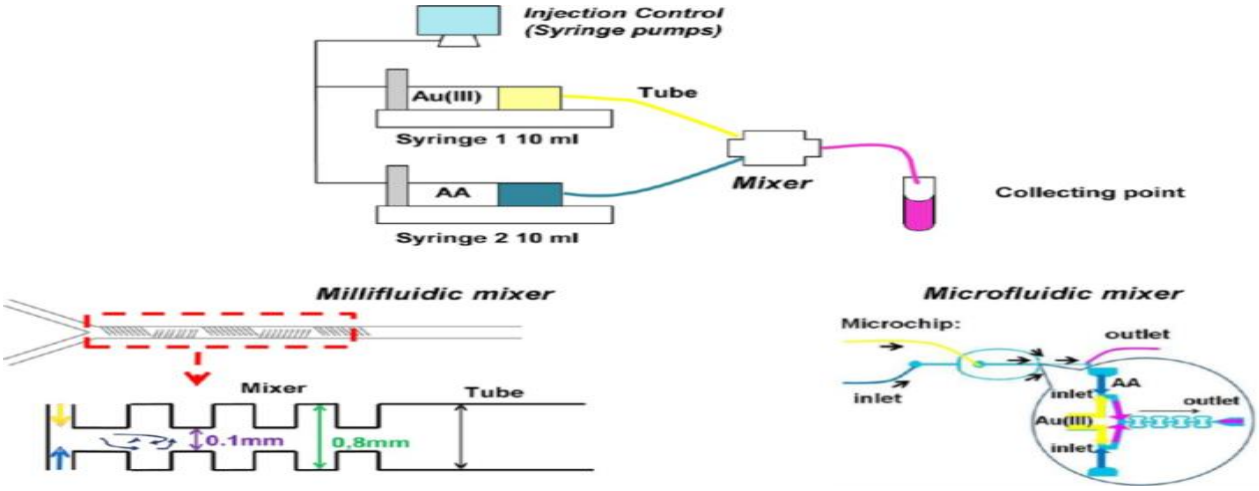

Figure 3.18. Illustration of the experimental setup. The mixer can be a pressed Teflon tube (millifluidic mixer) (7 or 22 cm length) (left), a Ball-Berger mixer (not shown) or a microfluidic mixer with a butterfly geometry (right). (Reproduced with permission from Ref Jun et.al., Copyright ACS Publications, 2012)

Kitson and coworkers (Kitson et.al., 2012) reported the synthesis of gold NPs of size 10 nm using a 3D-printed millifluidic and microfluidic devices. These 3D-printed reactors had two and three inlets for introducing the reactant solutions (Figure 3.19). Gold NPs were synthesized using a premixed solution of aqueous $HAuCl_4$ and sodium citrate. The solutions were fed into the 3D reactor through the first inlet and mixed with $NaBH_4$, which was fed simultaneously through the second inlet. The formation of the gold NPs was observed by in-line UV-Vis spectroscopy, which decreased over time due to the gold deposition over the channel walls.

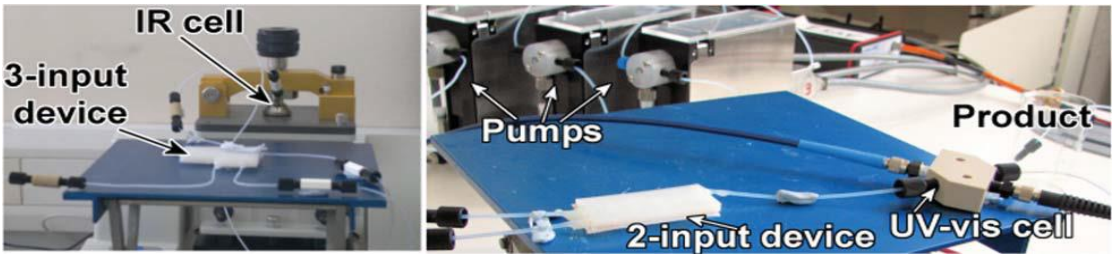

Figure 3.19. The devices with three inlets each connected to a pump, and the in-line ATR-IR and/or UV-Vis flow-cells connected to the outlet. (Reproduced with permission from Ref Kitson et.al., Copyright ACS Publications, 2008)

Weng and coworkers (Chen-Hsun et.al., 2008) reported the synthesis of citrate-based gold NPs of size 35 ± 2 nm using PDMS based microfluidic device. They used a pneumatic rotary micromixer with four peristaltic membrane layouts for the synthesis of hexagonal gold NPs with trisodium citrate as the primary reducing agent. Trisodium citrate and preheated-$HAuCl_4$ solutions were fed within the micromixer and mixed vigorously to obtain a ruby red solution, which was then heated to 115°C for the reaction completion. Different heating times and concentrations of the $HAuCl_4$ and tri-sodium citrate were also tested within the micromixer to synthesize the hexagonal gold NPs with different sizes. Similar to the previous report, Yang and coworkers (Yang et.al., 2010) used a microfluidic chip on a thermoelectric (TE) device to synthesize gold NPs with different sizes (19, 28, 37, and 58 nm) by manipulating the volumes of the reactant, *i.e.,* chloroauric acid and trisodium citrate at a constant reaction temperature of 100^{o}C. A cone-shaped condenser was placed on top of the chamber after the reagents were mixed into it to maintain a constant reactant concentration. A micropump was used to inject the sodium citrate, and a vortex-type micromixer was used to stir the reagents in the mixing chamber in order to form gold NPs by reducing the chloroauric acid solution, which was observed by a color change from light yellow to ruby red. The reaction process was carried out for 10 min before the solution was cooled down to room temperature.

3.6.3. Gold nanocatalysts supported within LOC systems

In the previous section, various synthetic protocols that have been used for making gold NPs using the LOC systems were summarized. This section is focused on gold NPs that are supported within the LOC devices for catalysis. The gold NPs catalysts were either prepared *in situ* enabling attachment to the channel walls or synthesized using conventional methods and

loaded or immobilized over the channels of the LOC systems (Figure 3.2). Loading the gold NPs into the LOC systems are carried out by various methods. For example, Abahmane and coworkers loaded the gold nanocatalysts into the capillaries and packed it by supporting vibrations (Abahmane et.al., 2011). Similarly, dip coating the internal surface of the capillary (Protasova et.al., 2011), calcination (Juarez et.al., 2011), crosslinking the copolymer to the gold NPs (Wang et.al., 2009; Miyamura et.al., 2007), spin-coating techniques (Adleman et.al., 2009) were used in order to make gold nanocatalyst-supported LOC systems.

Synthesis of polypyridine derivatives using alumina supported gold NPs of size 2 nm using microcontinuous flow conditions has been reported by Abahmane and coworkers (Abahmane et.al., 2011). After supporting the gold NPs on Al_2O_3 through impregnation, the heterogeneous catalysts were used in the microcontinuous flow system (Figure 3.20) as the packed bed capillary reactor (PBCR). Reactants were fed through the PBCR under optimized continuous flow conditions to retrieve the products.

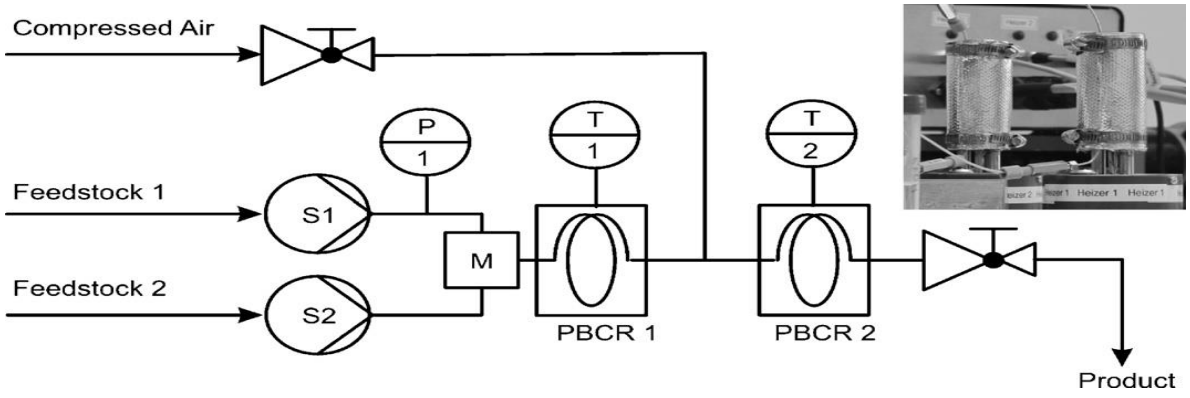

Figure 3.20. Micro continuous flow setup (feedstock 1: bis-α-H-ketone solution, feedstock 2: propargylamine solution; M: micro mixer; PBCR1, PBCR2: packed bed capillary reactors (ID: 1mm, 50cm length); P: pressure sensor; T1, T2: temperature sensors; S1, S2: syringe pumps). Inlay: image of the PBCRs. (Reproduced with permission from Ref Abahmane et.al., Copyright Elsevier, 2011)

The authors also reported the synthesis of pyridine (Abahmane et.al., 2009) and propargylamines (Figure 3.21) (Abahmane et.al., 2011) using similar continuous microflow system packed with gold NPs-impregnated alumina.

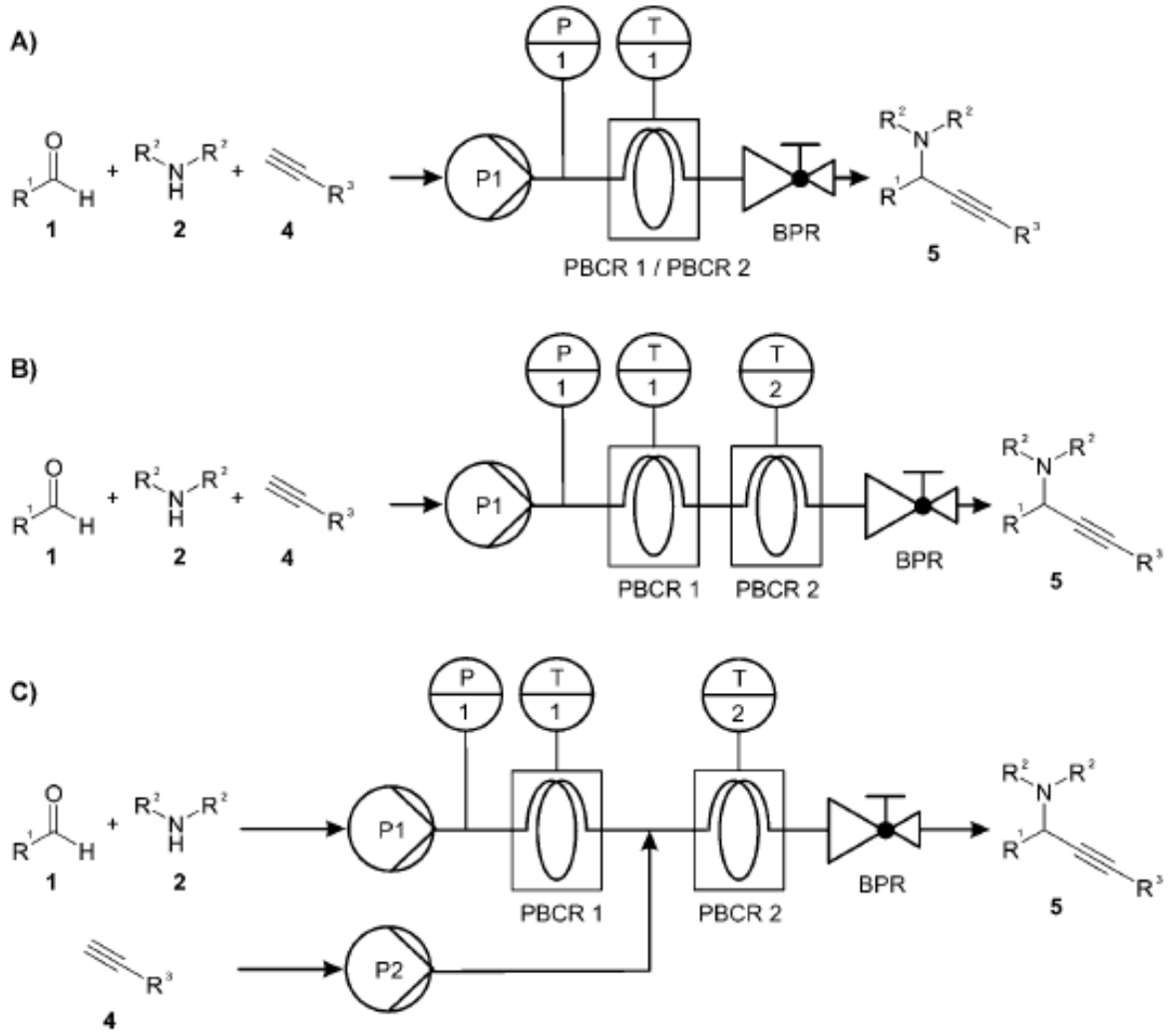

Figure 3.21. Flow chemistry set-up schemes for the different reaction regimes A–C. P1, P2 pumps; P(1) pressure sensor; T(1), T(2) temperature sensors; PBCR1 (Montmorillonite K-10) and PBCR2 (Au-NP@Al_2O_3): packed-bed capillary reactors; BPR: back-pressure regulator. (Reproduced with permission from Ref Abahmane et. al., Copyright John Wiley and Sons, 2011)

Packed bed capillary reactors were also used for liquid phase hydrogenation of citral on Au/TiO_2 thin films within capillary microreactors by Protasova and coworkers (Protasova et.al., 2011). Gold NPs of size 4.5 ± 0.5 nm prepared by $NaBH_4$ reduction were doped on titania films to form the Au/TiO_2 sol. The coating of Au/TiO_2 sol within the capillary reactor was done after pretreatment and calcination processes and used to study the kinetics of citral hydrogenation. A similar Au/TiO_2 catalyst was reported by Cao and coworkers (Cao et.al., 2011). They used Au-Pd over TiO_2 for benzyl alcohol oxidation within the microstructured reactors (Figure 3.22). The Au-Pd/ TiO_2 catalyst was prepared separately and loaded into the microreactors and was later used for catalytic studies.

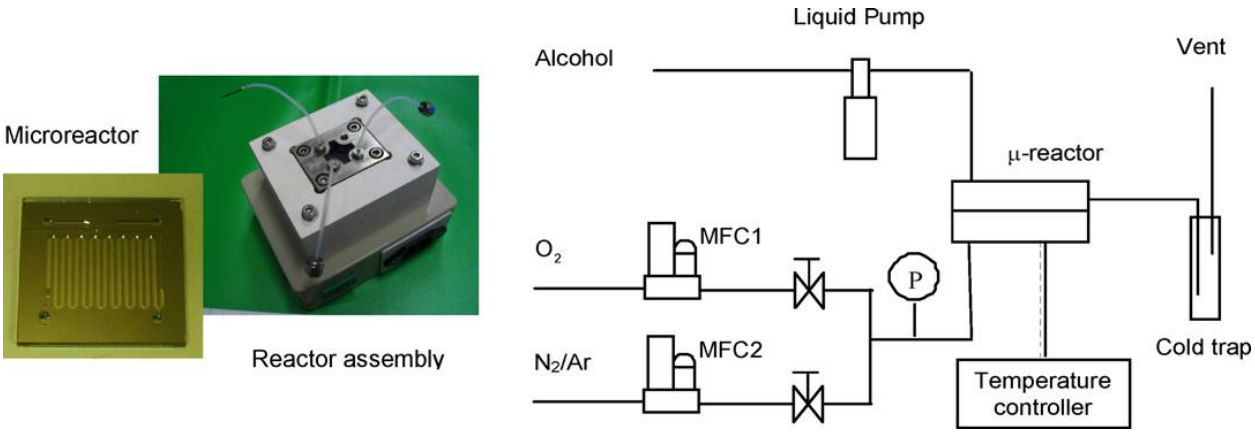

Figure 3.22. Microreactor, reactor assembly with temperature control and the schematic of the experimental setup (Reproduced with permission from Ref Cao et.al., Copyright Elsevier, 2011)

Juarez and coworkers (Juarez et.al., 2011) reported the continuous flow carbamoylation of aniline by dimethyl carbonate using Au/CeO_2 of size 3-4 nm within a microreactor (Figure 3.23). The Au NPs supported on CeO_2 support was prepared using conventional wet impregnation method, coated within the stainless steel microreactor plate and used for carbamyoylation reaction.

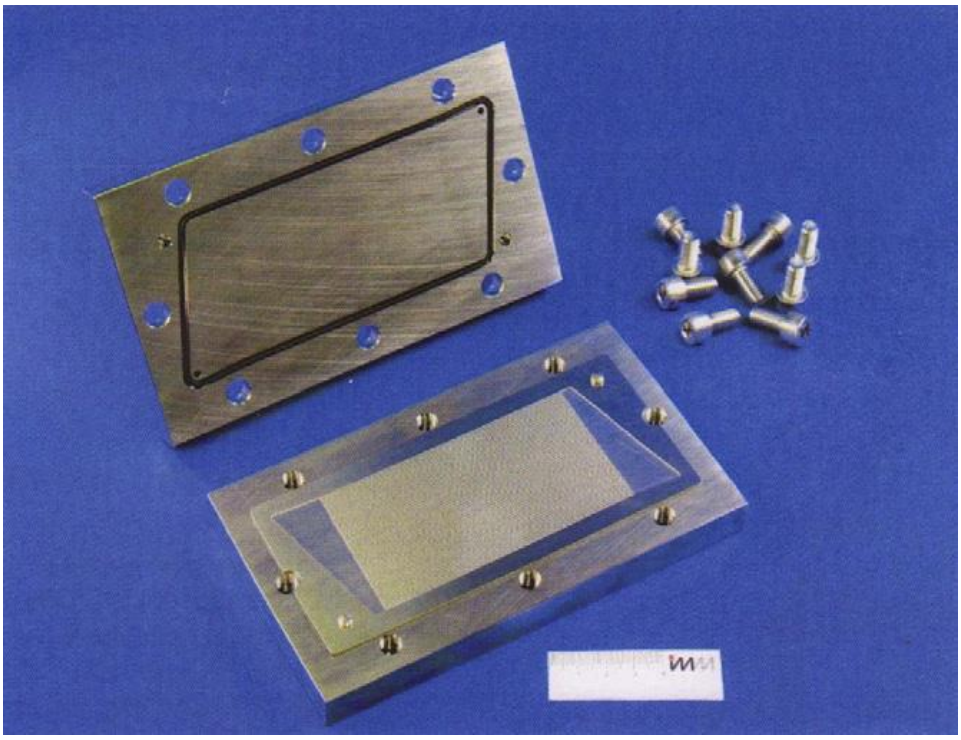

Figure 3.23. Parts of the microreactor showing the microchannel plate coated with a thin film of nanoparticulated ceria (Reproduced with permission from Ref Juarez et.al., Copyright Elsevier, 2011)

Wang and coworkers (Wang et.al., 2009) reported the oxidation of alcohols with molecular oxygen using the gold-immobilized mirochannel flow reactor. Microencapsulated gold prepared from chlorotriphenylphosphine gold ($AuClPPh_3$) and copolymer in THF solution, was used as a gold source for the immobilization (Miyamura et.al., 2007). Gold was immobilized on the capillary column reactor by reducing the cyanopropyl groups using lithium aluminum hydride to the corresponding amine (Figure 3.24). The modified capillary column was pumped with a colloidal solution of the microencapsulated gold and heated to 170°C for 5 h in order to have a crosslinking of the copolymer to result in the gold immobilization, which was further used for oxidation studies (Figure 3.25).

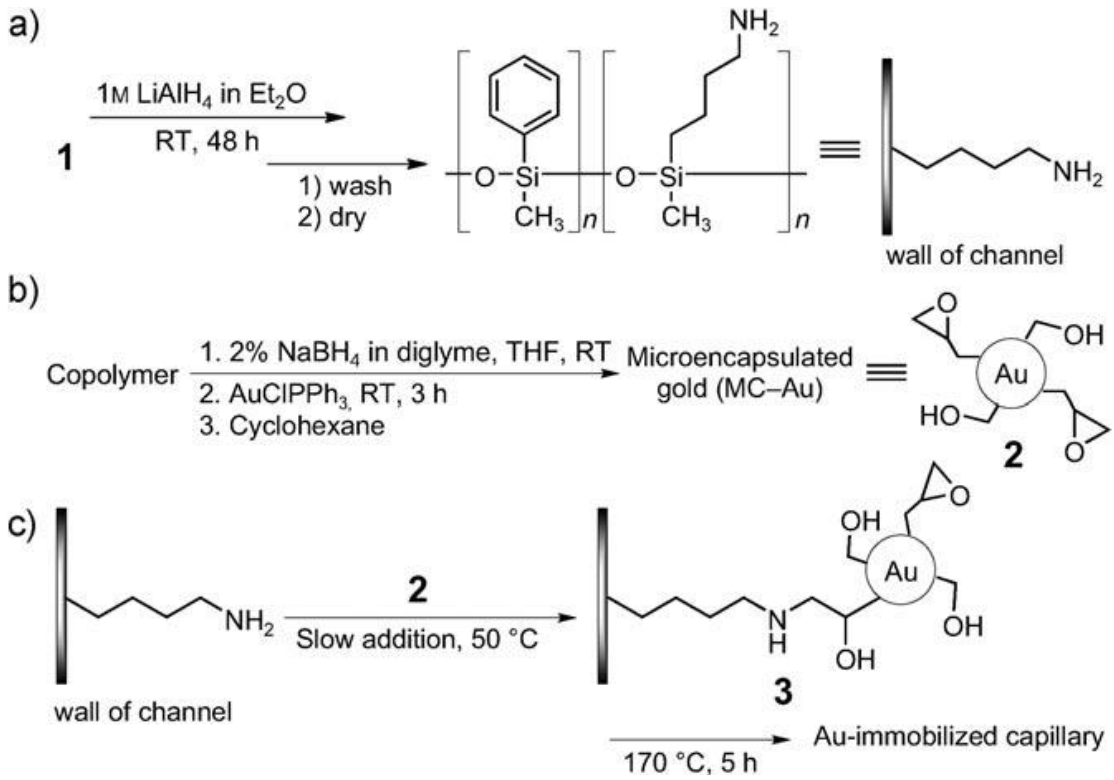

Figure 3.24. Immobilization of the gold catalyst. a) Reduction of the cyano group to an amine. b) Preparation of microencapsulated gold. c) Immobilization of the gold catalyst. (Reproduced with permission from Ref Wang et.al., Copyright John Wiley and Sons, 2009)

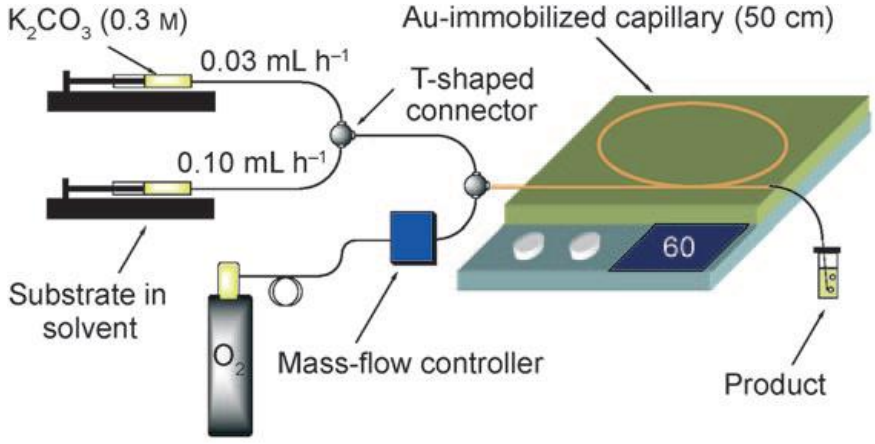

Figure 3.25. Experimental setup of the gold-catalyzed oxidation reactions (Reproduced with permission from Ref Wang et.al., Copyright John Wiley and Sons, 2009)

Apart from using immobilized gold nanocatalyst prepared through the bottom-up approaches, gold NPs synthesized using the top-down method were also used within the

microfluidic reactors for catalytic applications. For example, Adleman and coworkers (Adleman et.al., 2009) carried out heterogeneous catalysis mediated by plasmon heating with gold NPs of estimated average diameter size of 20 ± 5 nm prepared by lithography and immobilized over a glass microscope slide, which was temporarily bonded to PDMS. Figure 3.26 shows the schematic of gold NPs immobilized on the microfluidic channel attached to the PDMS support.

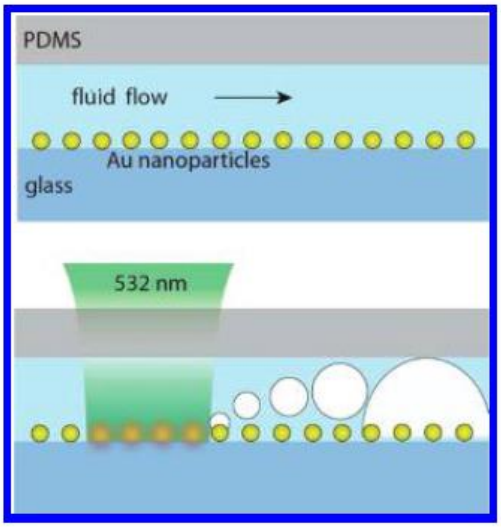

Figure 3.26. Schematic of the catalytic process (side view). A microfluidic channel with gold nanoparticles attached to a glass support; fluid flows from left to right. (Top) A laser at or near the frequency of the plasmon resonance of the gold nanoparticles is focused on the top of the support, and the subsequent heat generated in the nanoparticles is transferred to the surrounding fluid and forms vapor. The vapor phase components react on the catalyst forming gas bubbles which are carried downstream. (The channel height is 40 μm and the radius of the nanoparticles is ~10 nm.) (Reproduced with permission from Ref Adleman et.al., Copyright ACS Publications, 2009)

Krishna et al. (Krishna et.al., 2013) have demonstrated reduction reactions of 4-nitrophenol and ferricyanide using a gold microstructures-coated millifluidic chip. The authors achieved ~92% conversion of the reactants using gold-coated chip compared to 20% conversion using a chip without gold coating within the channel. Their gold catalysts were also reusable up to 40 catalytic cycles (80 h), which established significant advantage of their flow catalytic process.

There are some challenges that need to be addressed when a NPs-supported LOC device is used for catalytic conversion reactions. While loading a metal catalyst like gold NPs onto a support or a reactor, there are chances that these particles might lose their functional activity and selectivity due to environmental conditions. For example, while immobilizing the NPs onto a substrate, proper pretreatment procedures have to be carried out in advance in order to have an improved catalyst attachment. There are chances that the catalyst might undergo agglomeration due to the thermal pretreatment like calcination, mechanical vibrations, etc.

3.7 Conclusions and future perspective

Controlled synthesis of Au NPs with better stability and selectivity either by top-down or bottom-up approach is very important for their application as catalysts. Advances in synthetic protocols for Au NPs from conventional methods to LOC systems have proven to be successful with respect to control over their size, size distribution, and shape. Facile synthesis of Au NPs using LOC devices has been favorable due to the possibility for easy manipulation of reagents and reaction conditions along with the possibility for in-line characterization during synthesis. While the LOC-based synthesis of gold NPs has not produced better quality materials in comparison with traditional flask-based synthesis, the ability to combine synthesis with in-line probing of the reaction offers a distinct advantage in LOC devices. Therefore, the application of LOC devices for synthesis and characterization of gold NPs could lead to new analogs based on their structure (size distribution, shape, porosity), and functional properties (stability, catalytic activity) in the near future. As the synthetic efforts are currently being directed toward the synthesis of atomically precise gold catalysts, we anticipate a bigger role for the development of

LOC devices for these investigations. With the option to study time-resolved particle growth within the millifluidic channels, the synthesis conditions can be well controlled to investigate the surface growth kinetics of the gold NPs (Li et.al., 2012; Krishna et.al., 2013) and to prepare atomically precise gold NPs. As discussed in the chapter with several examples, the use of LOC systems with control over the residence time, precursor volume and concentration, and surfactant, surface modifications would definitely create a paradigm shift in designing unique Au NPs catalysts.

From the extensive literature presented in this chapter, it is clear that LOC devices offer many opportunities for flow catalysis based on gold NPs. This opportunity is particularly attractive as a large number of gold catalyzed organic and inorganic reactions (Hashmi and Hutchings, 2006; Toste, 2011; Coquet et.al., 2008; Rudolph and Hashmi, 2012) are yet to be exploited using continuous flow catalysis based on LOC devices. It is now well established that gold is effective for reactions under mild conditions, particularly CO oxidation, which is possible at sub-ambient temperatures. We hope that flow catalysis of such heterogeneous reactions will be carried out in the near future (Min and Friend, 2007). With the ability to probe reactions within LOC devices with unparalleled time- resolution using various spectroscopy tools, one can foresee investigations to unravel the mechanism of gold-catalyzed reactions (both solution phase as well as gas phase) ranging from fine chemical conversions to more complicated biomass conversion processes. The discovery that incorporating a second metal as an alloy with gold can enhance the catalyst performance (Hutchings and Kiely, 2013) is anticipated to lead to further utilization of LOC based approaches for both synthesis and flow catalysis of gold-based bimetallic nanocatalysts.

CHAPTER 4: MILLIFLUIDICS FOR CONTINUOUS FLOW SYNTHESIS AND TIME-RESOLVED IN-SITU X-RAY ABSORPTION SPECTROSCOPY INVESTIGATION OF PLATINUM-DMSA NANOPARTICLES

4.1 Introduction

Synthesis and characterization of metal sulfides for catalytic applications has been well-known for over a century ever since Che et al. reported the transition metal sulfide catalysis in 1912 (Che, 2003). In recent times, Weisser et al. investigated the hydrogenation of coal using transition metal sulfide catalysts (Weisser and Landa, 1973). Following these investigations, transition metal sulfide catalysts have started to gain importance for various applications such as hydrogenation of olefins, ketones and aromatics; alkylation; hydrodenitrogenation; hydrocracking; hydrodemetallation; and ring opening of aromatics (Topsee et.al., 1996). The catalytic activity of these transition metal sulfide materials is related to their surface chemistry, which is primarily determined by the bulk atomic and electronic structure (Harris and Chianelli, 1984; Harris and Chianelli, 1983; Harris and Chianelli, 1986). In addition, factors such as metal-sulfur bond strength, optimum heat of formation of the sulfide (Benard et.al., 1979), Pauling percentage d-character, and degree of covalency of the metal-sulfur bond (Harris and Chianelli, 1983) also contribute to their surface chemistry.

To date, techniques to synthesize monodisperse-sized metal sulfide nanoparticles using batch reactors have been relatively complex due to limitations such as non-uniform reactor conditions (i.e. temperature, mixing), and lack of in-situ reaction monitoring. However, these limitations can be addressed with the use of lab-on-a-chip (LOC) systems based on millifluidic reactors. Advances in millifluidics-based reactor technologies have brought opportunities to investigate the synthesis of nanoparticles and explore continuous flow catalysis of a variety of

chemical reactions (Krishna et.al., 2013). These reactors also offer the possibility to acquire real-time in-situ experimental data at various spatial intervals with the ability to convert spatial resolution into time resolution (Krishna et.al., 2013). Information obtained using such time-resolved in-situ measurements provide insight into the reaction kinetics for extremely fast reactions. For instance, we recently reported, the utility of a simple millifluidic chip for an in-situ analysis of morphology and dimension controlled growth of gold nanostructures with a time resolution of 5 ms (Krishna et.al., 2013). While these previously reported investigations were focused on metallic nanoparticles (i.e. gold), in the present report, we made an attempt to utilize the technique to analyze the time-resolved growth of ultra-fast formation of metal sulfide (Pt(DMSA)) nanoparticles to demonstrate its general applicability.

Platinum metal sulfide nanoparticles are used in important catalytic applications such as hydrogenation, hydrodesulfurization, etc. under high pressure conditions (Pecorar and Chianelli, 1981; Chiang et.al.,1991; Eijsbouts et.al., 1988). However, chemical procedures for synthesizing these nanoparticles have been relatively complex due to experimental limitations such as the need for longer reaction time, and high temperature, and pressure conditions (Paraspour et.al.,1998; Malik et.al., 2002). While yielding high quality platinum metal sulfide nanoparticles, these methods are also difficult to carry out due to use of toxic reagents as well as due to expensive synthesis procedure. A detailed analysis of existing techniques for the synthesis of platinum metal sulfide nanoparticles reveal protocols that lack ambient temperature and pressure based experimental conditions within an aqueous medium. With this in mind, we report a new approach to carry out continuous flow synthesis of Pt(DMSA) nanoparticles under ambient conditions using the millifluidic reactor. In addition, the formation of Pt(DMSA) nanoparticles

within the millifluidic reactor channel was monitored in real-time with in-situ XAS to investigate their nucleation and growth mechanism at selected spatial and time-intervals, which would be difficult using traditional batch reactors. Although, there are several reports on the synthesis of nanoparticles of various platinum sulfides (Malik et.al., 2002; Kliche, 1985) such as PtS, Pt_2S_3, PtS_2, PtS_{10}^{2-}, PtS_{15}^{2-}, PtS_{17}^{2-} and PtS_{18}^{2-}; to our knowledge there are no reports monitoring their synthesis until now. Therefore, here we demonstrate an approach to synthesize Pt(DMSA) nanoparticles and real-time in-situ analysis of their growth whilst only requiring small volumes of reactants and short reaction times.

4.2 Materials and Methods

4.2.1 Experimental section

4.2.1.1 Chemicals

Chloroplatinic acid hexahydrate ($H_2PtCl_6.6H_2O$, 99.9%, Strem chemicals), meso-2,3-dimercaptosuccinic acid (DMSA, 97%, Alfa Aesar), Sodium hydroxide (NaOH, 98.6%, Macron chemicals), sodium borohydride ($NaBH_4$, 98%, Aldrich) and Ethanol (EtOH, 200 proof) were purchased. All chemicals were used as received without further purification. Nanopure water was used for all the experiments.

4.2.1.2 Millifluidic reactor set-up

The millifluidic device and the millifluidic reactor chip were purchased from Millifluidica LLC. The channel dimensions of the chip were 2 mm wide, 0.15 mm in depth and 220 mm in length. The millifluidic device was tested with water as solvent at different flow rates prior to the experiment to optimize the required flow rate.

4.2.2 Experimental concept and design

4.2.2.1 Synthesis of ultra-small platinum sulfide nanoparticles using a millifluidic reactor

The Pt(DMSA) nanoparticles were prepared using standard solutions of H_2PtCl_6 (30 mmol), DMSA (60 mmol) and $NaBH_4$ (30 mmol). 10 ml each of H_2PtCl_6 and DMSA solutions were taken into two separate vials and were passed within the millifluidic chip with a uniform flow rate of 3.0 and 0.2 ml/min and the resulting Pt(DMSA) nanoparticles were collected and investigated using UV-Vis spectroscopy. In addition, HRTEM analysis was done in order to determine the morphology and size of these nanoparticles. Following these analyses, the growth process of Pt(DMSA) nanoparticles at room temperature was monitored using in-situ XAS in order to accurately determine its chemical features. For this purpose, a millifluidic chip attached with the millifluidic device was coupled to the synchrotron beam line using a metal stage that had access to movement in XYZ directions. Standard H_2PtCl_6 and DMSA solutions were passed within the millifluidic reactor channel at a volumetric flow rate of 3.0 and 0.2 ml/min (include any one flow-rate here) using the millifluidic device to initiate the nucleation of Pt(DMSA) nanoparticles. During the course of the reaction within the millifluidic channel, the conversion leading to the Pt(DMSA) nanoparticles was recorded using XAS and the resulting solutions were collected separately in a vial.

Following the XAS analysis, the obtained Pt(DMSA) nanoparticles colloid was reduced with $NaBH_4$ and purified by mixing ethanol. The mixture was further washed with Nanopure water and centrifuged at 5000 RPM for 10 minutes several times to remove impurities and dried overnight to remove moisture. In this procedure, $NaBH_4$ was used to promote good settling characteristics for Pt(DMSA), whereas, in the typical methods, $NaBH_4$ is used as a reducing

agent in order to provide a simple and efficient method for metal precipitation and recovery [1]. The addition of $NaBH_4$ to Pt(DMSA) nanoparticles colloid did not have any effect on the reduction of metal contaminant to their elemental form which was confirmed using EDS, STEM-EDS and XAS experiments. The purified Pt(DMSA) nanoparticles powder was characterized using XRD, FTIR, and XPS to obtain additional information.

4.2.3 Instrumentation

4.2.3.1 X-ray absorption spectroscopy (XAS)

Pt L_3-edge (11564 eV) X-ray absorption measurements were conducted at the 10ID beamline at the Advanced Photon Source, Argonne National Laboratory, Chicago. A rhodium coated harmonic rejection mirror was used to eliminate higher energy photons. Experiments were performed in fluorescence mode using an ion chamber with Stern Heald geometry. A mixture of 50% He and 50% N_2 gas was used in the initial ion chamber (I_o) placed before the sample and 100% N_2 gas in transmission and reference ion chambers. Argon gas was used for the fluorescence ion chamber. The gases in the ion chambers were optimized for adequate absorption of photons. Pt metal foil was measured using the reference ion chamber for every scan taken for energy calibration. The spot size of the x-ray beam on the sample was 300 µm x 300 µm. Before the start of the experiment, the millifluidic chip was mapped and different zones were selected for the XAS measurements. XANES and EXAFS measurements were done in quick scanning mode, with fixed undulator gap and taper while scanning the Bragg angle of the double crystal monochromator (with Si(111) crystal) with constant speed. Several scans were taken at each zone.

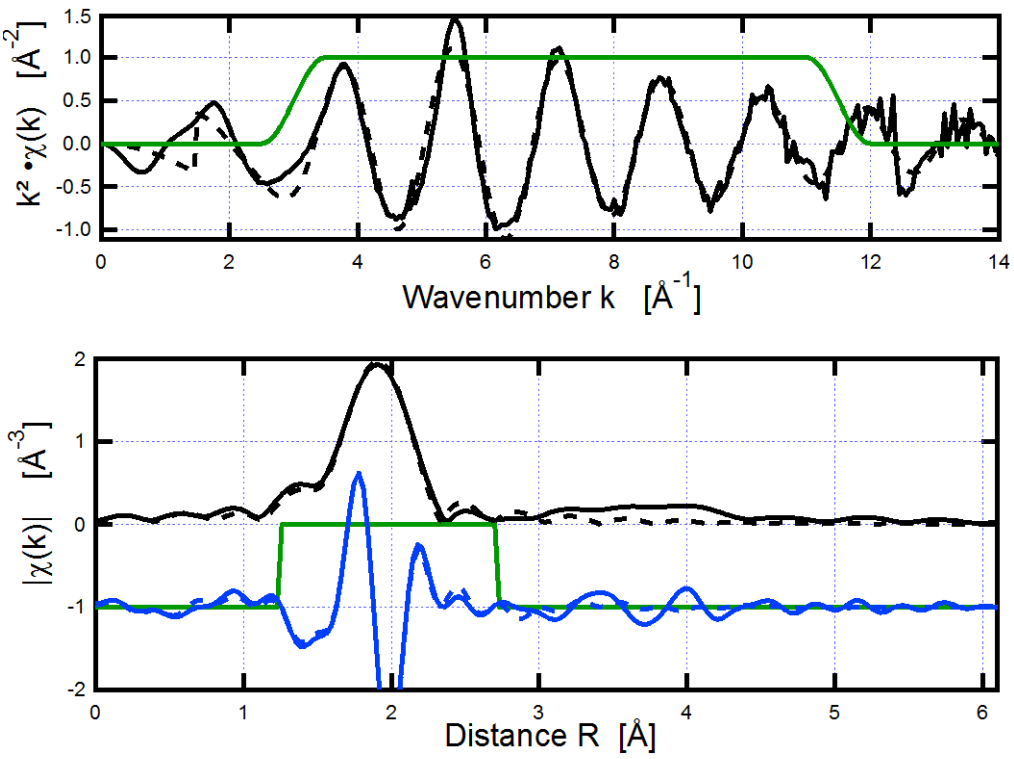

Fig 4.1: Pt(DMSA) nanoparticle k-space EXAFS data (not phase corrected)

The spectrum of metallic platinum (Pt foil) was used as a standard for energy calibration by setting the maximum of the first peak of the derivative of the spectrum to an energy of 11564 eV. XANES data were normalized and analyzed with the ATHENA program of the IFFEFIT package. Using the crystallographic data of PtS as input the FEFF 9 code was employed to simulate the Pt L_3-edge XANES spectrum of PtS. Standard parameters were used: e.g. no core hole, Hedin-Lundquist exchange potential, full multiple scattering (FMS) radius of 10 Angstrom. EXAFS data processing and analysis were performed using the demeter package. The theoretical paths were generated using FEFF6 and the models were done in the conventional way. Fitting parameters were obtained by modeling the EXAFS data of each sample in R-space until a satisfactory fit describing the system was obtained. The EXAFS data quality was good for the Pt foil up to a k-range of 17 $Å^{-1}$. The data quality for the Pt colloid synthesized using the

millifluidic reactor was poorer with a useable k-range only up to 11.5 $Å^{-1}$ due to noise. In order to reduce the effect of high k-values, k^2 fitting was applied. The fitting parameters were adjusted applying several conditions to the analysis. The amplitude reduction factor (SO2) was determined using the EXAFS data of the Pt foil as SO2 = 0.936 and was set constant. The coordination number (N), bond length (d), and value of thermal disorder σ^2 (Debye Waller Factor) for the first shell Pt-S were varied independently.

4.2.3.2 High Resolution Transmission Electron Microscopy

The high resolution imaging as well as EDS data was obtained using JEOL 2010 F-FasTEM which is a HRTEM with a zirconated tungsten thermal field emission tip. It is also equipped with a 2K x 2K Gatan CCD bottom mount camera. All the measurements were performed at an accelerating voltage of 200kV and in bright field mode. EDS mapping was performed using FEI Titan 80-300 probe aberration corrected scanning transmission electron microscope (STEM) which is equipped with high annular dark field detector (HADDF) STEM and ChemiSTEM. The combination of field emission electron source (X-FEG) and SuperX EDS together is called ChemiSTEM technology, which makes elemental mapping at atomic level possible.

4.2.3.3 X-ray photoelectron spectroscopy (XPS)

XPS experiments were conducted using PHI VersaProbe II instrument equipped with monochromatic Al K(alpha) source. Instrument base pressure was ca. 4/8 x 10^{-10} Torr. The X-ray power of 25 W at 15 kV was used for all experiments with 100 micron beam size. The instrument work function was calibrated to give a binding energy (BE) of 84.0 eV for Au $4f_{7/2}$

line for metallic gold and the spectrometer dispersion was adjusted to give a BE's of 284.8 eV, 932.7 eV and of 368.3 eV for the C 1s line of adventitious (aliphatic) carbon presented on the non-sputtered samples, Cu $2p_{3/2}$ and Ag $3d_{5/2}$ photoemission lines respectively. The FWHM for Ag $3d_{5/2}$ line at energy range 372 eV to 365 eV was 0.48 eV. The ultimate VersaProbe II instrumental resolution was determined to be 0.3 eV and 0.15 eV using the Fermi edge of the valence band for metallic silver for XPS and UPS (HeII line) respectively. The PHI dual charge compensation system was used on all samples. The high resolution Pt 4f and S 2p spectra were taken with a minimum of 10 - 60s scans using a 0.1 eV step and 23.5 eV and 46.95 eV pass energy respectively. All XPS spectra were recorded using PHI software SmartSoft –XPS v2.0 and processed using PHI MultiPack v9.0 and/or CasaXPS v.2.3.14. The relative sensitivity factors from MultiPack library were used to determine atomic percentage. Peaks were fitted using GL line shapes a combination of Gaussians and Lorentzians with 30-50% of Lorentzian contents. Shirley background was used for curve-fitting. The multiple spectra were recorded on different sample areas, to quantitatively evaluate reproducibility and avoid artifacts or detect radiation damage.

Two different experimental geometries were used in order to determine Pt/S ratio at the core and surface of the nano particles. The surface sensitivity of XPS is enhanced if analyzer collects the photoelectrons taking off at the grazing angle. We analyzed the samples at 45^{o} emission angle and at 10-15^{o} which corresponds to larger and smaller escaping depth of the excited electrons correspondingly. This approach, originally developed for continuous this films, was applied to nanoparticles in assumption that the spherically (Fig. 4.2) shaped nanoparticles likely assemble into mono/multi layers film on the high quality flat surface of the native surface

of the Si(111) while drop casted from solution. If the nanoparticles exhibit core-shell morphology, as it comes from EXAFS, the XPS angular dependence assignments differ for nanoparticles film from these for conventional thin films. According to TEM data (Fig. 4.2) nanoparticles are of the spherical shape and in case of core-shell structure should give different S/Pt ratios if different XPS geometries are used.

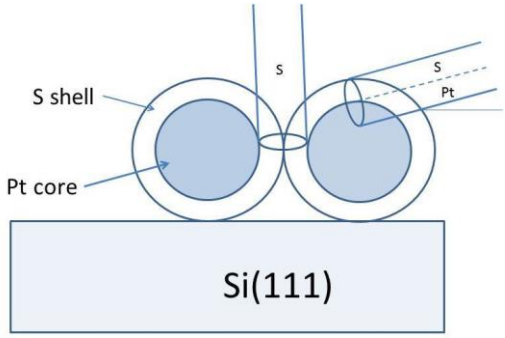

Fig.4.2. At the close to normal take off angles the shell related signal is larger than at the grazing angles.

The measured atomic % concentration ratios for all samples prepared according to that method confirm assumption about layered nature of the nanoparticles assembly for the samples with Pt contents (see Table 4.1).

Table 4.1: Calculated atomic percentage concentrations of Pt and S

At % concentration			
Samples measured, Si(111) substrate	S	Pt	S/Pt
Sample 1 bulk	68.6-69.3	30.7-31-4	2.18-2.25
Sample 1 surface	67.4-67.6	32.4-32.6	2.06-2.08
Sample 2 bulk	68-69.3	30.7-32	2.12-2.25
Sample 2 surface	66.9-67	33-33.1	2.02-2.03
Sample 3 bulk	69.6	30.7	2.29
Sample 3 surface	67.3	32.7	2.05
Sample 4 bulk	70	30	2.33
Sample 4 surface	67	33	2.03

4.2.3.4 UV-Visible spectroscopy (UV-Vis)

Optical absorbance of the Pt(DMSA) nanoparticle colloid samples were recorded using Shimadzu, UV-3600 spectrophotometer in a 10 mm Quartz cuvette (sample volume taken is ~ 3 ml) and the absorbance was measured from 250 nm to 500 nm.

4.2.3.5 X-ray diffraction (XRD)

Empyrean X-ray diffractometer (PANalytical) instrument was used for X-ray diffraction experiments. The samples were ground and placed in an aluminum holder and scanned on a flat sample stage between 5 to 120 degrees at a rate of 0.013 degrees for every 8.67 s. The instrument was set at 45KV and 40mA.

4.2.3.6 Fourier Transform Infrared Spectroscopy (FT-IR)

FTIR samples were prepared by mixing the Pt(DMSA) nanoparticles obtained from the colloidal solution with potassium bromide (KBr) powder and was pressed into pellet form Thermo Nicolet Nexus 670 instrument equipped with two beam splitters (KBr and solid substrate), two detectors (deuterated tri-glycine sulfate detector with KBr window and polyethylene window), and a globar source was used for FT-IR experiments. The Thermo Nicolet Continuum microscope utilized Schwarzchild optics, two objectives (15X and 32X) and one condenser (15X), allowing both reflection and transmission mode data acquisitions. The liquid N_2 cooled mercury cadmium telluride (MCT) microscope detector was utilized to cover the mid-IR spectral range of 11700 – 400 cm^{-1}. The instrument and the beam-collimating-optics section in a plastic container were purged with dry N_2 gas during operation.

4.3 Results and discussion

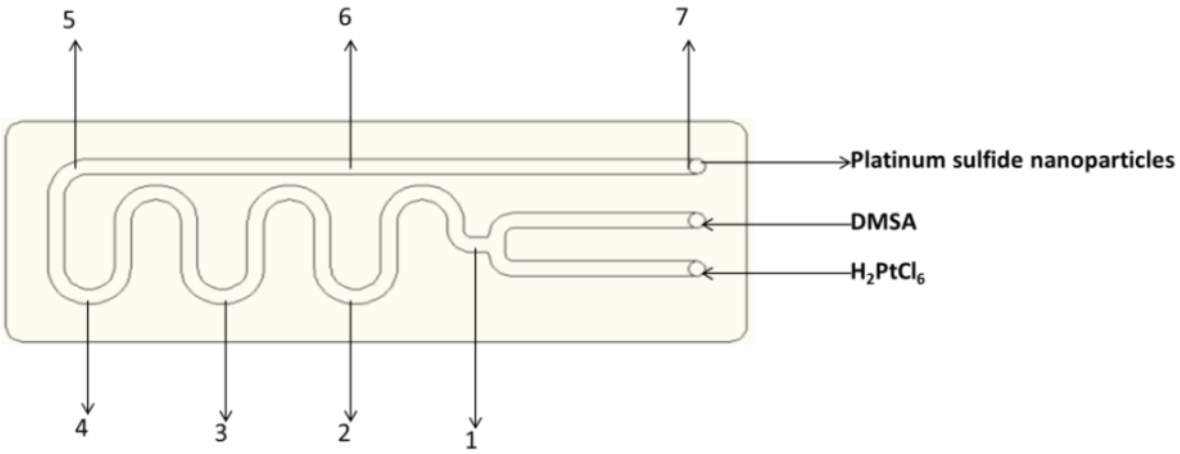

Figure 4.3. Schematic representation of Pt(DMSA) nanoparticles synthesis in a millifluidic reactor chip.

Figure 4.3 illustrates a typical millifluidic reactor chip, that was used in our experiments, possessing a serpentine channel with dimensions of 220 mm X 2 mm X 0.125 mm (Length X Width X Height). The figure also depicts inputs for the precursor reagents (Chloroplatinic acid (H_2PtCl_6) and 2,3-dimercaptosuccinic acid (DMSA)) and different zones (1 – 7) at which the Pt(DMSA) nanoparticles colloid was studied. A more detailed experimental protocol is described in the experimental section. In situ X-ray absorption spectroscopy (XAS) was carried out at these different zones (1 – 7) on the millifluidic reactor (as shown in figure 4.3) in order to accurately determine the features of Pt(DMSA) nanoparticles as well as to deduce their nucleation and growth. The millifluidic reactor was mounted onto a metal stage (that could be adjusted in two dimensions) in the path of the monochromatized synchrotron beam so that the desired zone on the chip could be investigated. In order to determine the local environment around Pt, both aspects of XAS, i.e. X-ray Absorption Near Edge Structure (XANES) and Extended X-ray Absorption Fine Structure (EXAFS), were recorded at the Pt L_3-edge. The reactants were fed continuously into the millifluidic reactor at 0.2 ml/min (H_2PtCl_6 and DMSA as shown in Figure

4.3) ensuring that the reactant and product concentrations at each point along the reactor channel were in laminar regime. The Reynolds number at 0.2 ml/h flow rate was 0.015. The XAS measurements were performed as close to the inlet of the millifluidic reactor as possible (zone 1) as well as at other points (zones 2 to 7) as shown in figure 4.3.

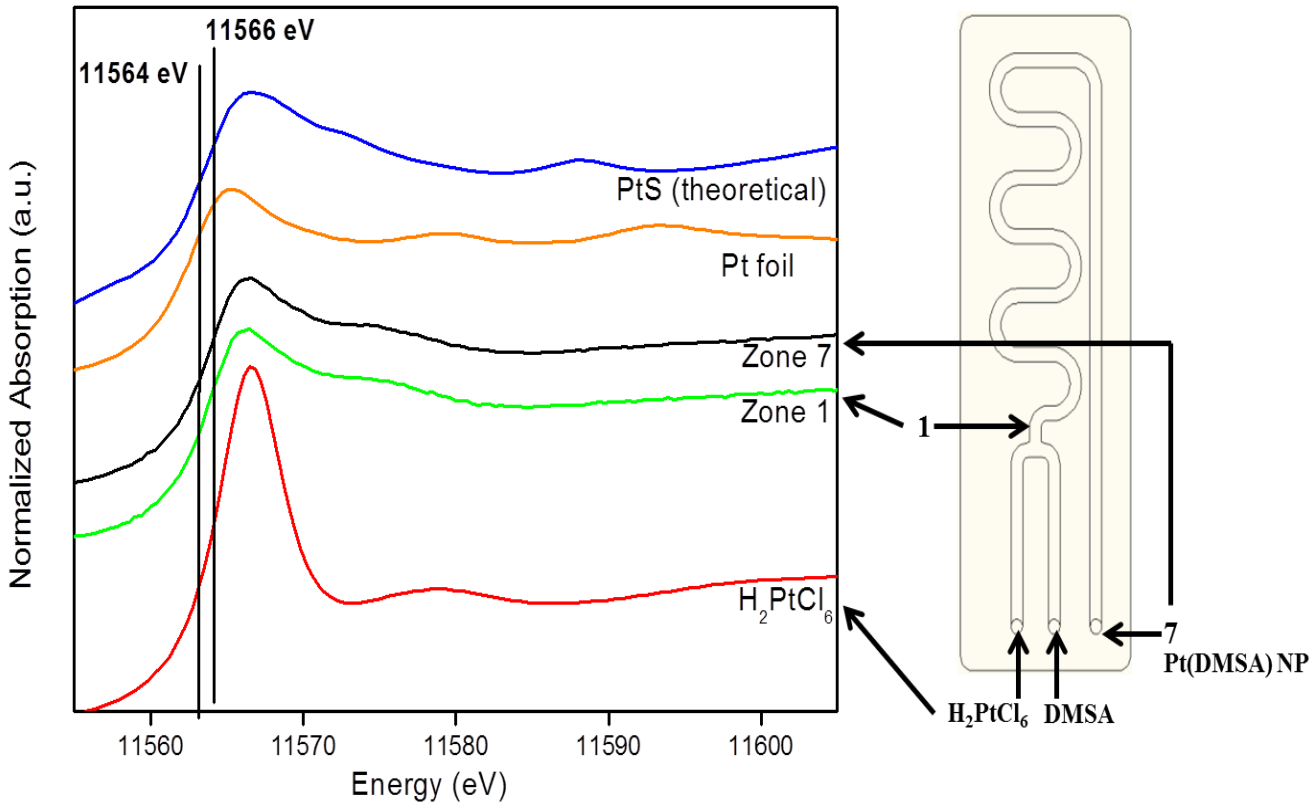

Figure 4.4. Pt L_3-edge XANES spectra: Reference H_2PtCl_6 (red), Experimental spectra of Pt(DMSA) obtained at zones 1 and 7 (green and black, respectively), Standard Pt foil (dark yellow), Theoretically calculated reference PtS (blue)

The experimental Pt L_3-edge XANES spectra (Figure 4.4) for the colloidal solution at zone 1 (green spectrum) of the millifluidic reactor revealed a 1.5 eV white line shift with a shoulder peak at 11575.2 eV when compared with the reference Pt foil (orange spectrum). The spectral results obtained at zone 1 were in good agreement with the theoretical calculated PtS XANES spectrum (blue spectrum) including an oxidation state of +2, therefore indicating the

formation of Pt(DMSA) nanoparticles with Pt-S bonding. The oxidation state of +2 could be determined by comparing the edge energies of Pt foil (+0 at 11564 eV) with the standard H_2PtCl_6 (+2 at 11566.1 eV) and the Pt(DMSA) (+2 at 11565.7 eV) sample. In addition, the less intense white line of the spectrum obtained at zone 1 (green spectrum) indicated a change in geometric structure when compared with the starting H_2PtCl_6 solution (red) due to charge transfer from S to Pt atoms. Such charge transfer was also observed in X-ray photoelectron spectroscopy (XPS) analysis which is discussed later. Since our previous investigation on the synthesis of gold nanostructures gave a conceptual basis for understanding some of the features of the growth of nanoparticles with a time resolution of ~5 ms, (Krishna et.al., 2013) a similar reaction mechanism was anticipated for the present study. Therefore, we probed the millifluidic reactor channels at other zones (2 to 7) in order to have a better understanding of the contribution of the ligand (DMSA) to the synthesis of Pt(DMSA) nanoparticles. However, irrespective of the zones in the millifluidic reactor channel, the XANES spectra collected at all the zones were identical denoting that the formation of Pt(DMSA) as soon as H_2PtCl_6 and DMSA mix at zone 1. We reasoned that a faster reactant flow rate may significantly separate the growth and nucleation of Pt(DMSA) nanoparticles. Subsequently, we increased the reactant's flow rate to 3 ml/min, only to find that the Pt(DMSA) nanoparticles exhibited the same structural and chemical characteristics as before when the resulting colloidal solution was characterized using XAS. This preliminary XAS study pointed out that the reduction of H_2PtCl_6 to Pt(DMSA) nanoparticles was spontaneous in the presence of DMSA, and the effect of different flow rates (0.2 and 3 ml/min) did not have any impact on growth and nucleation of these nanoparticles.

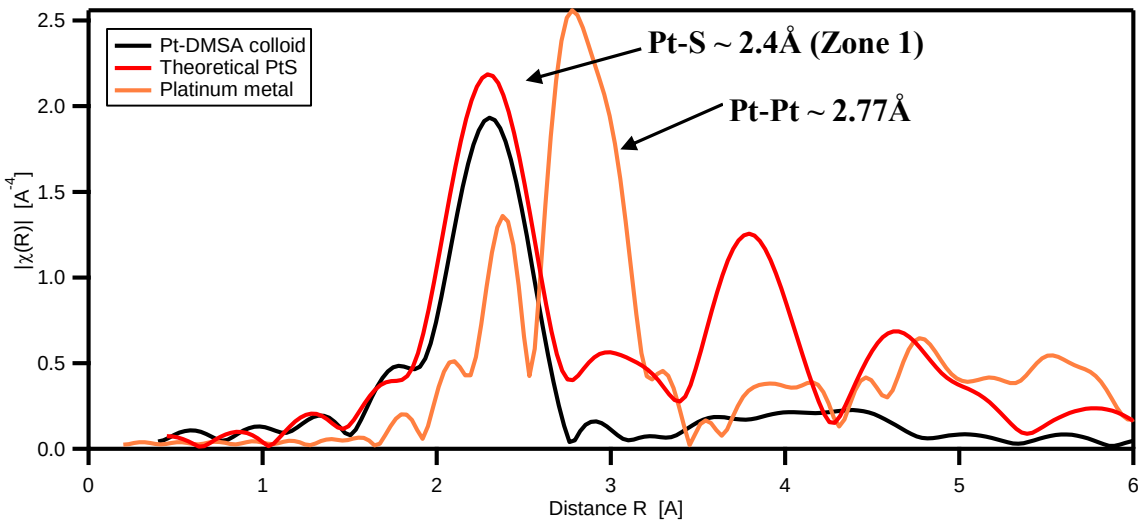

Figure 4.5. Pt L_3-edge FT EXAFS spectra of experimental Pt(DMSA) nanoparticles and theoretical platinum sulfide (PtS) from crystal structure

Table 4.2. Results of the EXAFS Analysis Pt L_3-edge for sample investigated at zone 1

Scattering pair	CN	Ri (Å)	σ^2	$\Delta E0$
Pt-S	3.7	2.31	0.0028	8.50

The Fourier transformed (FT) EXAFS spectrum of the Pt(DMSA) nanoparticles obtained at zone 1 revealed low intense peaks specifically for the higher order coordination shells beyond 2.7 Å when compared with the theoretically calculated PtS crystal structure (Figure 4.5) consistent with small crystallites. In addition, the EXAFS spectra of the Pt(DMSA) nanoparticles obtained at zone 1 were fit using theoretical models in both R-space and k-space in order to extract information on the atomic environment around the central Pt core atom. Detailed information on how these theoretical calculations were performed is described in the methods section. Only the first shell scattering pathway for Pt-S was used to construct the theoretical fitting model for Pt(DMSA) nanoparticles (table 4.2). These results were in good agreement with the EXAFS data presented in figure 4.5.

The Pt(DMSA) nanoparticles colloid was collected at different spatial intervals from the chip during their formation by dissecting it at various zones (1 to 7, as shown in figure 4.3) to study their size dependent optical properties using UV-Vis spectroscopy. The as-collected colloid was immediately quenched in ethanol to arrest the further growth of Pt(DMSA) nanoparticles in order to compare their optical characteristics. The UV-Vis spectra of the Pt(DMSA) nanoparticle colloid collected at all the zones (1 to 7) lacked a characteristic plasmon absorption peak at 260 nm (figure 4.6), which is typically observed for H_2PtCl_6 solution due to ligand-to-metal charge transition of $[PtCl_6]^{2-}$ ions (Li et.al., 2008). This indicated the spontaneous reduction of the H_2PtCl_6 with DMSA at the beginning of the channel, therefore supporting the XANES analysis. In addition, the absence of plasmon peak at 260 nm can be attributed to the formation of Pt(DMSA) nanoparticles with diameter less than about 5 nm; since nanoparticles and atomically precise clusters lose their visible extinction features as they decrease in size (Brege et.al., 2009; Ghosh et.al., 2013; Biswas et.al., 2012; Singh et.al., 2010; Siwach et.al., 2008; Pileni and Lisiecki, 1993; Wei et.al., 2011; Vazquez-Vazquez et.al., 2009; Niranjan and Chakraborty 2012; Brumbaugh et.al., 2014). A separate UV-Vis spectrum was obtained for the unquenched colloidal solution of Pt(DMSA) nanoparticles (zone 7) in order to determine any changes in their optical property. However, comparison of the UV-Vis spectrum of unquenched sample with that of quenched sample showed no difference, indicating a rapid reduction, nucleation, and growth of the Pt(DMSA) nanoparticles as soon as the two reagents mix at zone 1.

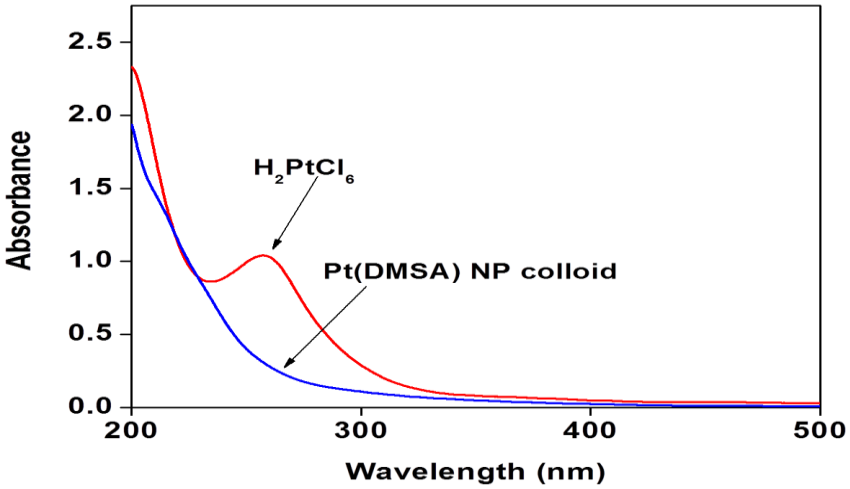

Figure 4.6. UV-Vis spectrum of H_2PtCl_6 (precursor) and Pt(DMSA) nanoparticles colloid indicating the reduction of $[PtCl_6]^{2-}$ ions

HRTEM analyses of the quenched and unquenched colloidal solutions collected from the millifluidic reactor at zone 1 and 7 respectively were carried out to obtain the size of the Pt(DMSA) nanoparticles. HRTEM images (Figures 4.7a & 4.7b) revealed the presence of small spherical Pt(DMSA) nanoparticles with an average diameter of about 5 nm. It is evident from these figures that no significant change in the size was observed for quenched (collected at zone 1) and unquenched (collected at zone 7 and stored for a week) Pt(DMSA) nanoparticles. These comparative HRTEM figures confirmed that the growth of the Pt(DMSA) nanoparticles was instantaneous (< 1s) as soon as the reagents mixed, thereby supporting the XAS and UV-Vis spectral results. The classical nucleation and growth theory points out that slow nucleation leads to formation of nanoparticles with broad size distribution (Lamer and Dinegar, 1950; Kwon and Hyeon, 2011) and vice versa. This theory agrees well with our XAS, UV-Vis and HRTEM analysis, where the nucleation and growth of the Pt(DMSA) nanoparticles were rapid, therefore resulting in small sized nanoparticles. In addition, the HRTEM images showed the presence of reticular planes extending over entire Pt(DMSA) nanoparticles (figure 4.7c) suggesting the

crystalline nature of these particles. The lattice spacing (d) was calculated to be 0.24 nm (figure 4.7(d)), which corresponds to the Pt-S bond distance.

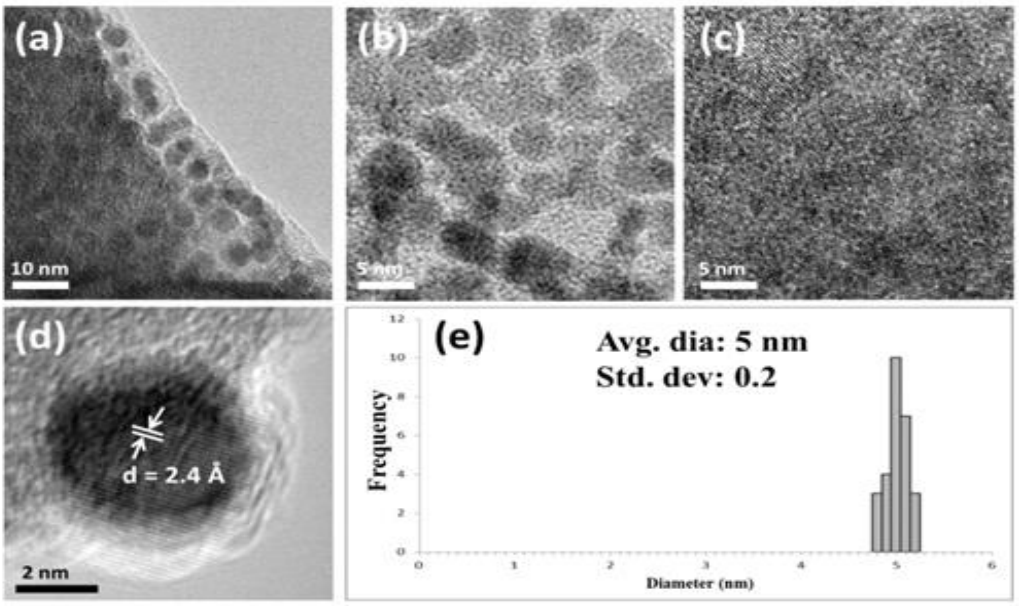

Figure 4.7. a) HRTEM image of the quenched Pt(DMSA) nanoparticles. (b) HRTEM image of the unquenched Pt(DMSA) nanoparticles (c) HRTEM image of Pt(DMSA) nanoparticles with clearly visible lattice fringes passivated by Pt and S atoms, (d) HRTEM image of a single Pt(DMSA) nanoparticle with lattice spacing of 2.4 Å, (e) Corresponding size histogram of Pt(DMSA) nanoparticles

The elemental composition mapping of the Pt(DMSA) nanoparticles using EDS showed equivalent ratio of Pt and S (1:1) in the sample (Figure 4.8a). A combination of STEM imaging equipped with EDS was used to obtain the chemical composition of the nanoparticles and the color-mapped EDS images (Figure 4.8b and 4.8c) indicated the presence of both Pt and S in the Pt(DMSA) nanoparticles. Due to the rapid formation of Pt(DMSA) nanoparticles, there is slight excess of unreacted precursors passivated over the surface of the nanoparticles. This excess distribution of unreacted precursors over the Pt(DMSA) nanoparticles also correlates well with the EDS analysis indicating high Pt to S ratio. The passivation of Pt and S precursor atoms over the Pt(DMSA) nanoparticles can be explained by the Watzky and Finke model, which describes

a faster growth rate of the nanoparticles dominating at some point during the reaction, therefore effectively stopping the nucleation of new particles (Watzky and Finke, 1997; Watzky and Finke, 1997). This model agreed well with our UV-Vis and HRTEM analysis as the presence of 5 nm sized Pt(DMSA) nanoparticles at zone 1 indicated a faster growth rate, which successively stopped the nucleation of newer particles, therefore, resulting in unreacted Pt and S precursor atoms. Furthermore, XRD analysis of these samples revealed two peaks centered at $2\theta = 34$ and 54 similar to standard Pt(DMSA) XRD spectrum (Figure 4.8d). These peaks were broad due to the ultra-small size of the crystalline Pt(DMSA) nanoparticles. The small size of Pt(DMSA) nanoparticles is attributed to the high ratio of DMSA to H_2PtCl_6, which in turn contributed to the increased ligand coverage on the nanoparticles surface thereby limiting their further growth. In addition, the broad peaks in the XRD also infers amorphous component in the nanoparticles due to the presence of unreacted Pt and S precursor atoms.

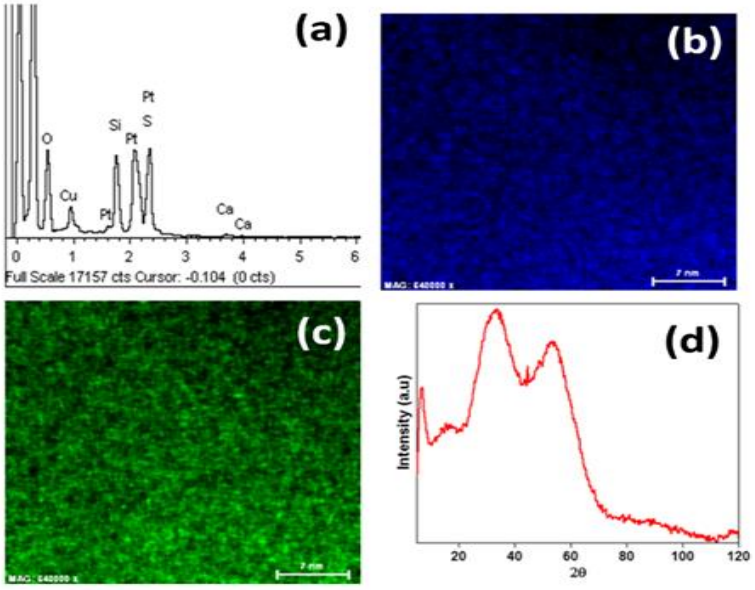

Figure 4.8. (a) EDS spectra of the nanoparticles formed after reduction with DMSA showing the presence of both Pt and S; (b) and (c): STEM-EDS images of Pt (left) and S (right) confirming the passivation of Pt and S atoms throughout the sample. The white areas in both images represent the unreacted Pt and S precursor atoms passivated over the crystalline Pt(DMSA) nanoparticles respectively; (d) XRD spectra of the purified Pt(DMSA) nanoparticles.

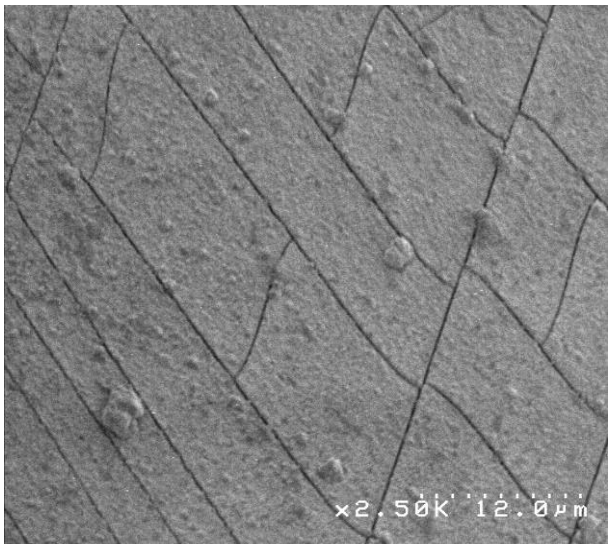

Figure 4.9. SEM image of the Pt(DMSA) microstructures formed within the walls of the millifluidic rector chip after 9 h reaction.

The growth of Pt(DMSA) nanostructures over time on the walls of the millifluidic reactor was also studied (by feeding the precursors (H_2PtCl_6 and DMSA) at 1 ml/h) as our previous report on gold (Krishna et.al., 2013) showed the formation of different morphology and dimensional controlled nanostructures with time over a period of 9 h. In the present investigation, the low magnification SEM image at zone 1 of the millifluidic reactor channel (Figure 4.9) showed randomly sized polygonal Pt(DMSA) microstructures formed over a thin Pt(DMSA) film after 9 h. Although the growth of PtS nanocrystals on GaAs at 500^o C was reported earlier (Malik et.al., 2002), the formation of such Pt(DMSA) nanostructures at ambient conditions, in an aqueous medium, and under flow conditions has not been reported. Also, this is the first report of their formation within a continuous flow reactor. Furthermore, the chip was dissected at zone 1 to analyze the Pt(DMSA) structures coated on its wall using XAS. The XAS spectrum obtained for the sample coated on the millifluidic reactor wall at zone 1 resembled the spectra obtained from all other in-situ XAS experiments.

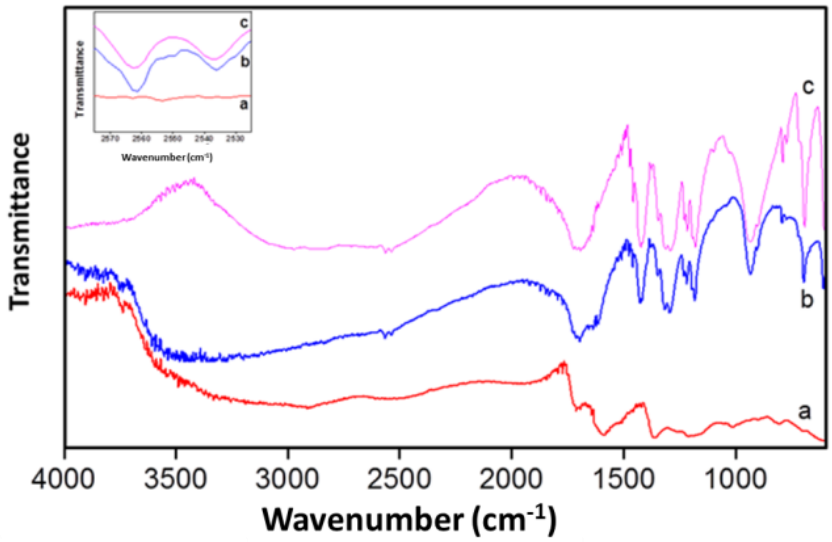

Figure 4.10. (a) FTIR spectra of Pt(DMSA) colloidal nanoparticles, b) H_2PtCl_6 and DMSA powder mixture, c) DMSA. Inset shows the expanded version of the –SH– stretching in H2PtCl6-DMSA mixture (blue) and DMSA (pink). The absence of this stretching in spectrum (a) confirms Pt-S bond formation.

For better understanding of the bonding between Pt and S in Pt(DMSA) nanoparticles, a systematic study on the interaction between DMSA and H_2PtCl_6 precursors was carried out using FTIR spectroscopy. A detailed preparation process of Pt(DMSA) nanoparticles samples for FTIR is described in the experimental section. The characteristic peak of the –SH– group in DMSA at 2563 and 2537 cm^{-1} (shown in the figure 4.10c) was identified in order to confirm the bond formation between Pt and S atoms in the Pt(DMSA) nanoparticles. Comparison between the FTIR spectra of Pt(DMSA) nanoparticles and DMSA showed an absence of the thiol (–SH–) stretch for Pt(DMSA) nanoparticles (figure 4.10a), which indicated the formation of Pt-S bond. The broad absorption band observed between 3400 and 2400 cm^{-1} could be attributed to the carboxylic acids and is due to the unreacted DMSA (HOOC-CHSH-CHSH-COOH) ligand passivated over the Pt(DMSA) nanoparticles. The intra-molecular hydrogen bonding within the –COOH– group results in a broad absorption band in the FTIR spectrum. The inter-molecular

hydrogen bonding between carboxylic acid groups is another possible cause for excess DMSA being adsorbed onto the Pt(DMSA) nanoparticles.

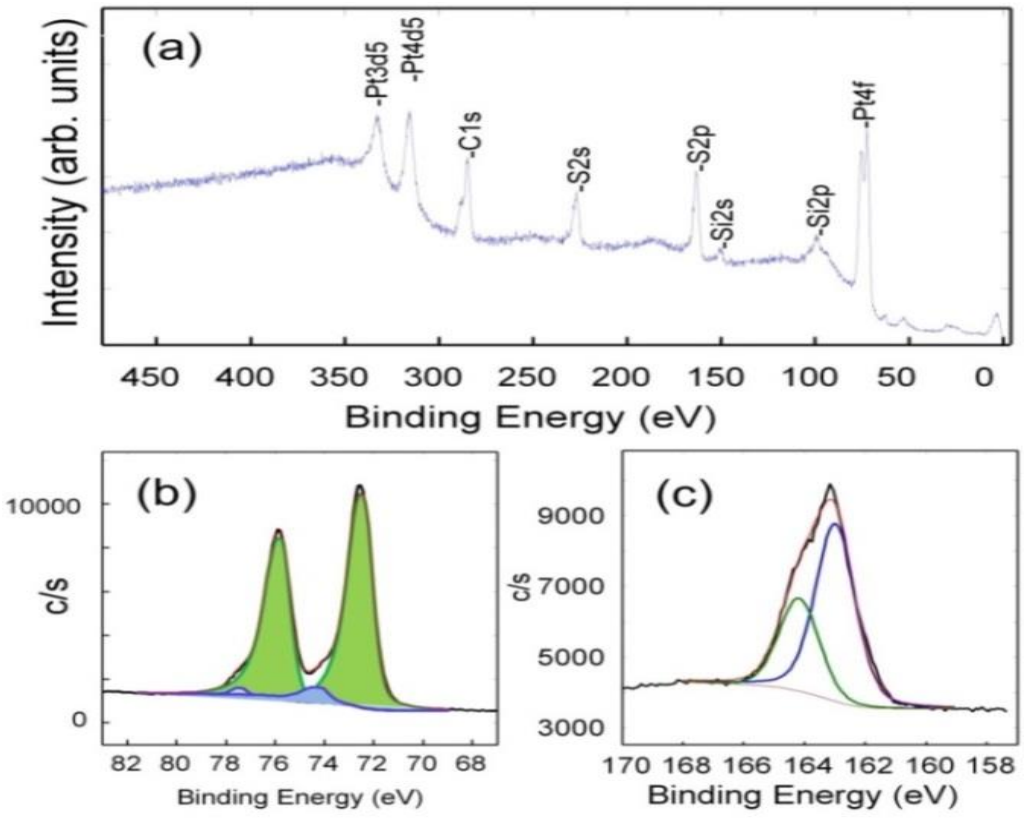

Figure 4.11. (a) Survey XPS scan of the Pt(DMSA) nanoparticles drop casted onto native SiO_2 surface of the Si(111) wafer. (b) High resolution Pf 4f XRS spectra, black line represents experimental data, red line – generated fit curve, green – Pt^{2+} 4f doublet, blue – Pt^{4+} oxide doublet. (c) High resolution S 2p XPS spectra, blue line $2p_{3/2}$ component, green line – $2p_{1/2}$ component.

XPS measurements on Pt(DMSA) nanoparticles were carried out in order to determine the bonding in Pt(DMSA) nanoparticles and oxidation state of Pt after the formation of the nanoparticles (Figure 4.11). XPS spectra show two peaks at 72.41 and 75.77 eV related to the binding energies of 4f7/2 and 4f5/2 electrons of Pt (Figure 4.11b) and two peaks at 162.97 eV and 164.17 eV related to the binding energies of $2p_{3/2}$ and $2p_{3/2}$ electrons of sulfur (figure 4.11c). The peak fitting parameters for Pt 4f and sulfur 2p regions are given in table 4.3 and 4.4

respectively. More than 94% of the sample contained Pt at the intermediate binding energy, which suggested +2 oxidation state by taking the calculated atomic percentage concentrations into account (Table 4.1). There was presence of excess of sulfur, possibly related to unreacted precursor sulfur atoms that had passivated over the Pt(DMSA) nanoparticles during the synthesis. These findings along with positive binding energy shift for Pt 4f indicate a charge transfer from Pt to S atoms, which is in good agreement with XAS results.

Table 4.3. Peaks fitting parameters for Pt 4f region

Spec	Band	Pos, eV	PosSep, eV	FWHM, eV	Height	% Gauss	Area	% Area
1	1	72.41	0.00	1.22	9704	54	14863	53.92
	2	74.16	1.75	1.46	680	41	1277	4.63
	3	75.77	3.36	1.24	7326	75	11147	40.44
	4	77.36	4.95	0.74	312	80	276	1.00

Table 4.4. Peaks fitting parameters for sulfur 2p region

Spec	Band	Pos, eV	PosSep, eV	FWHM, eV	Height	% Gauss	Area	% Area
1	1	162.97	0.00	1.55	5022	71	9403	66.67
	2	164.17	1.20	1.55	2690	87	4701	33.33

4.4 Conclusions

In conclusion, a viable aqueous based continuous synthesis of Pt(DMSA) nanoparticles at ambient conditions using a millifluidic reactor is demonstrated. The Pt(DMSA) nanoparticles formed have an average diameter of 5 nm. The fast nucleation and formation of the Pt(DMSA) nanoparticles was confirmed with the help of in situ XANES, which revealed spontaneous Pt-S bond formation at zone 1 of the millifluidic reactor channel. Furthermore, the XANES spectra obtained at all the zones (1-7) were observed to be similar indicating that the reaction completed as soon as the reactants mixed at zone 1. The results presented here prove the possibility to synthesize and characterize Pt(DMSA) nanoparticles through a continuous flow process at room

temperature using millifluidic chip reactor. Unlike the case of the ability to time-resolved probing of nucleation and growth of Au(DMSA) nanoparticles (Krishna et.al., 2013), present investigations show that ultra-fast formation and growth of Pt(DMSA) nanoparticles prevents not only their time–resolved probing but also prevent coating of the channel wall.

CHAPTER 5: MILLIFLUIDICS FOR TIME-RESOLVED CONTINUOUS FLOW OXIDATION OF 5-(HYDROXYMETHYL)FURFURAL TO 2, 5-FURANDICARBOXYLIC ACID AT AMBIENT CONDITIONS

5.1 Introduction:

Due to increase in demand for energy, powerful scientific tools with a combination of computational, synthesis and characterization techniques are being developed to design and create novel materials for green energy applications such as fuel cells, biomimetics and catalysis (Spivey et.al., 2014). These tools are helping in creating high quality materials with atomic precision involving lesser quantity of reagents. In this regard, Lab-on-a-chip (LOC) based millifluidic reactors have started to gain attention due to easy and inexpensive fabrication techniques as well as for its inherent capability to carry out chemical reactions at isotropic conditions in continuous flow conditions (Kalinin et.al., 2012). In addition, they offer the possibility to acquire real time in-situ experimental data at various spatial intervals with the ability to convert spatial resolution into time resolution due to higher signal to noise ratio (Krishna et.al., 2013). Information obtained using such time resolved in-situ measurements provide insight into the reaction kinetics for reactions that are extremely fast. Our group has previously successfully demonstrated the utility of such millifluidic chip for an in-situ real time analysis of growth of copper nanoclusters and gold nanoparticles using synchrotron radiation based X-ray Absorption Spectroscopy (XAS) (Krishna et.al., 2013; Biswas et.al., 2012; Krishna et.al., 2013). These materials were found to be catalytic as well, therefore providing potential opportunities for time-resolved monitoring of catalytic reactions. Considering these advantages, here we demonstrate the use of a millifluidic system to showcase its capability to investigate time-resolved continuous flow catalysis of a biomass conversion reaction. It is crucial to understand the potential in developing biomass derived products in a chemical industry,

especially when there is a need to reduce waste and increase sustainability during production. However, it has been a challenging task to control a biomass conversion process because a slight change in the reaction parameters could lead to decreased selectivity towards the desired product (Cheng and Huber, 2011). In this regard, the use of continuous flow reactors has several advantages over batch reactors, with respect to controlling the reaction parameters such as temperature, pressure, residence time, and mixing (Hartman and Jensen, 2009). In addition, these reactors enable isolation of intermediate products, thereby, assisting in chemoselectivity. While a variety of chemical reactions catalyzed by embedded or impregnated catalysts using continuous flow reactors have been reported previously, only few of them are related to biomass conversion (Navin et.al., 2013). The synthesis of fine chemicals obtained through the cellulosic and lignocellulosic biomass degradation is a most widely envisioned approach toward the implementation of renewable feed stocks for fuels and chemicals (Huber et.al., 2006). Therefore, for this purpose, we chose to investigate the oxidation of HMF to FDCA as a model reaction for biomass conversion, since FDCA is an important renewable alternative for terephthalic acid (PTA) in the production of polyesters (Gorbanev et.al., 2009; Lilga et.al., 2010). HMF has also been identified by US DOE as one of the important intermediates for biorenewable chemicals and fuels (Bozell and Petersen, 2010).

Significant advances have been made in the synthesis of furan-based polyester building block FDCA from biomass derived HMF by using homogeneous and nanoparticulate catalysts (Saha et.al., 2012). A detailed analysis on existing reports show that the oxidation of HMF has been carried out with various catalysts such as Au, Pt, Pb, Pd, vanadyl-pyridine complexes, and metal bromides using batch reactors; although this process has been recently scaled up to bench

scale conditions (Gorbanev et.al., 2009, Davis et.al.,2011; Davis et.al., 2012; Partenheimer and Grushin, 2011; Navarro et.al., 2009; Siyo et.al., 2014). In most cases, Au-based catalysts have been used for this reaction since they have been demonstrated to be highly efficient in terms of activity and selectivity. In the majority of these experiments, the gold catalysts have been supported on materials such as TiO_2, CeO_2, C, FeO_2 etc. Experiments that were carried out using such supported gold catalysts (Pasini et.al., 2011) (Au/TiO_2, Au/CeO_2, Au/C, Au/FeO_2) showed positive results with 99% FDCA yield at high temperatures (60 to 100^oC). Nevertheless, there are currently other challenges such as pressure and corrosive reaction conditions involved with catalytic oxidation of HMF to FDCA. It should be noted here that the metal catalysts used in these reactions were subjected to deactivation due to high temperatures used and over-oxidation of their surface. All of the existing literature indicate that either high temperature or high pressure or both have to be maintained at all times in order to have an efficient conversion of HMF to FDCA (Casanova et.al., 2009; Koopman et.al., 2010; Gupta et.al., 2011; Albonetti et.al., 2012; Cai et.al., 2013; Jain et.al., 2015). Additionally, the reactors were pressurized with oxygen in order to achieve the oxidation in most cases. Taking these challenges into consideration, for the first time we have developed a method for convenient ambient temperature and pressure based continuous flow oxidation of HMF to FDCA using an aqueous phase oxidizing agent in a millifluidic reactor embedded with nanostructured gold catalyst. The conversion of HMF to primary and secondary products was characterized at various spatial intervals in the millifluidic reactor to understand reaction mechanisms. This is an advanced concept in the development of continuous flow nanostructured catalyst reactors where multiple value-added products from a range of renewable feed stocks can be produced. This work showcases the importance in the integration of green chemistry and green engineering into continuous flow catalysis, along with

the use of low environmental impact technologies such as millifluidic reactors for sustainable societies.

5.2 Materials and Methods

5.2.1 Experimental section

5.2.2.1 Chemicals

Chloroplatinic acid hexahydrate ($H_2PtCl_6.6H_2O$, 99.9%, Strem chemicals), meso-2,3-dimercaptosuccinic acid (DMSA, 97%, Alfa Aesar), Sodium hydroxide (NaOH, 98.6%, Macron chemicals), sodium borohydride ($NaBH_4$, 98%, Aldrich), Ethanol (EtOH, 200 proof), 5-(Hydroxymethyl)furfural (HMF, Aldrich), 5-Hydroxymethyl-2-furancarboxylic acid (HMFCA, Aldrich), 2, 5-Furandicarboxylic acid (FDCA, Aldrich), and tert-Butyl hydroperoxide solution (70% in water, Luperox® TBH70X, Aldrich) were purchased. All chemicals were used as received without further purification. Nanopure water was used for all the experiments.

5.2.2.2 Millifluidic platform set-up

The millifluidic reactor chips made of polyester terephthalate (PET) were purchased from Millifluidica LLC. The channel dimensions of the chip were 2 mm wide, 0.125 mm in depth and 220 mm in length. The millifluidic device was tested with water as solvent at different flow rates prior to the experiment to optimize the required flow rate.

5.2.2.3 Catalysis experiments

In a typical reaction, HMF (3 mM), NaOH (12 mM) and 70% TBHP in H_2O (10x diluted) was used.

5.2.2.4 Gold catalyst

The synthesis Au nanoparticles for batch reactions and coating of Au structures within the millifluidic reactor channel for continuous flow reactions were carried out according to the procedure described by Krishna et.al. 2013.

5.2.2.5 Continuous flow oxidation of HMF using millifluidic reactor

5 ml of 3 mM HMF was mixed with 5 mL of 12 mM NaOH in a vial. To this mixture, 5 mL of 10x diluted 70% TBHP in H_2O was added and vortexed for 10 seconds. This reaction mixture was transferred to a syringe and injected into the millifluidic reactor chip coated with nanostructured gold at 0.1 mL/h using a pulsation free pump at room temperature and pressure. Reaction samples were collected at different spatial intervals as the reaction mixture moved within the millifluidic reactor channel as shown in Figure 5.1. These samples were analyzed using UV-Vis spectrophotometer and HPLC without further processing.

5.2.2.6 Batch mode oxidation of HMF

5 mL of 3 mM HMF solution was mixed with 5 mL of 12 mM NaOH solution in a conical flask. To this mixture 5 mL of 10x diluted 70% TBHP in H_2O was added along with 5 mg of Au nanoparticles. The vial was closed and the reaction solutions were mixed using a magnetic stirrer at room temperature and pressure. Samples were taken as the reaction progressed and centrifuged to remove any Au nanoparticles that might have transferred during the sample collection. The centrifuged samples were analyzed using UV-Vis spectrophotometer and HPLC without further processing.

5.2.2.7 UV-Visible spectroscopy (UV-Vis)

Optical absorbance of the HMF reaction samples were recorded using Shimadzu, UV-3600 spectrophotometer in a 10 mm Quartz cuvette (sample volume taken is ~ 3 mL) and the absorbance was measured from 200 nm to 500 nm.

5.2.2.8 High Pressure Liquid Chromatography

HPLC analysis was performed with a Waters 616 pump, Waters 2707 Autosampler, and 996 Photodiode Assay Detector, which are controlled by Waters Empower 2 software. The separation was performed on an Agilent Zorbax 300Extend- C18 column (5 um, 4.6× 150 mm) with guard column (3.2 × 10 mm) by a gradient resulting from mixing eluents A (0.1% TFA in water) and B (0.1% TFA in acetonitrile). The flow rate was 1.0 mL/min.

5.3 Results and Discussion

5.3.1 HMF oxidation using continuous flow millifluidic reactor

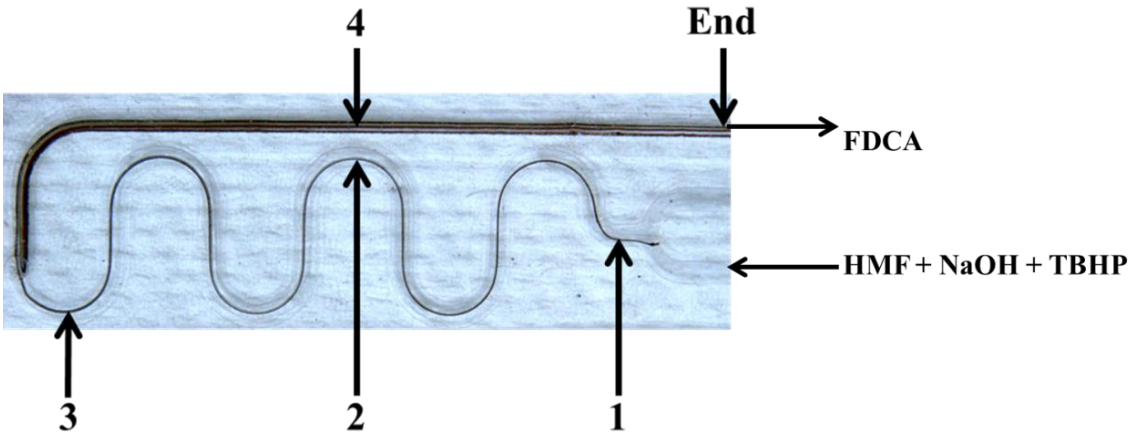

Figure 5.1: Schematic representation of oxidation of HMF to FDCA using a millifluidic reactor chip coated with nanostructured gold catalyst.

The oxidation of HMF was carried out within a millifluidic reactor channel of dimensions 220 mm X 2 mm X 0.125 mm (Length X Width X Height) coated with nanostructured gold catalyst. The coating of gold nanostructures within the millifluidic reactor channel was carried out according to the previously reported protocol by Krishna et.al (Krishna et.al., 2013). An aqueous mixture of HMF, NaOH and TBHP were pumped into the millifluidic reactor channel at 0.1 ml/h at ambient temperature and pressure as depicted in Figure 5.1. A more detailed experimental protocol for the reagents preparation and the concentrations used is described in the methods section.

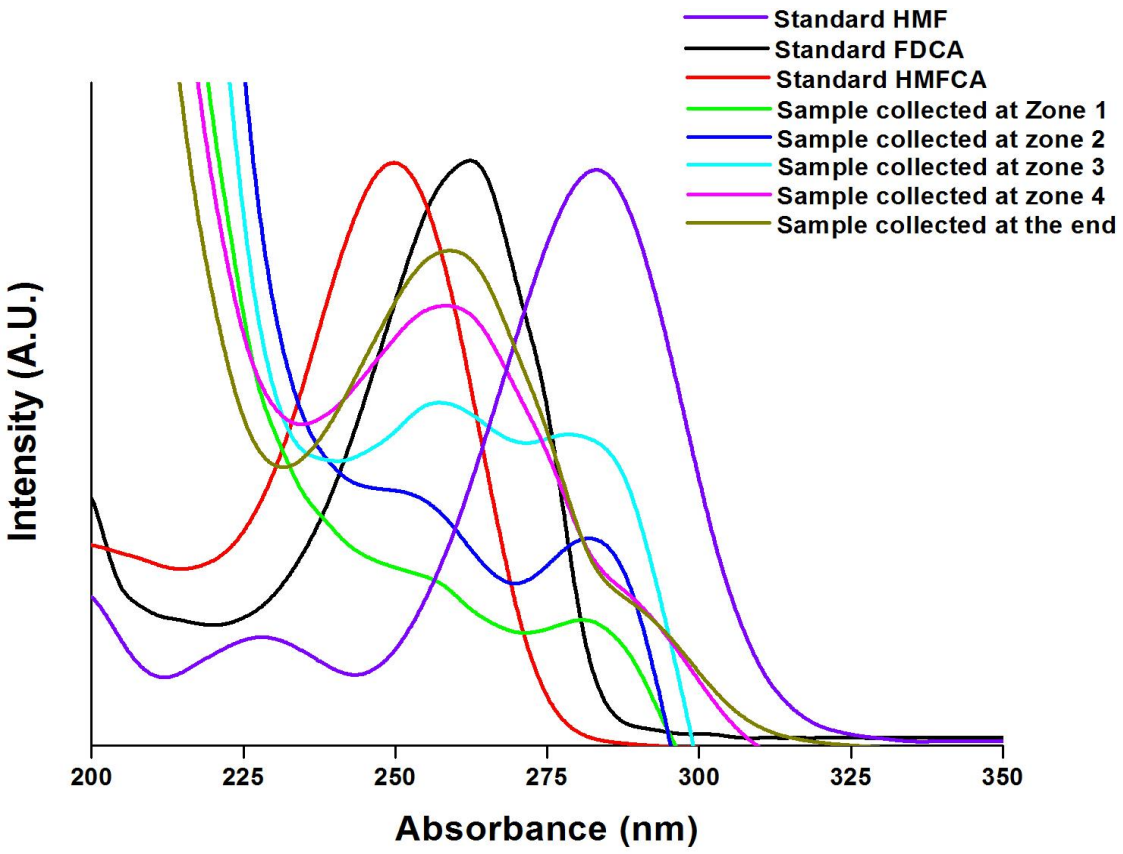

Figure 5.2: UV-Vis spectra of the reaction mixtures collected at different zones of the millifluidic reactor channel by dissecting the chip.

In order to monitor in-situ formation of HMF oxidation products, several initial studies using in-situ UV-Vis spectroscopy technique were carried out to obtain the mechanistic information on the HMF oxidation process within the millifluidic reactor. However, due to the dilute concentration of the reagents, their absorbance was masked due to a strong UV absorbance of the polymeric material (Polyester terephthalate, PET) of the millifluidic reactor thereby making it difficult to collect in-situ UV-Vis absorption data. However, the option to dissect the PET-based millifluidic reactors (Li et.al., 2012) at desired locations made it more feasible to proceed further and carry out HMF oxidation study and obtain mechanistic information at different spatial and time intervals. It should be noted here that this approach makes the millifluidic systems to have an upper hand amongst other traditional microfluidic devices (Krishna et.al., 2013). Hence, UV-Vis analyses were carried out by collecting aliquots of reacted solutions by dissecting the millifluidic reactor channel at various spatial intervals (zones 1 to 4, as shown in Figure 5.1) in order to examine the kinetic evolution of the products due to oxidation of HMF over the nanostructured gold. The UV-Vis absorption spectra (Figure 5.2) of the reaction mixtures collected at different zones of the millifluidic reactor channel revealed a sequential conversion of HMF to FDCA, where the concentration of the reactant (HMF) decreased with increase in the concentration of the product (FDCA), as the reactant moved towards the end of the nanostructured gold-coated millifluidic channel. However, differences were noticed in terms of final product selectivity (FDCA) since the product peak at 258 nm for the samples collected at all the zones resulted in a 4 nm shift in the absorbance peak when compared with the absorbance peak of standard FDCA (black spectrum in Figure 5.2). These results strongly suggested the presence of other products that might have formed during the oxidation of HMF. Therefore, subsequent to the UV-Vis spectroscopy, the products were

analyzed by high-performance liquid chromatography (HPLC) in order to characterize the by-products formed during the oxidation of HMF. All the conclusions derived from UV-Vis spectroscopy were supported by HPLC analysis.

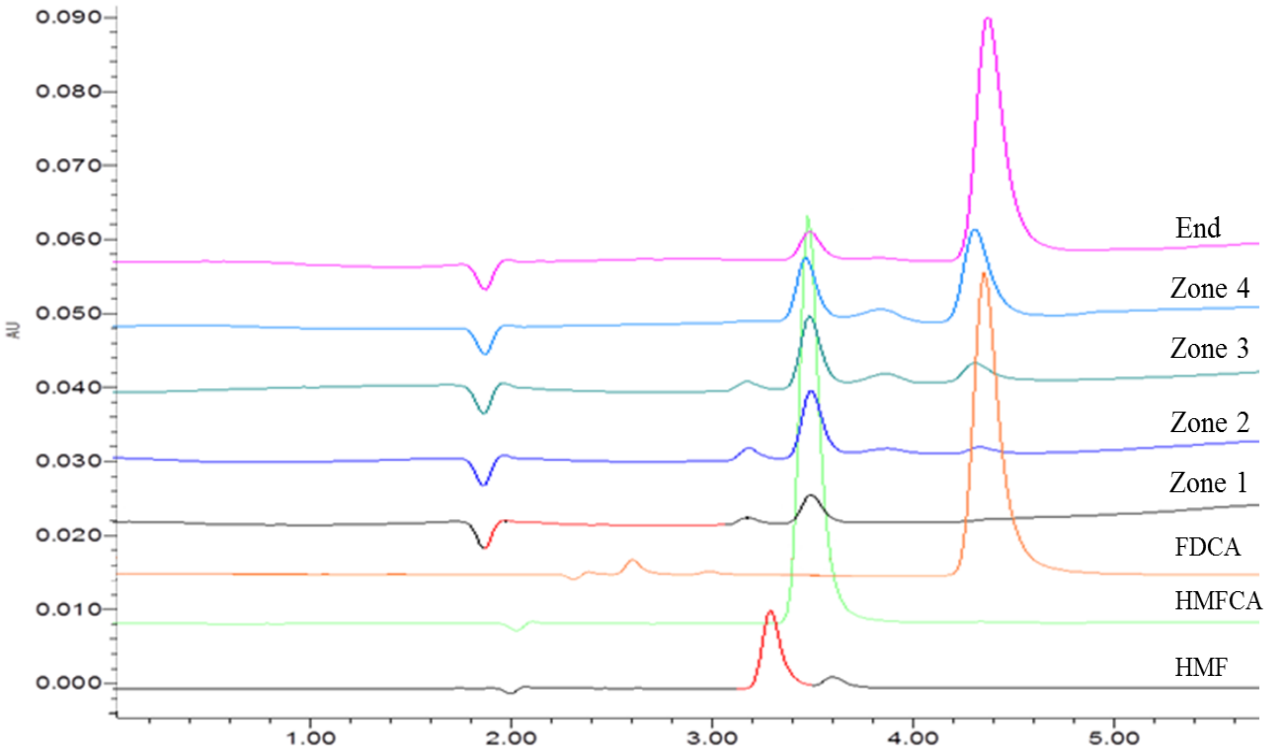

Figure 5.3: HPLC of the reaction mixtures collected at different zones of the millifluidic reactor channel.

As shown in Figure 5.3, HPLC of the samples of the HMF oxidation reaction revealed a mixture of products after 20 minutes (Table 5.1, exp 3). The peak detected at zone 1 (Table 5.1, exp 2) indicated the formation of the primary product 5-hydroxy-2-furancarboxylic acid (HMFCA), where only the aldehyde group of HMF was oxidized. During this time, no formation of secondary product (FDCA) or conversion of primary product (HMFCA) was detected.

Interestingly, maximum peak intensity of the primary product was detected at zone 2, before setting into steady absorption at zone 3. Simultaneously a second peak was observed to originate at zone 2 which had an increased intensity in subsequent zones (3 and 4) indicating the formation of a secondary product, FDCA. At zone 3, a continuous low, steady concentration of HMFCA was detected demonstrating its importance as an intermediate for the formation of the secondary product, FDCA. This intermediate was further converted to FDCA due to oxidation of the primary alcohol group in HMF as shown in Figure 5.4. The consumption of the intermediate compound (i.e. HMFCA) to FDCA was a much slower step when compared to the first step, i.e. oxidation of HMF to HMFCA. In addition, a gradual decrease in the primary reactant peak intensity was seen at zones 2, 3 and 4 suggesting the partial catalytic transformation of the reactant (HMF) into the intermediate product (HMFCA). This analysis excluded the second reaction pathway of HMF (Navarro et.al., 2009) that was described in Figure 5.5, in which it was proposed that the interaction between the reactants can also lead to the formation of DFF. Therefore, it can be concluded that the consumption of HMF was followed by the formation of intermediate product, HMFCA, which further reacted with the nanostructured gold catalyst to form the secondary product, FDCA.

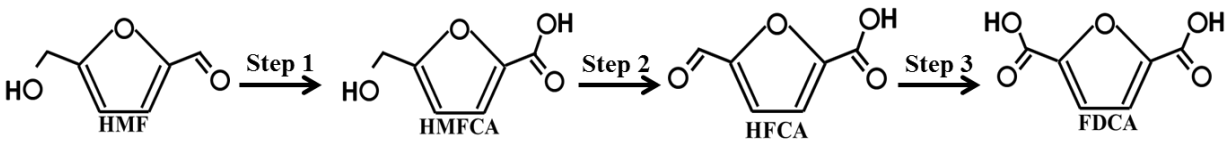

Figure 5.4: HMF Oxidation pathway leading to FDCA with HMFCA as the intermediate product

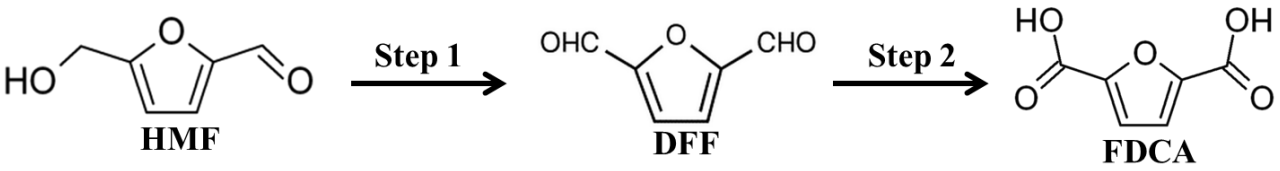

Figure 5.5: HMF Oxidation pathway leading to FDCA with DFF as the intermediate product

The percentage of the reaction products detected is listed in Table 5.1. The quantification calculations were performed by integrating the area of the HPLC peaks of the reaction solutions as a function of time along the millifluidic reactor channel. The area of the HPLC peaks were converted to concentration values (mmol) in order to determine the percentage of the reaction molecules. The concentration values and the peak areas are listed in the appendix. It is clear from Table 5.1 that the percentage of HMFCA was found to increase gradually at the initial zones (i.e. zones 1, 2 and 3) of the millifluidic reactor thereby demonstrating its pivotal role as an intermediate for the formation of secondary product, FDCA. These results excluded the competitive reaction between the aldehyde and alcohol groups associated with the HMF furan ring and making it very clear that FDCA (zones 3, 4 and 5) cannot be obtained in an aqueous medium without the evolution of the primary product, HMFCA.

Table 5.1: Percentage of HMF converted and HMFCA and FDCA detected at different zones of the millifluidic reactor channel

Exp. No.	Time (min)	Zone	HMF conversion (%)	HMFCA detected (%)	FDCA detected (%)
1	0	0	0	0	0
2	10	1	88.36	86.53	0
3	20	2	88.16	88.45	3.37
4	30	3	87.83	87.12	13.14
5	40	4	~99	84.57	15.43
6	50	5	~99	62.71	37.29

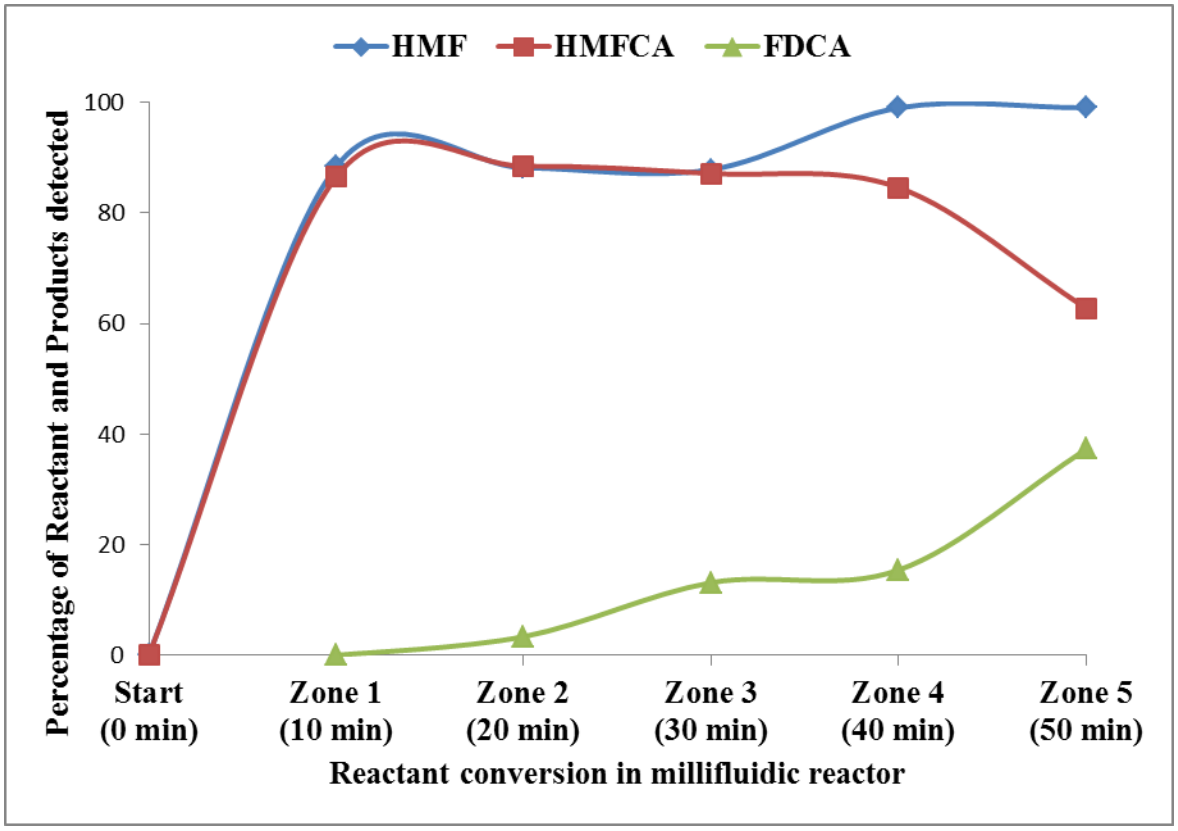

Figure 5.6: Oxidation of HMF to FDCA using a millifluidic reactor chip coated with nanostructured gold catalyst.

As analyzed by UV-Vis spectroscopy and HPLC, it can be stated that the chemoselectivity of the reaction products can be modified by tuning the residence time of the reactants within the millifluidic reactor channel i.e. a fast volumetric flow rate or short residence time of the reaction solution could result in less HMF oxidation with a significant reduction in the intermediate (HMFCA) and final (FDCA) product yield. Whereas, a similar approach to tune the selectivity of different products in similar cascade reactions is not easy to achieve while using homogeneous or heterogeneous catalysts in a batch reactor. Furthermore, the results obtained here highlight that the nanostructured gold catalyst is highly active as suggested by our previous reports (Krishna et.al., 2013). A separate experiment was carried out with HMFCA as

the initial reactant using the millifluidic reactor chip coated with Au structures. The reaction solution was collected at the outlet of the millifluidic reactor chip and was analyzed using HPLC, which revealed 54.36% of the final product (FDCA) detection. In addition, these results demonstrate the applicability of the millifluidic reactors for fundamental understanding of the catalytic reactions mechanism, where isolation of intermediate and final products can be achieved without much difficulty.

5.3.2 HMF oxidation using batch reactor

The oxidation of HMF was also conducted in a batch process at ambient temperature and pressure in order to compare the amount of FDCA with the continuous flow millifluidic reactor conditions. The batch reaction experiments were carried out in a conical flask for 24 h and aliquots from the reaction were collected periodically for HPLC analysis. Table 5.2 shows the quantification data of FDCA under batch reaction conditions calculated by integrating the area of the peaks obtained for HPLC of the reaction aliquots as a function of time. The concentration values and the HPLC peak areas are listed in the appendix. Employing a batch reactor for HMF oxidation resulted in a major difference in the obtained percentage of intermediate (HMFCA) and final product (FDCA). The batch reactor results revealed a 100% HMF conversion within the first 2 h of the reaction with HMFCA as the major product being formed after 60 min (Table 5.2, exp. 2) and its concentration was found to be relatively unchanged even up to 6 h. In addition to HMFCA, a lower concentration of FDCA was also observed in the reactant mixture after 60 min (Table 5.2, exp. 2). The concentration of HMFCA and FDCA suggested the competition between the aldehyde and the alcohol moiety associated with the HMF furan ring during oxidation. However, according to the results obtained from the continuous flow oxidation

using millifluidic reactor, it can be clearly postulated that the oxidation initially took place at the aldehyde moiety and not at alcohol moiety. It was not surprising that the radical nature of TBHP-based oxidation first oxidized the aldehyde moiety associated with HMF, since aldehyde groups are more prone to oxidation than the alcohol groups. The concentration of HMFCA after 60 minutes did not increase significantly and it appeared that the HMFCA concentration has reached saturation thereby diverting the further oxidation towards the alcohol moiety of HMF resulting in traces of FDCA. The selectivity of HMFCA was nearly constant at all-time intervals (Table 5.2, expts. 2 to 5), which indicated that the reaction pathway was not affected as shown in Figure 5.4. From these results, it can be understood that the presence of aldehyde moiety decreased the rate of oxidation of the primary alcohol group associated with HMF in aqueous medium, therefore reducing the rate of FDCA production. It should be noted that the oxidation of HMFCA to FDCA proceeded with the formation of another intermediate, Hydroxyfurancarboxylic acid (HFCA, step 2 in figure 5.4). The presence of HFCA could not be detected in our experiments due to its rapid conversion into FDCA. This rapid conversion is attributed to the freshly formed aldehyde group as a result of the oxidation of the primary alcohol moiety that was present in HMF. The catalysis experiments were continued from 6 to 24 h, where the quantity of FDCA detected increased from 32.5% to 99%. While the time to reach complete conversion of HMFCA was much longer (6 to 24 h), the final product, FDCA was detected in good amount (~99%). Unlike the existing reports, where the alcohol oxidation for FDCA production was carried out at higher temperatures and pressure (Casanova et.al., 2009; Koopman et.al., 2010; Gupta et.al., 2011; Albonetti et.al., 2012; Cai et.al., 2013; Jain et.al., 2015); in our experiments, the oxidation of the alcohol side chain associated with the HMF molecule was achieved at ambient pressure and temperature with unsupported Au nanoparticles.

No by-products were formed in all our studies and HMF was exclusively oxidized to HMFCA and subsequently to FDCA. The rate of formation of products and turnover frequency (TOF) of the reaction using the millifluidic reactor and flask reactor is listed in Table 5.3.

Table 5.2: Percentage of HMF converted and HMFCA and FDCA detected using batch reactor as a function of time

Exp. No.	Time (h)	HMF conversion (%)	HMFCA detected (%)	FDCA detected (%)
1	0	0	0	0
2	1	84	92.8	7.2
3	2	100	71.7	28.3
4	4	100	69.4	30.6
5	6	100	67.5	32.5
6	24	100	0	~99

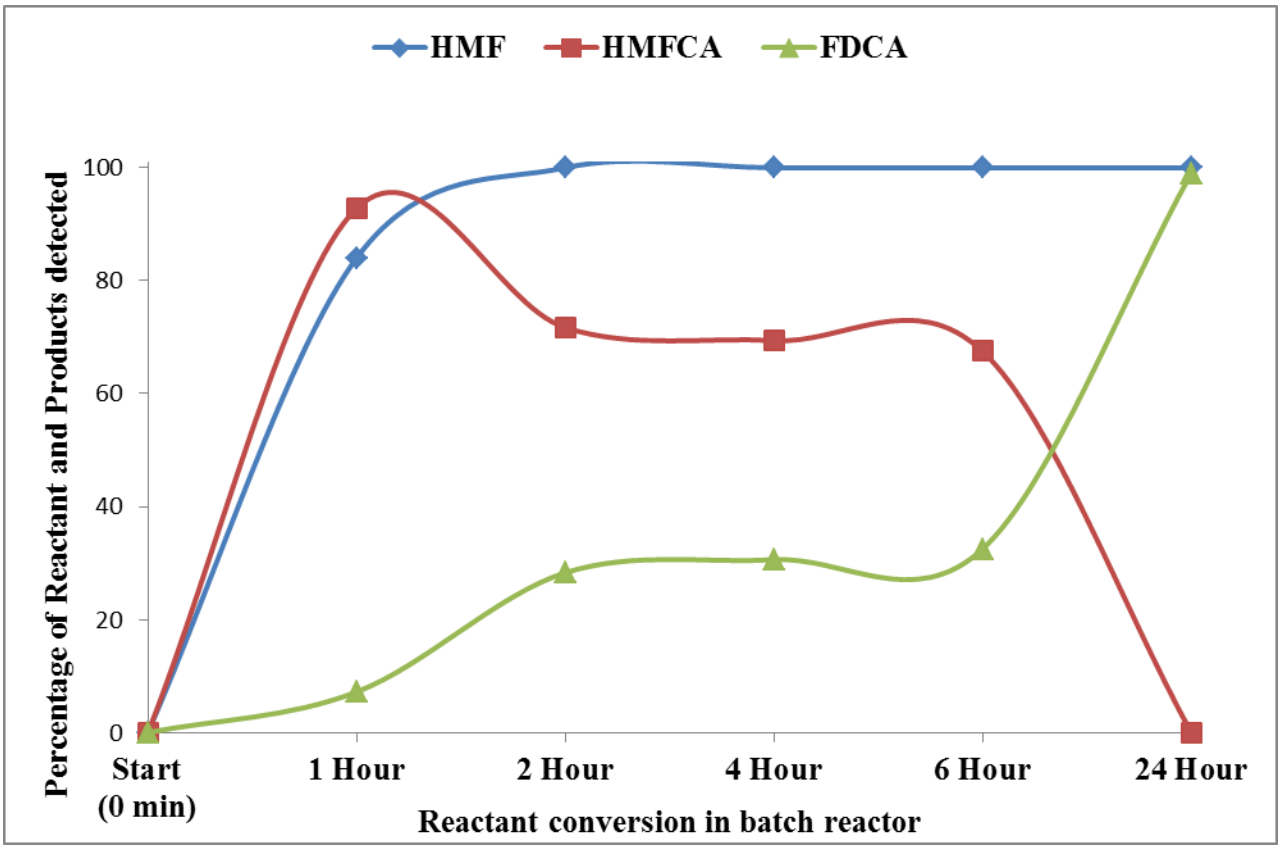

Figure 5.7: Oxidation of HMF to FDCA using flask with gold nanoparticles

Table 5.3: Rate of formation of products and turnover frequency of the reaction using the millifluidic reactor and flask reactor

	Millifluidic Reactor		Flask Reactor	
	HMFCA (After 50 min)	FDCA (After 50 min)	HMFCA (After 6 h)	FDCA (After 24 h)
Rate of Formation (M s^{-1})	$1.01*10^{-7}$	$3.76*10^{-8}$	$1.43*10^{-8}$	$1.28*10^{-9}$
Turnover Frequency (molecules s^{-1})	$4.10*10^{-26}$	$1.11*10^{-26}$	$1.87*10^{-28}$	$1.26*10^{-29}$

5.3.3 Effect of pressure, temperature, amount of base and catalyst

The oxidation of HMF in continuous flow millifluidic reactor as well as in conventional flask-based method required high base concentration for the production of FDCA, similar to Casanova et al. experiments (Casanova et.al, 2009). In all the cases, a stable intermediate, HMFCA was produced before sequentially oxidizing to FDCA. Several researchers have also followed the same protocol in order to maintain a high pH to oxidize the alcohol moiety of HMF either at high temperature or high pressure or both (Casanova et.al., 2009; Koopman et.al., 2010; Gupta et.al., 2011; Albonetti et.al., 2012; Cai et.al., 2013; Jain et.al., 2015). These stringent reaction conditions have been prone to molecule degradation, especially in the case of HMF. High catalyst loadings were used with these high pH conditions in order to rapidly convert all the HMF molecules to HMFCA (Zhang et.al, 2014), an intermediate product that is very stable in basic environment. Hansen et.al. (Hansen et.al, 2013) demonstrated the oxidation of HMF in various solvents at ambient temperature and pressure with TBHP in the absence of a base (NaOH). They have been successful in obtaining 50% yield of FDCA using CuCl catalyst with MeCN as solvent. However, their experiments with water as solvent resulted only in 3% yield of FDCA. The reason for such a less yield in the case of Hansen et al. and high FDCA yield in our case can be attributed to the presence of NaOH. The presence of base can facilitate dehydrogenation of hydroxyl groups, and reduce the amount of carboxylic acid adsorbed on the

catalyst surface, thus resulting in the availability of active sites in the catalyst (Cai et.al., 2013). In most of the previously reported literature, researchers have not been very successful in recycling their catalyst after each oxidation experiment due to problems such as ion leaching, high ratio of base under high temperature and high pressure conditions. Although much of the efforts had been towards increasing the FDCA yield, most of the previous works on HMF oxidation have been focused primarily to increase the efficiency of the catalyst performance. In our experiments, the concentration of NaOH used for the oxidation of HMF was maintained at a NaOH/HMF molar ratio of 4:1, similar to the protocol carried out by Casanova et al. (Casanova et.al., 2009).

The HPLC results of the samples collected using the continuous flow millifluidic chip reactor reveal that only 0.11 mM concentration of FDCA was obtained at the end of the reaction, which is 3.66% of the initial HMF concentration of 3 mM. These results were similar to the outcome reported by Hansen et.al (Hansen et. al, 2013) where a FDCA yield of 3% was obtained with an aqueous phase oxidizing agent using a batch reactor. The value of turnover frequency for FDCA in our experiments was calculated to be in the order of 10^{-26} & 10^{-29} S^{-1} for millifluidic and batch reactor respectively. These values are very less when compared to the turnover frequency for most industrial applications (10^{-2} to 10^{2} S^{-1}). These results more likely indicate very little conversion of HMF to HMFCA and FDCA, which is possibly due to the molecular degradation of HMF due to stringent reaction condition (Zhang et. al., 2014). To confirm this, a control experiment was conducted separately without the gold catalyst and the samples were analyzed using HPLC. The HPLC results revealed that the degradation of HMF molecule occurred as soon as it was mixed with TBHP and NaOH resulting in 1.7 mM concentration of HMF, which is accounted for 43% loss when compared to the initial HMF concentration of 3

mM. The control experiment was continued for 24 h and the HPLC results revealed 1.39 mM concentration of HMF, which is accounted for 53% loss. Another control experiment was carried out with HMFCA as the initial reactant and the samples were analyzed using HPLC. The HPLC results revealed 1.44 mM and 1.32 mM concentration of HMFCA at t = 0 and 24 h respectively, which is accounted for 52% and 56% loss due to degradation when compared to the initial concentration of 3 mM. The HPLC results of both the HMF and HMFCA control experiments did not show any conversion of the reactants into products. The results are tabulated in the appendix. Since the emphasis of this research is only to show the capability of millifluidic chip reactor to carry out time-resolved mapping of chemical processes, further experiments to improve the kinetics and mass balances were not performed.

5.4 Conclusions

A millifluidic chip-based reactor was utilized as a tool to carry out time-resolved study of HMF oxidation reaction. The reactions were carried out with the nanostructured gold catalyst coated within the reactor channel. The sequential transformation of the reactant (HMF) and the evolution of primary (HMFCA) and secondary products (FDCA) were analyzed using UV-Vis spectrophotometer and HPLC techniques with spatial resolution on the millifluidic chip. By mapping the gradual evolution of FDCA from HMF, a better understanding of the kinetics of the catalytic reaction was obtained. These analyses revealed that the oxidation was initiated at the aldehyde moiety before oxidizing the alcohol group associated with the HMF furan ring, thereby producing HMFCA as an intermediate. This novel approach of time-resolved study of catalytic reactions can be directly utilized to investigate and improve the catalytic yield and selectivity of various biomass conversions using continuous flow reactors. Future investigation towards this

reaction can be directed towards optimizing the reactant conditions in order to eliminate the degradation of HMF molecules as well as on efficiently facilitating the dehydrogenation of hydroxyl groups attached on the Au catalyst by using an optimum concentration of base to achieve 100% product yield. Or researchers wishing to better understand the reaction kinetics might consider picking a different cascade reaction.

CHAPTER 6: FINAL CONCLUSIONS

The use of LOCs as a tool for time resolved investigations is still an evolving field and is estimated to grow into a global scale for nanomaterials research due to its effective technique. The synthesis of nanoparticles using the LOCs has created an impact in various applications due to its high potential as a catalyst. Although several procedures are available to make nanoparticles for catalysis, advancements in the LOCs have set the need to synthesize efficient and atomically precise catalyst under continuous flow conditions. Most of the investigations mentioned above involved the utilization of X-ray instruments for time resolved measurements for the nanocatalyst synthesis and catalysis reactions using the continuous flow based LOCs. The generality of these instruments is that they can deduce the geometric and electronic properties of the reaction intermediates at various spatial intervals of the LOCs channel in real time. In addition to these X-ray instruments, optical tools such as UV-Vis absorption spectrophotometer, ultrafast spectroscopy, fluorescence spectroscopy, Raman spectroscopy and nuclear magnetic resonance spectroscopy can also be integrated with the LOCs to generate results on the properties of the nanoparticles (Yue et.al., 2012). These tools are noninvasive in nature and have the capability to probe the reactions in-situ to extract information on nanoparticle size, size distribution, surface uniformity, crystal structure, shape and reaction yield with time resolution. By exploiting the progress of nanoparticle synthesis using these instruments in real time, appropriate changes in the reactor parameters can be induced to optimize the reaction conditions to achieve precisely tailored nanoparticles using the LOCs. In addition, by integrating computational instruments to the LOCs, the entire process of nanoparticles synthesis can be systematically automated using user written algorithm to achieve feedback control in order to

tweak the reaction mechanism until a desired product is obtained. Incorporating these techniques would advance the process of nanoparticles synthesis to an autonomous level which can lead to rapid screening of products in shorter duration. For example, Krishnadasan et al. developed an online automated system to analyze the formation of cadmium selenide (CdSe) nanoparticles using a continuous flow microfluidic reactor (Krishnadasan et.al., 2004). Similarly, Toyota et.al. demonstrated the use of inline fluorescence spectroscopy to optimize the synthesis of CdSe quantum dots using five parallel microreactors (Toyota et.al., 2010). Conducting time resolved investigations using LOCs coupled to the online monitoring automation systems with feedback control would provide an opportunity to scale up a process with chemoselectivity. Although these investigations seem to be complicated, the actual results obtained are systematic, accurate and require less time. Mainly, the versatility of the LOC rectors in terms of its compatibility to hold high concentrated solutions and its ability to provide real time probing window for time resolved studies for nanoparticle synthesis, has to be determined to design autonomous reactors for synthesizing various nanoparticles.

REFERENCES

1. Abahmane L, Knauer A, Ritter U, Köhler JM, Groß GA. (2009). Heterogeneous Catalyzed Pyridine Synthesis using Montmorillionite and Nanoparticle-Impregnated Alumina in a Continuous Micro Flow System. *Chemical Engineering & Technology,* 32(11), 1799-1805

2. Abahmane L, Köhler JM, Groß, GA. (2011). Gold-Nanoparticle-Catalyzed Synthesis of Propargylamines: The Traditional A3-Multicomponent Reaction Performed as a Two-Step Flow Process. *Chemistry – A European Journal,* 17(10), 3005-3010.

3. Abahmane L, Knauer A, Köhler JM, Groß GA. (2011). Synthesis of polypyridine derivatives using alumina supported gold nanoparticles under micro continuous flow conditions. *Chemical Engineering Journal,* 167(2–3), 519-526

4. Abou Hassan A, Sandre O, Cabuil V, Tabeling P. (2008). Synthesis of iron oxide nanoparticles in a microfluidic device: preliminary results in a coaxial flow millichannel. *Chemical Communications,* 0(15), 1783-1785.

5. Abou-Hassan A, Bazzi R, Cabuil V. (2009). Multistep Continuous-Flow Microsynthesis of Magnetic and Fluorescent γ-Fe2O3@SiO2 Core/Shell Nanoparticles. *Angewandte Chemie International Edition,* 48(39), 7180-7183.

6. Adleman, J.R., Boyd, D.A., Goodwin, D.G., and Psaltis, D. (2009). Heterogenous catalysis mediated by plasmon heating. *Nano Lett.* 9, 4417–4423

7. Ahmadi TS, Wang ZL, Green TC, Henglein A, El-Sayed MA. (1996). Shape-Controlled Synthesis of Colloidal Platinum Nanoparticles. *Science,* 272(5270), 1924-1925.

8. Albonetti, S., Pasini, T., Lolli, A., Blosi, M., Piccinini, M., Dimitratos, N., Lopez-Sanchez, J.A., Morgan, D.J., Carley, A.F., Hutchings, G.J., and Cavani, F. (2012). Selective oxidation of 5-hydroxymethyl-2-furfural over TiO2-supported gold–copper catalysts prepared from preformed nanoparticles: Effect of Au/Cu ratio. *Catalysis Today,* 195, 120 – 126.

9. Ali MRK, Snyder B, El-Sayed MA. (2012). Synthesis and Optical Properties of Small Au Nanorods Using a Seedless Growth Technique. *Langmuir,* 28(25), 9807-9815.

10. An, K., and Somorjai, G.A. (2012). Size and shape control of metal nanoparticles for reaction selectivity in catalysis. *ChemCatChem*, 4 (10), 1512–1524.

11. Andreescu D, Sau TK, Goia, DV. (2006) Stabilizer-free nanosized gold sols. *Journal of Colloid and Interface Science*, 298(2), 742-751.

12. Auer, S., and Frenkel, D. (2001) Prediction of absolute crystal-nucleation rate in hard-sphere colloids. *Nature*, 409(6823), 1020-1023.

13. Barakat T, Rooke JC, Genty E, Cousin R, Siffert S, Su BL. (2013) Gold catalysts in environmental remediation and water-gas shift technologies. *Energy & Environmental Science,* 6(2), 371-391.

14. Bénard, J.; Oudar, J.; Barbouth, N.; Margot, E.; Berthier, Y. (1979). The thermodynamics of some metallic 2D sulphides. *Surf. Sci.,* 88, 2-3, L35-L41.

15. Berger RL, Balko B, Chapman HF. (1968). High Resolution Mixer for the Study of the Kinetics of Rapid Reactions in Solution. *Review of Scientific Instruments,* 39(4), 493-498.

16. Biswas, S., Miller, J.T., Li, Y., Nandakumar, K., and Kumar, C.S.S.R. (2012) Millifluidics: Developing a Millifluidic Platform for the Synthesis of Ultrasmall Nanoclusters: Ultrasmall Copper Nanoclusters as a Case Study. *Small,* 8(5), 688 - 698.

17. Boleininger, J, Kurz A, Reuss V, Sonnichsen C. (2006). Microfluidic continuous flow synthesis of rod-shaped gold and silver nanocrystals. *Physical Chemistry Chemical Physics,* 8(33), 3824-3827.

18. Bozell, J.J., and Petersen, G.R. (2010). Technology development for the production of biobased products from biorefinery carbohydrates – the US Department of Energy's "Top 10" revisited. *Green Chem.,* 12, 539 - 554.

19. Brege, J. J.; Hamilton, C. E.; Crouse, C. A.; Barron, A. R. (2009). Ultrasmall copper nanoparticles from a hydrophobically immobilized surfactant template. *Nano Lett.,* 9, 2239−2242.

20. Brivio M, Verboom W, Reinhoudt DN. (2006). Miniaturized continuous flow reaction vessels: influence on chemical reactions. *Lab on a Chip,* 6(3), 329-344.

21. Brumbaugh A.D; Cohen, K.A.; and St. Angelo, S. K. (2014). Ultrasmall Copper Nanoparticles Synthesized with a Plant Tea Reducing Agent. *ACS Sustainable Chem. Eng.,* 2, 1933−1939

22. Brust M, Walker M, Bethell D, Schiffrin DJ, Whyman R. (1994). Synthesis of thiol-derivatised gold nanoparticles in a two-phase Liquid-Liquid system. *Journal of the Chemical Society, Chemical Communications,* 0(7), 801-802.

23. Cabeza VS, Kuhn S, Kulkarni AA, Jensen KF. (2012). Size-Controlled Flow Synthesis of Gold Nanoparticles Usinga Segmented Flow Microfluidic Platform. *Langmuir,* 28, 7007−7013

24. Cacciuto, A., Auer, S., and Frenkel, D. (2004). Onset of heterogeneous crystal nucleation in colloidal suspensions. *Nature,* 428(6981), 404-406.

25. Cai, J., Ma, H., Zhang, J., Song, Q., Du, Z., Huang, Y., and Xu, J. (2013). Gold Nanoclusters Confined in a Supercage of Y Zeolite for Aerobic Oxidation of HMF under Mild Conditions. *Chem. Eur. J.,* 19, 14215 – 14223

26. Cao E, Sankar M, Firth S, Lam KF, Bethell D, Knight DK., Gavriilidis A. (2011). Reaction and Raman spectroscopic studies of alcohol oxidation on gold–palladium catalysts in microstructured reactors. *Chemical Engineering Journal*, 167(2–3), 734-743.

27. Casanova, O., Iborra, S., and Corma, A. (2009). Biomass into Chemicals: Aerobic Oxidation of 5-Hydroxymethyl- 2-furfural into 2,5-Furandicarboxylic Acid with Gold Nanoparticle Catalysts. *ChemSusChem,* 2, 1138 – 1144

28. Chan E.M., Mathies RA, Alivisatos AP. (2003). Size-Controlled Growth of CdSe Nanocrystals in Microfluidic Reactors. *Nano Letters*, 3(2), 199-201.

29. Chan, E.M., Marcus, M.A., Fakra, S., Elnaggar, M., Mathies, R.A., and Alivisatos, A.P. (2007). Millisecond kinetics of nanocrystal cation exchange using microfluidic X-ray absorption spectroscopy. *J. Phys. Chem. A.,* 111, 12210–12215.

30. Chang JY, Yang CH, Huang KS. (2007) Microfluidic assisted preparation of CdSe/ZnS nanocrystals encapsulated into poly(DL-lactide- co -glycolide) microcapsules. *Nanotechnology*, 18(30), 305305.

31. Chaturvedi S, Dave PN, Shah NK. (2012). Applications of nano-catalyst in new era. *Journal of Saudi Chemical Society,* 16(3), 307-325.

32. Che, M. (2013) Nobel Prize in chemistry 1912 to Sabatier: Organic chemistry or catalysis? *Catalysis Today,* 218–219, 162–171.

33. Chen MS, Goodman DW. (2004). The Structure of Catalytically Active Gold on Titania. *Science,* 306(5694), 252-255.

34. Chen-Hsun W, Chih-Chia H, Chen-Sheng Y, Huan-Yao L, Gwo-Bin L. (2008). Synthesis of hexagonal gold nanoparticles using a microfluidic reaction system. *Journal of Micromechanics and Microengineering,* 18(3), 035019.

35. Cheng, Y., and Huber, G.W. (2011). Chemistry of Furan Conversion into Aromatics and Olefins over HZSM-5: A Model Biomass Conversion Reaction. *ACS Catal.*, 1(6), 611 – 628

36. Chiang, L.Y.; Swirczewski, J. W.; Kastrup, R.; Hsu, C. S.; Upasani, R. B. (1991). Chemistry of Catalytic Dehydrogenative Oligomerization of Tetrahydroquinoline and Structural Characterization of Nonsubstituted Quinoline Oligomers. *J. Am. Chem. Soc.,* 113, 6574-6548.

37. Cho A. (2003). Connecting the Dots to Custom Catalysts. *Science,* 299(5613), 1684-1685.

38. Chrimes AF, Khoshmanesh K, Stoddart PR, Mitchell A, Kalantar-zadeh K. (2013). Microfluidics and Raman microscopy: current applications and future challenges. *Chem. Soc. Rev.,* 42, 5880-5906

39. Conte M, Carleya AF, Heirene C, Willocka DJ, Johnston P, Herzing AA, Kielyc CJ, Hutchings GJ. (2007). Hydrochlorination of acetylene using a supported gold catalyst: A study of the reaction mechanism. *Journal of Catalysis,* 250, 231–239.

40. Coquet R, Howard KL, Willock DJ. (2008). Theory and simulation in heterogeneous gold catalysis. *Chem. Soc. Rev.,* 37, 2046-2076.

41. Corma A, Garcia H. (2008). Supported gold nanoparticles as catalysts for organic reactions. *Chemical Society Reviews,* 37(9), 2096-2126.

42. Corma A, Serna P. (2012). Gold-Catalyzed Reduction Reactions, in Modern Gold Catalyzed Synthesis (eds A. S. K. Hashmi and F. D. Toste), *Wiley-VCH Verlag GmbH & Co. KGaA,* Weinheim, Germany, 27-54.

43. Cuenya BR. (2010). Synthesis and catalytic properties of metal nanoparticles: Size, shape, support, composition, and oxidation state effects. *Thin Solid Films,* 518(12), 3127-3150.

44. Dahl JA, Maddux BLS, Hutchison JE. (2007). Toward Greener Nanosynthesis. *Chemical Reviews,* 107(6), 2228-2269.

45. Davis, S.E., Zope, B.N., and Davis, R.J. (2012). On the mechanism of selective oxidation of 5-hydroxymethylfurfural to 2,5-furandicarboxylic acid over supported Pt and Au catalysts. *Green Chem.,* 14, 143 – 147

46. Davis, S.E., Houk, L.R., Tamargo, E.C., Datye, A.K., and Davis, R.J. (2011). Oxidation of 5-hydroxymethylfurfural over supported Pt, Pd and Au catalysts. *Catalysis Today*, 160, 55 – 60

47. De Jong KP. (2009). Synthesis of Solid Catalysts. *Wiley-VCH: Weinheim*.

48. DeMello AJ. (2006). Control and detection of chemical reactions in microfluidic systems. *Nature,* 442(7101), 394-402.

49. De Menech M, Garstecki P, Jousse F, Stone HA. (2008). Transition from squeezing to dripping in a microfluidic T-shaped junction. *J. Fluid Mech.,* 595, 141–161.

50. Donati G, Paludetto R. (1999). Batch and semibatch catalytic reactors (from theory to practice). *Catalysis Today,* 52(2–3), 183-195.

51. Dunnewijk J, Bosch H, De Haan, AB. (2004). Reverse flow adsorption: integrating the recovery and recycling of homogeneous catalysts. *Separation and Purification Technology,* 40(3), 317-320.

52. Duraiswamy S, Khan SA. (2009). Droplet-Based Microfluidic Synthesis of Anisotropic Metal Nanocrystals. *Small,* 5(24), 2828-2834.

53. Dushkin, C.D., Yoshimura, H., and Nagayama, K. (1993). Nucleation and growth of two-dimensional colloidal crystals. *Chemical Physics Letters,* 204(5-6), 455–460.

54. Edel JB, Fortt R, DeMello JC, DeMello AJ. (2002). Microfluidic routes to the controlled production of nanoparticles. *Chemical Communications,* 0(10), 1136-1137.

55. Eijsbouts, S.; De Beer, V.H.J.; Prins, R. (1988). Periodic trends in the hydronitrogenation activity of carbon supported transition metal sulfide catalysts. *J. Catal.,* 109, 217-220.

56. Elvira, K.S., Solvas, X., Wootton, R.C.R., and DeMello, A.J. (2013). The past, present and potential for microfluidic reactor technology in chemical synthesis. *Nat. Chem.,* 5, 905-915.

57. Engl W, Tachibana M, Panizza P, Backov R. (2007). Millifluidic as a versatile reactor to tune size and aspect ratio of large polymerized objects. *International Journal of Multiphase Flow,* 33(8), 897-903.

58. Eustis S, El-Sayed MA. (2006). Why gold nanoparticles are more precious than pretty gold: Noble metal surface plasmon resonance and its enhancement of the radiative and nonradiative properties of nanocrystals of different shapes. *Chem. Soc. Rev.,* 35, 209–217

59. Fair RB, Khlystov A, Tailor TD, Ivanov V, Evans RD, Griffin PB, Zhou J. (2007). Chemical and Biological Applications of Digital-Microfluidic Devices. *Design & Test of Computers, IEEE,* 24(1), 10-24.

60. Frens G. (1973). Controlled nucleation for the regulation of the particle size in monodisperse gold suspensions. *Nat. Phys. Sci. (Lond.),* 241, 20-22.

61. Frost CG, Mutton, L. (2010). Heterogeneous catalytic synthesis using microreactor technology. *Green Chemistry,* 12(10), 1687-1703.

62. Gaur S, Miller JT, Stellwagen D, Sanampudi A, Kumar CSSR, and Spivey JJ. (2012). Synthesis, characterization, and testing of supported Au catalysts prepared from atomically-tailored $Au_{38}(SC_{12}H_{25})_{24}$ clusters. *Phys. Chem. Chem. Phys,* 14(5), 1627-1634

63. Gaur S, Johansson S, Mohammad F, Kumar C, Spivey JJ. (2012). Catalytic Activity of Titania-Supported Core–Shell Fe_3O_4@Au Nano-Catalysts for CO Oxidation. *J. Phys. Chem. C, 116 (42), 22319–22326.*

64. Gaur S, Wu H, Stanley GG, More K, Kumar CSSR, Spivey JJ. (2013). CO oxidation studies over cluster-derived Au/TiO_2 and AURO*lite*™ Au/TiO_2 catalysts using DRIFTS. *Catalysis Today,* 208, 72 - 81

65. Ghosh, S. K.; Rahman, D. S.; Ali, A. L.; Kalita, A. (2013). Surface plasmon tunability and emission sensitivity of ultrasmall fluorescent copper nanoclusters. *Plasmonics,* 8, 1457−1468.

66. Goeres DM, Hamilton MA, Beck NA, Buckingham-Meyer K, Hilyard JD, Loetterle LR, Lorenz LA, Walker DK, Stewart PS. (2009)A method for growing a biofilm under low shear at the air–liquid interface using the drip flow biofilm reactor. *Nature protocols,* 4, 783-788.

67. Gole A, Murphy CJ. (2004). Seed-Mediated Synthesis of Gold Nanorods: Role of the Size and Nature of the Seed. *Chemistry of Materials,* 16(19), 3633-3640.

68. Gorbanev, Y.Y., Klitgaard, S.K., Woodley, J.M., Christensen, C.H., and Riisager, A. (2009). Gold-Catalyzed Aerobic Oxidation of 5-Hydroxymethylfurfural in Water at Ambient Temperature. *ChemSusChem,* 2, 672 – 675.

69. Göröcs, Z., and Ozcan, A. (2013). On-chip biomedical imaging. *IEEE Rev Biomed Eng.,* 6, 29–46.

70. Goswami, N., Chaudhuri, S., Giri, A., Lemmens, P., and Pal, S.K. (2014). Surface engineering for controlled nanocatalysis: key dynamical events from ultrafast electronic spectroscopy. *J. Phys. Chem. C.,* 118, 23434−23442.

71. Gou L, Murphy CJ. (2005). Fine-Tuning the Shape of Gold Nanorods. *Chemistry of Materials,* 17(14), 3668-3672.

72. Gravesen P, Branebjerg J, Jensen OS. (1993). Microfluidics-a review. *Journal of Micromechanics and Microengineering,* 3(4), 168.

73. Gross, E., Shu, X,Z., Alayoglu, S., Bechtel, H.A., Martin, M.C., Toste, F.D., and Somorjai, G.A. (2014). In situ IR and X-ray high spatial-resolution microspectroscopy measurements of multistep organic transformation in flow microreactor catalyzed by Au nanoclusters. *J. Am. Chem. Soc.,* 136, 3624−3629.

74. Guo S, Wang L, Wang E. (2007). Templateless, surfactantless, simple electrochemical route to rapid synthesis of diameter-controlled 3D flowerlike gold microstructure with "clean" surface. *Chem Commun (Camb),* (30), 3163-3165.

75. Gupta, N.K., Nishimura, S., Takagaki, A., and Ebitani, K. (2011). Hydrotalcite-supported gold-nanoparticle-catalyzed highly efficient base-free aqueous oxidation of 5-hydroxymethylfurfural into 2,5-furandicarboxylic acid under atmospheric oxygen pressure. *Green Chem.,* 13, 824 - 827

76. Hammer B, Norskov JK. (2002). Why gold is the noblest of all the metals? *Nature,* 376, 238 – 240.

77. Hansen, T.S., Sádaba, I., García-Suárez, E.J., and Riisager, A. (2013). Cu catalyzed oxidation of 5-hydroxymethylfurfural to 2,5-diformylfuran and 2,5-furandicarboxylic acid under benign reaction conditions. *Applied Catalysis A: General*, 456, 44 – 50.

78. Harris,S.; Chiannelli, R.R. (1983). Periodic effects in catalysis: the relation between trends in catalytic activity and calculated electronic structure of transition metal sulfides. *Chem. Phys. lett,* 101, 603-605

79. Harris, S.; Chianelli, R.R. (1984). Catalysis by transition metal sulfides: the relation between calculated electronic trends and HDS activity. *J.Catal.*, 86, 400-412.

80. Harris. S.; Chiannelli, R.R. (1986). Catalysis by transition metal sulfides: a theoretical and experimental study of the relation between the synergic systems and the binary transition metal sulfides. *J. catal.*, 98, 17-31.

81. Hartman, R.L., and Jensen, K.F. (2009). Microchemical systems for continuous-flow synthesis. *Lab Chip*, 9, 2495 – 2507.

82. Haruta M, Kobayashi T, Sano H, Yamada N. (1987). Novel Gold Catalysts for the Oxidation of Carbon Monoxide at a Temperature far below 0ºC. *Chemistry Letters,* 16(2), 405-408.

83. Haruta M. (1997). Novel catalysis of gold deposited on metal oxides. *Catalysis Surveys of Japan,* 1, 61 – 73

84. Haruta M. (1997). Size- and support-dependency in the catalysis of gold. *Catalysis Today,* 36(1), 153-166.

85. Haruta, M. (2003). When Gold Is Not Noble: Catalysis by Nanoparticles. *The Chemical Record,* 3, 75–87.

86. Hashmi SK, Hutchings GJ. (2006). Gold Catalysis. *Angew. Chem. Int. Ed.,* 45, 7896 – 7936

87. He S, Liu Y, Uehara M, Maeda H. (2007). Continuous micro flow synthesis of ZnO nanorods with UV emissions. *Materials Science and Engineering: B,* 137(1–3), 295-298.

88. Hinsmann, P., Frank, J., Svasek, P., Harasek, M., and Lendl, B. (2001). Design, simulation and application of a new micromixing device for time resolved infrared spectroscopy of chemical reactions in solution. *Lab Chip*, 1, 16-21.

89. Huang CT, Peretfi SW, Bryers JD. (1992). Use of flow cell reactors to quantify biofilm formation kinetics. *Biotechnology techniques,* 6 (3), 193-198.

90. Huber, G.W., Iborra, S., and Corma, A. (2006). Synthesis of Transportation Fuels from Biomass: Chemistry, Catalysts, and Engineering. *Chem. Rev,* 106, 4044 - 4098.

91. Hutchings GJ, Kiely CJ. (2013). Strategies for the Synthesis of Supported Gold Palladium Nanoparticles with Controlled Morphology and Composition. *Acc. Chem. Res.*, *46* (8), 1759–1772

92. Hwang DK, Dendukuri D, Doyle PS. (2008). Microfluidic-based synthesis of non-spherical magnetic hydrogel microparticles. *Lab on a Chip,* 8(10), 1640-1647.

93. Ishizaka T, Ishigaki A, Chatterjee M, Suzuki A, Suzuki TM, Kawanami H. (2012). Continuous Fabrication of Novel Polyimide Nanoparticles Confining Highly Dispersed Gold Nanoparticles by a Multistep Microfluidic Reaction System and Their Catalytic Application. *Chemistry Letters,* 41(4), 447-449.

94. Ismagilov IZ, Michurin EM, Sukhova OB, Tsykoza LT, Matus EV, Kerzhentsev MA, Ismagilov ZR, Zagoruiko AN, Rebrov EV, De Croon MHJM, Schouten JC. (2008). Oxidation of organic compounds in a microstructured catalytic reactor. *Chemical Engineering Journal,* 135S, S57–S65

95. Jain, A., Jonnalagadda, S.C., Ramanujachary, K.V., Mugweru, A. (2015). Selective oxidation of 5-hydroxymethyl-2-furfural to furan-2,5-dicarboxylic acid over spinel mixed metal oxide catalyst. *Catalysis Communications,* 58, 179 – 182

96. Jamal F, Jean-Sébastien G, Maël P, Edmond P, Christian R. (2012). Gold nanoparticle synthesis in microfluidic systems and immobilisation in microreactors designed for the catalysis of fine organic reactions. *Microsystem technologies,* 18(2), 151-158.

97. Jana NR, Gearheart L, Murphy CJ. (2001). Seed-Mediated Growth Approach for Shape-Controlled Synthesis of Spheroidal and Rod-like Gold Nanoparticles Using a Surfactant Template. *Advanced Materials,* 13(18), 1389-1393.

98. Jana NR. (2005). Gram-Scale Synthesis of Soluble, Near-Monodisperse Gold Nanorods and Other Anisotropic Nanoparticles. *Small,* 1(8-9), 875-882.

99. Jensen KF. (2001). Microreaction engineering — is small better? *Chemical Engineering Science,* 56(2): 293-303.

100. Jin R, Qian H, Wu Z, Zhu Y, Zhu M, Mohanty A, Garg N. (2010). Size Focusing: A Methodology for Synthesizing Atomically Precise Gold Nanoclusters. *J. Phys. Chem. Lett., 1,* 2903–2910.

101. Jin R, Qian H, Zhu Y, Das A. (2011). Atomically Precise Nanoparticles: A New Frontier in Nanoscience. *J. Nanosci. Lett., 1*, 72–86

102. Juárez R, Pennemann H, García H. (2011). Continuous flow carbamoylation of aniline by dimethyl carbonate using a microreactor coated with a thin film of ceria supported gold nanoparticles. *Catalysis Today*, 159(1), 25-28.

103. Jun H, Fabienne T, Florent M, Coulon PE, Nicolas M, Olivier S. (2012). Understanding of the Size Control of Biocompatible Gold Nanoparticles in Millifluidic Channels. *Langmuir*, 28(45), 15966-15974.

104. Kakuta, M., Jayawickrama, D.A., Wolters, A.M., Manz, A., and Sweedler, J.V. (2003). Micromixer-based time-resolved NMR: Applications to ubiquitin protein conformation. *Anal. Chem.,* 75(4), 956–960.

105. Kalinin Y.V., Murali, A., and Gracias, D.H. (2012). Chemistry with spatial control using particles and streams. *RSC Advances,* 2, 9707 – 9726.

106. Koopman, F., Wierckx, N., De Winde, J.H., and Ruijssenaars, H.J. (2010). Efficient whole-cell biotransformation of 5-(hydroxymethyl)furfural into FDCA, 2,5-furandicarboxylic acid. *Bioresource Technology*, 101, 6291–6296.

107. Khan SA, Jensen KF. (2007). Microfluidic Synthesis of Titania Shells on Colloidal Silica. *Advanced Materials*, 19(18), 2556-2560.

108. Kim JW, Utada AS, Fernández-Nieves A, Hu Z, Weitz DA. (2007). Fabrication of Monodisperse Gel Shells and Functional Microgels in Microfluidic Devices. *Angewandte Chemie International Edition*, 46(11), 1819-1822.

109. Kitson PJ, Rosnes MH, Sans V, Dragone V, Cronin L. (2012). Configurable 3D-Printed millifluidic and microfluidic 'lab on a chip' reactionware devices. *Lab on a Chip*, 12(18), 3267-3271.

110. Kliche, G. (1985). Far-infrared reflection spectra of Pdo, PdS, PdSe and PtS. *Infrared Physics*, 25, 381 (ir).

111. Kohler JM, Wagner J, Albert J. (2005). Formation of isolated and clustered Au nanoparticles in the presence of polyelectrolyte molecules using a flow-through Si chip reactor. *Journal of Materials Chemistry*, 15(19), 1924-1930.

112. Köhler JM, Abahmane L, Wagner J, Albert J, Mayer G. (2008). Preparation of metal nanoparticles with varied composition for catalytical applications in microreactors. *Chemical Engineering Science*, 63(20), 5048-5055.

113. Krishna K.S., Navin, C.V. Biswas, S., Singh, V., Ham, K., Bovenkamp, G.L., Theegala, C.S., Miller, J.T., Spivey, J., and Kumar, C.S.S.R. (2013). Millifluidics for time-resolved mapping of the growth of gold nanostructures. *J. Am. Chem. Soc.,* 135(14), 5450-5456.

114. Krishna, K.S., Biswas, S., Navin, C.V., Yamane, D.G., Miller, J.T., and Kumar, C.S.S.R. (2013). Millifluidics for chemical synthesis and time-resolved mechanistic studies. *J. Vis. Exp.,* 81(e50711), 1-9.

115. Krishna, K.S., Li, Y., Li, S., and Kumar, C.S.S.R. (2013). Lab-on-a-chip synthesis of inorganic nanomaterials and quantum dots for biomedical applications. *Adv. Drug Delivery Rev.,* 65, 1470–1495.

116. Krishnadasan, S., Tovilla, J., Vilar, R., DeMello, A.J., and DeMello J.C. (2004). On-line analysis of CdSe nanoparticle formation in a continuous flow chip-based microreactor. *J. Mater. Chem.,* 14, 2655 – 2660.

117. Kusema BT, Murzin DY. (2013). Catalytic oxidation of rare sugars over gold catalysts. *Catalysis Science & Technology,* 3(2), 297-307.

118. Kwon, S. G.; Hyeon, T. (2011). Formation Mechanisms of Uniform Nanocrystals Via Hot-Injection and Heat-up Methods. *Small,* 7, 2685-2702.

119. Lamer, V. K.; Dinegar, R. H. (1950). Theory, Production and Mechanism of Formation of Monodispersed Hydrosols. *Journal of the American Chemical Society,* 72, 4847-4854.

120. Lazarus LL, Yang ASJ, Chu S, Brutchey RL, Malmstadt N. (2010). Flow-focused synthesis of monodisperse gold nanoparticles using ionic liquids on a microfluidic platform. *Lab Chip,* 10, 3377–3379.

121. Li Z, Ravaine V, Ravaine S, Garrigue P, Kuhn A. (2007). Raspberry-like Gold Microspheres: Preparation and Electrochemical Characterization. *Advanced Functional Materials,* 17(4), 618-622.

122. Li, P.; Wu, J.; Lin, J.; Huang, M.; Lan, Z.; Li, Q. (2008). Improvement of performance of dye-sensitized solar cells based on electrodeposited-platinum counter electrode. *Electrochimica Acta,* 53, 4161–4166.

123. Li P, Lei N, Sheadel DA, Xu J, Xue W. (2012). Integration of nanosensors into a sealed microchannel in a hybrid lab-on-a-chip device. *Sensors and Actuators B: Chemical,* 166–167(0): 870-877.

124. Li, Y., Sanampudi, A., Reddy, V.R., Biswas, S., Nandakumar, K., Yamane, D.G., Goettert, J.S., and Kumar, C.S.S.R. (2012). Size evolution of gold nanoparticles in a millifluidic reactor. *Phys. Chem. Phys.,* 13(1), 177-182.

125. Lilga, M.A., Hallen, R.T., and Gray, M. (2010). Production of Oxidized Derivatives of 5-Hydroxymethylfurfural (HMF). *Top Catal,* 53:1264 – 1269

126. Liu H, Huang J, Sun D, Lin L, Lin W, Li J, Li Q. (2012). Microfluidic biosynthesis of silver nanoparticles: Effect of process parameters on size distribution. *Chemical Engineering Journal*, 209(0), 568-576.

127. Liu X, Unal B, Jensen KF. (2012). Heterogeneous catalysis with continuous flow microreactors. *Catalysis Science & Technology*, 2(10), 2134-2138.

128. Liu J, Krishna KS, Losovyj YB, Chattopadhyay S, Lozova N, Miller JT, Spivey JJ, Kumar CSSR. (2013). Ligand-Stabilized and Atomically Precise Gold Nanocluster Catalysis: ACase Study for Correlating Fundamental Electronic Properties with Catalysis. *Chem. Eur. J.*, 19, 10201 – 10208

129. Lohse SE, Eller JR, Sivapalan ST, Plews MR, Murphy CJ. (2013). A Simple Benchtop Reactor System for the High-Throughput Synthesis and Functionalization of Gold Nanoparticles (AuNPs) with Different Sizes and Shapes. *ACS Nano*, 7(5), 4135-4150.

130. Lopez-Sanchez JA, Dimitratos N, Hammond C, Brett GL, Kesavan L, White S, Miedziak P, Tiruvalam R, Jenkins RL, Carley AF, Knight D, Kiely CJ, Hutchings GJ. (2011). Facile removal of stabilizer-ligands from supported gold nanoparticles. *Nature Chemistry*, 3, 551–556.

131. Lorber N, Sarrazin F, Guillot P, Panizza P, Colin A, Pavageau B, Mignard E. (2011). Some recent advances in the design and the use of miniaturized droplet-based continuous process: Applications in chemistry and high-pressure microflows. *Lab on a Chip*, 11(5), 779-787.

132. Lu Z, McMahon J, Mohamed H, Barnard D, Shaikh TR, Mannella CA, Lu TM. (2010). Passive Microfluidic device for Sub Millisecond Mixing. *Sensors and actuators. B, Chemical*, 144(1), 301-309.

133. Ma Z, Dai S. (2011). Design of Novel Structured Gold Nanocatalysts. *ACS Catalysis*, 1(7), 805-818.

134. Ma C, Xue W, Li J, Xing W, Hao Z. (2013). Mesoporous carbon-confined Au catalysts with superior activity for selective oxidation of glucose to gluconic acid. *Green Chemistry*, 15(4), 1035-1041.

135. MacDonald M. A, Zhang P, Qian H, Jin R. (2010). Site-Specific and Size-Dependent Bonding of Compositionally Precise Gold−Thiolate Nanoparticles from X-ray Spectroscopy. *J. Phys. Chem. Lett., 1*, 1821–1825.

136. Macintyre, J.E. *Dictionary of inorganic compounds.* Volume 3, 3781.

137. Malik, M.A.; O'Brien, P.; Revaprasadu, N. (2002). Synthesis of TOPO-capped PtS and PdS nanoparticles from [$Pt(S_2CNMe(Hex))_2$] and [$Pd(S_2CNMe(Hex))_2$]. *J. Mater. Chem.,* 12, 92-97.

138. Marre S, Roig Y, Aymonier C. (2012). Supercritical microfluidics: Opportunities in flow-through chemistry and materials science. *The Journal of Supercritical Fluids,* 66(0), 251-264.

139. Marre, S., and Jensen, K.F. (2010). Synthesis of micro and nanostructures in microfluidic systems. *Chem. Soc. Rev.,* 39, 1183–1202.

140. Martínez-Cisneros CS, Pedro SGD, Puyol M, García-García J, Alonso-Chamarro J. (2012). Design, fabrication and characterization of microreactors for high temperature syntheses. *Chemical Engineering Journal,* 211–212(0), 432-441

141. McEwana L, Juliusa M, Roberts S, Fletcher JCQ. (2010). A review of the use of gold catalysts inselective hydrogenation reactions. *Gold Bulletin Volume,* 43(4), 298 – 306.

142. Merkoçia, A., and Kutter, J.P. (2012). Analytical miniaturization and nanotechnologies. *Lab Chip,* 12, 1915–1916.

143. Mielby J, Kegnæs S, Fristrup P. (2012). Gold Nanoparticle-Catalyzed Formation of Nitrogen-containing Compounds—From Mechanistic Understanding to Synthetic Exploitation. *ChemCatChem,* 4(8), 1037-1047.

144. Mikami Y, Dhakshinamoorthy A, Alvaro M, Garcia H. (2013). Catalytic activity of unsupported gold nanoparticles. *Catalysis Science & Technology,* 3(1), 58-69.

145. Min BK, Friend CM. (2007). Heterogeneous Gold-Based Catalysis for Green Chemistry: Low-Temperature CO Oxidation and Propene Oxidation. *Chem. Rev.,* 107, 2709-2724

146. Murphy CJ, Jana NR. (2002). Controlling the Aspect Ratio of Inorganic Nanorods and Nanowires. *Advanced Materials,* 14(1), 80-82.

147. Murphy CJ. (2008). Sustainability as an emerging design criterion in nanoparticle synthesis and applications. *Journal of Materials Chemistry,* 18(19), 2173-2176.

148. Murray, C.B., Kagan, C.R., and Bawendi, M.G. (2000). Synthesis and characterization of monodisperse nanocrystals and close-packed nanocrystal assemblies. *Annu. Rev. Mater. Sci.,* 30, 545-610.

149. Miyamura H, Matsubara R, Miyazaki Y, Kobayashi S. (2007). Aerobic Oxidation of Alcohols at Room Temperature and Atmospheric Conditions Catalyzed by Reusable Gold Nanoclusters Stabilized by the Benzene Rings of Polystyrene Derivatives. *Angewandte Chemie,* 119(22), 4229-4232.

150. Miyamura H, Matsubara R, Miyazaki Y, Kobayashi S. (2007). Aerobic Oxidation of Alcohols at Room Temperature and Atmospheric Conditions Catalyzed by Reusable Gold Nanoclusters Stabilized by the Benzene Rings of Polystyrene Derivatives. *Angewandte Chemie International Edition,* 46(22), 4151-4154.

151. Nakamura H, Yamaguchi Y, Miyazaki M, Maeda H, Uehara M, Mulvaney P. (2002). Preparation of CdSe nanocrystals in a micro-flow-reactor. *Chemical Communications*, 0(23), 2844-2845.

152. Nagy KD, Jensen KF. (2011). Catalytic processes in small scale flow reactors status and opportunities. *Chimica oggi/Chemistry Today,* 29(4).

153. Navarro, O.C., Canos, A.C., and Chornet, S.I. (2009). Chemicals from Biomass: Aerobic Oxidation of 5-Hydroxymethyl-2-Furaldehyde into Diformylfurane Catalyzed by Immobilized Vanadyl-Pyridine Complexes on Polymeric and Organofunctionalized Mesoporous Supports. *Top Catal.*, 52, 304 – 314.

154. Navin, C.V., Krishna, K.S., Theegala, C., Kumar, C.S.S.R. (2014). Lab-on-a-chip devices for gold nanoparticle synthesis and their role as a catalyst support for continuous flow catalysis. *Nanotechnol Rev*, 3(1): 39 – 63.

155. Newman SG, Jensen KF. (2013). The role of flow in green chemistry and engineering. Green chemistry. *Green Chem.*,15, 1456-1472.

156. Ni W, Kou X, Yang Z, Wang J. (2008). Tailoring Longitudinal Surface Plasmon Wavelengths, Scattering and Absorption Cross Sections of Gold Nanorods. *ACS Nano,* 2(4), 677-686.

157. Nie X, Qian H, Ge Q, Xu H, Jin R. (2012). CO Oxidation Catalyzed by Oxide-Supported Au25(SR)18 Nanoclusters and Identification of Perimeter Sites as Active Centers. *ACS Nano,* 6(7), 6014–6022.

158. Nikoobakht B, El-Sayed MA. (2003). Preparation and Growth Mechanism of Gold Nanorods (NRs) Using Seed-Mediated Growth Method. *Chemistry of Materials*, 15(10), 1957-1962.

159. Niranjan, M. K.; Chakraborty, J. (2012). Synthesis of oxidation resistant copper nanoparticles in aqueous phase and efficient phase transfer of particles using alkanethiol. *Colloids Surf., A,* 407, 58−63.

160. O'Malley, B., and Snook, I. (2003). Crystal nucleation in the hard sphere system. *Phys. Rev. Lett.,* 90(8), 085702-1 - 085702-2.

161. Orendorff CJ, Murphy CJ. (2006). Quantitation of Metal Content in the Silver-Assisted Growth of Gold Nanorods. *The Journal of Physical Chemistry B,* 110(9), 3990-3994.

162. Oyanagi, H., Sun, Z.H., Jiang, Y., Uehara, M., Nakamura, H., Yamashita, K., Zhang, L., Lee, C., Fukano, A., and Maeda, H. (2011). In situ XAFS experiments using a microfluidic cell: Application to initial growth of CdSe nanocrystals. *J. Synchrotron Radiat.,* 18, 272–279.

163. Pan M, Brush AJ, Pozun ZD, Ham HC, Yu WY, Henkelman G, Hwang GS, Mullins CB. (2013). Model studies of heterogeneous catalytic hydrogenation reactions with gold. *Chem. Soc. Rev.,* 42, 5002-5013

164. Parak, W. J., Gerion, D., Pellegrino, T., Zanchet, D., Micheel, C., Williams, S.C., Boudreau, R., Le Gros, M.A., Larabell, C.A., and Alivisatos, A.P. (2003). Biological applications of colloidal nanocrystals. *Nanotechnology*, 14, R15-R27.

165. Parsapour, F.; Kelley, D.F.; Williams, R. S. (1998). Spectroscopy of Eu3+-Doped Pt(DMSA) Nanoclusters. *J. Phys. Chem. B,* 102, 7971-7977.

166. Partenheimer, W., and Grushin, V. (2011). Synthesis of 2,5-Diformylfuran and Furan-2,5-Dicarboxylic Acid by Catalytic Air-Oxidation of 5-Hydroxymethylfurfural. Unexpectedly SelectiveAerobic Oxidation of Benzyl Alcohol to Benzaldehyde with Metal=Bromide Catalysts. *Adv. Synth. Catal.*, 343, 102 - 111.

167. Pasini, T., Piccinini, M., Blosi, M., Bonelli, R., Albonetti, S., Dimitratos, N., Lopez-Sanchez, J.A., Sankar, M., He, Q., Kiely, C.J., Hutchings, G.J., and Cavani, F. (2011). Selective oxidation of 5-hydroxymethyl-2-furfural using supported gold–copper nanoparticles. *Green Chem.,* 13, 2091 - 2099

168. Pecoraor, T. A.; Chianelli, R. R. (1981). Hydrodesulfurization Catalysis by Transition Metal Sulfides. *J. Catal.,* 67, 2, 430-445.

169. Pedro SG, Puyol M, Izquierdo D, Salinas I, Alonso J. (2010). Synthesis of MUA-protected gold nanoparticles in microfluidic devices with in situ UV-vis. Characterization. *Ibersensor,* 9-11.

170. Phillips, T.W., Lignos, I.G., Maceiczyk, R.M., DeMello, A.J., and DeMello, J.C. (2014). Nanocrystal synthesis in microfluidic reactors: Where next? *Lab Chip,* 14, 3172-3180.

171. Pileni, M. P.; Lisiecki, I. (1993). Nanometer metallic copper particle synthesis in reverse micelles. *Colloids Surf., A,* 80, 63−68

172. Polshettiwar V, Luque R, Fihri A, Zhu H, Bouhrara M, Basset JM. (2011). Magnetically Recoverable Nanocatalysts. *Chemical Reviews,* 111(5), 3036-3075.

173. Polte J, Erler R, Thünemann AF, Sokolov S, Ahner TT, Rademann K, Kraehnert R. (2010). Nucleation and Growth of Gold Nanoparticles Studied via in situ Small Angle X-ray Scattering at Millisecond Time Resolution. *ACS Nano,* 4(2), 1076-1082.

174. Porel S, Singh S, Radhakrishnan TP. (2005). Polygonal gold nanoplates in a polymer matrix. *Chemical Communications,* 0(18), 2387-2389.

175. Powell MS, Slater NKH. (1983). The deposition of bacterial cells from laminar flows onto solid surfaces. *Biotechnology and bioengineering,* 891-900.

176. Protasova LN, Rebrov EV, Skelton HE, Wheatley AEH, Schouten JC. (2011). A kinetic study of the liquid-phase hydrogenation of citral on Au/TiO2 and Pt–Sn/TiO2 thin films in capillary microreactors. *Applied Catalysis A: General,* 399(1–2), 12-21.

177. Qian H, Jin R. (2009). Controlling Nanoparticles with Atomic Precision: The Case of $Au_{144}(SCH_2CH_2Ph)_{60}$. *Nano Lett., 9*, 4083–4087

178. Qian H, Zhu Y, Jin R. (2012). Atomically Precise Gold Nanocrystal Molecules with Surface Plasmon Resonance. *Proc. Natl. Acad. Sci. USA, 109*, 696–700

179. Qian H, Zhu M, Wu Z, Jin R. (2012). Quantum Sized Gold Nanoclusters with Atomic Precision. *Acc. Chem. Res., 45*, 1470–1479.

180. Rahimpour MR, Pourazadi E, Iranshahi D, Bahmanpour AM. (2011). Methanol synthesis in a novel axial-flow, spherical packed bed reactor in the presence of catalyst deactivation. *Chemical Engineering Research and Design,* 89(11), 2457-2469.

181. Ratner DM, Murphy ER, Jhunjhunwala M, Snyder DA, Jensen KF, Seeberger PH. (2005). Microreactor-based reaction optimization in organic chemistry-glycosylation as a challenge. *Chemical Communications,* 0(5), 578-580.

182. Richards, R., Koodali, R., Klabunde, K., and Erickson, L. (2011). Nanoscale Materials in Chemistry: Environmental Application. *ACS Publications: Washington DC*.

183. Roumanie M, Delattreb C, Mittler F, Marchandb G, Meille V, De Bellefonc C, Pijolata C, Tourniera G, Pouteau P. (2008). Enhancing surface activity in silicon microreactors: Use of black silicon and alumina as catalyst supports for chemical and biological applications. *Chemical Engineering Journal,* 135, Supplement 1(0): S317-S326.

184. Rudolph M, Hashmi ASK. (2012). Gold catalysis in total synthesis – an update. *Chem. Soc. Rev.,* 41, 2448-2462.

185. Sachse A, Galarneau A, Coq B, Fajula F. (2011). Monolithic flow microreactors improve fine chemicals synthesis. *New Journal of Chemistry,* 35(2), 259-264.

186. Saha, B., Dutta, S., and Abu-Omar, M.M. (2012). Aerobic oxidation of 5-hydroxylmethylfurfural with homogeneous and nanoparticulate catalysts. *Catal. Sci. Technol.,* 2, 79 – 81

187. Saliba, N., Parker, D.H., and Koel, B.E. (1998). Adsorption of oxygen on Au(111) by exposure to ozone. *Surf Sci.,* 410, 270-282.

188. Sau TK, Murphy CJ. (2004). Seeded High Yield Synthesis of Short Au Nanorods in Aqueous Solution. *Langmuir,* 20(15), 6414-6420.

189. Sault, A.G., Madix, R.J., and Campbell, C.T. (1986). Adsorption of oxygen and hydrogen on Au(110)-(1×2). *Surf Sci.,* 169, 347-356.

190. Schmid, G. (2012). Nanoparticles: From Theory to Application, 2nd ed., *Wiley-VCH: Weinheim.*

191. Schwarz, B., Reininger, P., Ristanic, D., Detz, H., Andrews, A.M., Schrenk,W., and Strasser, G. (2014). Monolithically integrated mid-infrared lab-on-a-chip using plasmonics and quantum cascade structures. *Nature Communications,* 5(4085), 1-7.

192. Sear, R. P. (2006). Heterogeneous and homogeneous nucleation compared: rapid nucleation on microscopic impurities. *J. Phys. Chem. B.,* 110(10), 4985-4989.

193. Seker E, Gulari E. (2002). Single step sol–gel made gold on alumina catalyst for selective reduction of NOx under oxidizing conditions: effect of goldprecursor and reaction conditions. *Applied Catalysis A: General,* 232, 203–217.

194. Serna P, Boronat M, Corma A. (2011). Tuning the Behavior of Au and Pt Catalysts for the Chemoselective Hydrogenation of Nitroaromatic Compounds. *Topics in Catalysis,* 54(5-7), 439-446.

195. Shaikhutdinov SK, Meyer R, Naschitzki M, Bäumer M, Freund HJ. (2003). Size and Support Effects for CO Adsorption on Gold Model Catalysts. *Catalysis Letters,* 86(4), 211-219.

196. Shalom D, Wootton RCR, Winkle RF, Cottam BF, Vilar R, DeMello AJ, Wilde CP. (2007). Synthesis of thiol functionalized gold nanoparticles using a continuous flow microfluidic reactor. *Materials Letters,* 61(4–5), 1146-1150.

197. Shan C, Han D, Song J, Ivaska A, Niu L. (2010). Flowerlike submicrometer gold particles: Size- and surface roughness-controlled synthesis and electrochemical characterization. *Journal of Materials Research,* 25(09), 1755-1760.

198. Si S, Leduc C, Delville MH, Lounis B. (2010). Short Gold Nanorod Growth Revisited: The Critical Role of the Bromide Counterion. *ChemPhysChem,* 13(1), 193-202.

199. Singh, M.; Sinha, I.; Premkumar, M.; Singh, A. K.; Mandal, R. K. (2010). Structural and surface plasmon behavior of Cu nanoparticles using different stabilizers. *Colloid Surf., A,* 359, 88−94.

200. Siwach, O. P.; Sen, P. (2008). Synthesis and study of fluorescence properties of Cu nanoparticles. *J. Nanopart. Res.,* 10, 107−114.

201. Siyo, B., Schneider, M., Radnik, J., Pohl, M., Langer, P., and Steinfeldt, N. (2014). Influence of support on the aerobic oxidation of HMF into FDCA overpreformed Pd nanoparticle based materials. *Applied Catalysis A: General*, 478, 107–116.

202. Song Y, Kumar CSSR, Hormes J. (2004). Synthesis of Pd nanoparticles using a continuous flow polymeric micro reactor, *Journal of Nanoscience and nanotechnology*, 4(7), 788-793.

203. Song Y, Doomes EE, Prindle J, Tittsworth R, Hormes J, Kumar CSSR. (2005). Investigations into Sulfobetaine-Stabilized Cu Nanoparticle Formation: Toward Development of a Microfluidic Synthesis. *The Journal of Physical Chemistry B,* 109(19), 9330-9338.

204. Song JH, Kim F, Kim D, Yang P. (2005). Crystal overgrowth on gold nanorods: tuning the shape, facet, aspect ratio, and composition of the nanorods. *Chemistry,* 11(3), 910-916.

205. Song Y, Hormes J, Kumar CSSR. (2008). Microfluidic Synthesis of Nanomaterials. *Small,* 4(6), 698-711.

206. Sournat, T.L., Safier, P.A., Voigt, J.A., Hoyt, J., Tallant, D.R., Matzke, C.M., and Michalske, T.A. (2007). Spatially-resolved analysis of nanoparticle nucleation and growth in a microfluidic reactor. *Lab Chip,* 7, 908–915.

207. Spivey, J.J., Krishna, K.S., Kumar, C.S.S.R., Dooley, K.M., Flake, J.C., Haber, L.H., Xu, Y., Janik, M.J., Sinnott, S.B., Cheng, Y., Liang, T., Sholl, D.S., Manz, T.A., Diebold, U., Parkinson, G.S., Bruce, D.A., and De Jongh, P. (2014). Synthesis, Characterization, and Computation of Catalysts at the Center for Atomic-Level Catalyst Design. *J. Phys. Chem. C, 118* (35), 20043 – 20069.

208. Stratakis M, Garcia H. (2012). Catalysis by Supported Gold Nanoparticles: Beyond Aerobic Oxidative Processes. *Chemical Reviews,* 112(8), 4469-4506.

209. Stubenrauch M, Fischer M, Kremin C, Stoebenau S, Albrecht A, Nagel O. (2006). Black silicon—new functionalities in microsystems. *Journal of Micromechanics and Microengineering,* 16(6): S82-S87.

210. Sun X, Dong S, Wang E. (2005). One-step preparation of highly concentrated well-stable gold colloids by direct mix of polyelectrolyte and HAuCl4 aqueous solutions at room temperature. *Journal of Colloid and Interface Science,* 288(1), 301-303.

211. Sun Y, Xia Y. (2002). Shape-controlled synthesis of gold and silver nanoparticles. *Science,* 298, 2176-2179.

212. Sweeney SF, Woehrle GH, Hutchison JE. (2006). Rapid Purification and Size Separation of Gold Nanoparticles via Diafiltration. *Journal of the American Chemical Society,* 128(10), 3190-3197.

213. Takagi M, Maki T, Miyahara M, Mae K. (2004). Production of titania nanoparticles by using a new microreactor assembled with same axle dual pipe. *Chemical Engineering Journal,* 101(1–3), 269-276.

214. Taniike T, Tada M, Coquet R, Morikawa Y, Sasaki T, Iwasawa Y. (2007). A new aspect of heterogeneous catalysis: Highly reactive cis-$(NO)_2$ dimer and Eley–Rideal mechanism for NO–CO reaction on a Co-dimer/γ-alumina catalyst. *Chemical Physics Letters,* 443(1–3), 66-70.

215. Teste, B., Malloggi, F., Gassner, A., Georgelin, T., Siaugue, J., Varenne, A., Giraultc, H., and Descroix, S. (2011). Magnetic core shell nanoparticles trapping in a microdevice generating high magnetic gradient. *Lab Chip,* 11, 833-840.

216. Thomas, J. M. and Thomas, W.J. (1997). *Principle and practice of heterogeneous catalysis*.

217. Thompson DT. (2007). Using gold nanoparticles for catalysis. *Nano Today,* 2(4): 40-43.

218. Topsøe, H.; Clausen, B.S.; Massoth, F.E.; Anderson, J.R.; Boudart, M. (1996). (Eds.), Catalysis Science and Technology, vol. 11, *Springer-Verlag, New York.*

219. Torigoe K, Watanabe Y, Endo T, Sakai K, Sakai H, Abe M. (2010). Microflow reactor synthesis of palladium nanoparticles stabilized with poly(benzyl ether) dendron ligands. *Journal of Nanoparticle Research,* 12(3), 951-960.

220. Toste D. (2011). Gold catalysis for organic synthesis. *Beilstein J. Org.Chem.,* 7, 553–1525.

221. Tosti S, Basileb A, Chiappettab G, Rizzelloc C, Violantea V. (2003). Pd–Ag membrane reactors for water gas shift reaction. *Chemical engineering journal,* 93, 23-30.

222. Toyota, A., Nakamura, H., Ozono, H., Yamashita, K., Uehara, M., and Maeda, H. (2010). Combinatorial Synthesis of CdSe Nanoparticles Using Microreactors. *J. Phys. Chem. C,* 114, 7527–7534.

223. Tsunoyama H, Ichikuni N, Tsukuda T. (2008). Microfluidic Synthesis and Catalytic Application of PVP-Stabilized, ∼1 nm Gold Clusters. *Langmuir,* 24(20), 11327-11330.

224. Turner M, Golovko VB, Vaughan OPH, Abdulkin P, Berenguer-Murcia A, Tikhov MS, Johnson BFG, Lambert RM. (2008). Selective oxidation with dioxygen by gold nanoparticle catalysts derived from 55-atom clusters. *Nature,* 454, 981-983.

225. Valden M, Lai X, Goodman DW. (1998). Onset of Catalytic Activity of Gold Clusters on Titania with theAppearance of Nonmetallic Properties. *Science,* 281, 1647-1650.

226. Vazquez-Vazquez, C.; Banobre-Lopez, M.; Mitra, A.; Arturo Lopez-Quintela, M.; Rivas, J. (2009). Synthesis of small atomic copper clusters in microemulsions. *Langmuir,* 25, 8208−8216.

227. Viefhues, M., Eichhorn, R., Fredrich,E., Regtmeiera, J., and Anselmettia, D. (2012). Continuous and reversible mixing or demixing of nanoparticles by dielectrophoresis. *Lab Chip,* 12, 485-494.

228. Wagner J, Kirner T, Mayer G, Albert J, Köhler JM. (2004). Generation of metal nanoparticles in a microchannel reactor. *Chemical Engineering Journal,* 101(1–3), 251-260.

229. Wagner J., Köhler, J. M. (2005). Continuous Synthesis of Gold Nanoparticles in a Microreactor. *Nano Letters,* 5(4), 685-691.

230. Wagner J, Tshikhudo TR, Köhler JM. (2005). Microfluidic generation of metal nanoparticles by borohydride reduction. *Chemical Engineering Journal,* 135, Supplement 1(0), S104-S109

231. Walter E, Pronzato L, Soong Y, Otarod M, Happel J. (1995). Modeling Transient Tracing in Plug-Flow Reactors: A Case Study. *Industrial & Engineering Chemistry Research,* 34(2), 483-487.

232. Wang, J., Koel, B.E. (1998). IRAS studies of NO_2, N_2O_3 and N_2O_4 adsorbed on Au(111) surfaces and reactions with coadsorbed H_2O. *J. Phys. Chem. A.,* 102, 8573-8579.

233. Wang L, Yang P, Li Y, Chen H, Li M, Luo F. (2007). A flow injection chemiluminescence method for the determination of fluoroquinolone derivative using the reaction of luminol and hydrogen peroxide catalyzed by gold nanoparticles. *Talanta,* 72(3), 1066-1072.

234. Wang N, Matsumoto T, Ueno M, Miyamura H, Kobayashi S. (2009). A Gold-Immobilized Microchannel Flow Reactor for Oxidation of Alcohols with Molecular Oxygen. *Angewandte Chemie International Edition,* 48(26), 4744-4746.

235. Wang, L., McCleese, C., Kovalsky, A., Zhao,Y., and Burda, C. (2014). Femtosecond time-resolved transient absorption spectroscopy of $CH_3NH_3PbI_3$ perovskite films: Evidence for passivation effect of PbI_2. *J. Am. Chem. Soc.*, 136, 12205−12208.

236. Waseda, Y., and Muramatsu, A. (2004). Morphology control of materials and nanoparticles advanced materials processing and characterization. *Series: Springer Series in Materials Science,* XV, 262.

237. Watzky, M. A.; Finke, R. G. (1997). Nanocluster Size-Control and "Magic Number" Investigations, Experimental Tests of the "Living-Metal Polymer" Concept and of Mechanism-Based Size-Control Predictions Leading to the Syntheses of Iridium (0) Nanoclusters Centering About Four Sequential Magic Numbers. *Chemistry of Materials*, 9, 3083-3095.

238. Watzky, M. A.; Finke, R. G. (1997). Transition Metal Nanocluster Formation Kinetic and Mechanistic Studies. A New Mechanism When Hydrogen Is the Reductant: Slow, Continuous Nucleation and Fast Autocatalytic Surface Growth. *Journal of the American Chemical Society*, 119, 10382-10400.

239. Wei, W.; Lu, Y.; Chen, W.; Chen, S. (2011). One-pot synthesis, photoluminescence, and electrocatalytic properties of subnanometersized copper clusters. *J. Am. Chem. Soc.*, 133, 2060−2063.

240. Weisser, O.; Landa, S. (1973). Sulfide Catalysts Their Properties and Applications, *Pergamon Press, New York,*.

241. Werpy, T., Holladay, J., White, J., Peterson, G., Bozell, JJ., Aden, A., and Manheim, A. (2004). Top value added chemicals from biomass. Vol 1, Results of screening for potential candidates from sugars and synthetic gas. *U.S. Department of Energy, NREL/TP-510-35523.*

242. Wu Z, MacDonald M, Chen J, Zhang P, Jin R. (2011). Kinetic Control and Thermodynamic Selection in the Synthesis of Atomically Precise Gold Nanoclusters. *J. Am. Chem. Soc*., *133*, 9670–9673.

243. Wu P, Loh KP, Zhao XS. (2011). Supported Gold Catalysts for Selective Oxidation of Organics. *Science of Advanced Materials*, 3(6), 970-983.

244. Xia, Y., Xiong, Y., Lim, B., and Skrabalak, S.E. (2009). Shape-controlled synthesis of metal nanocrystals: simple chemistry meets complex physics? *Angew Chem Int Ed Engl.*, 48 (1), 60–103.

245. Yang SY, Cheng FY, Yeh CS, Lee GB. (2010). Size-controlled synthesis of gold nanoparticles using a micro-mixing system. *Microfluid Nanofluid*, 8, 303–311

246. Yue, J., Schouten, J.C., and Nijhuis, T.A. (2012). Integration of Microreactors with Spectroscopic Detection for Online Reaction Monitoring and Catalyst Characterization. *Ind. Eng. Chem. Res., 51* (45), 14583–14609

247. Yuet KP, Hwang DK, Haghgooie R, Doyle PS. (2009). Multifunctional Superparamagnetic Janus Particles. *Langmuir*, 26(6), 4281-4287.

248. Zhang P, Zhang B, Shi R. (2009). Catalytic decomposition of low level ozone with gold nanoparticles supported on activated carbon. *Front. Environ. Sci. Engin. China,* 3(3), 281–288

249. Zhang W, Xu S, Han X, Bao X. (2012). In situ solid-state NMR for heterogeneous catalysis: a joint experimental and theoretical approach. *Chemical Society Reviews,* 41(1), 192-210.

250. Zhang H, Toshima N. (2013). Glucose oxidation using Au-containing bimetallic and trimetallic nanoparticles. *Catalysis Science & Technology,* 3(2), 268-278.

251. Zhang, Z., Liu, B., Lv, K., Sun, J., and Deng, K. (2014). Aerobic oxidation of biomass derived 5-hydroxymethylfurfural into 5-hydroxymethyl- 2-furancarboxylic acid catalyzed by a montmorillonite K-10 clay immobilized molybdenum acetylacetonate complex. *Green Chem.*, 16, 2762 - 2770

252. Zhu Y, Qian H, Drake BA, Jin R. (2010). Atomically Precise $Au_{25}(SR)_{18}$ Nanoparticles as Catalysts for Selective Hydrogenation of α, β-Unsaturated Ketones and Aldehydes. *Angew. Chem. Int. Ed., 49,* 1295–1298

253. Zhu Y, Qian H, Jin R. (2010). An atomic-level strategy for unraveling gold nanocatlaysis from the perspective of $Au_n(SR)_m$ nanoclusters. *Chem. Eur. J.,* 16, 11455-11462

254. Zhu Y, Qian H, Jin R. (2011). Catalysis Opportunities of Atomically Precise Gold Nanoclusters. *J. Mater. Chem., 21,* 6793–6799.

255. Zinoveva, S., De Silva, R., Louis, R.D., Datta, P., Kumar, C.S.S.R., Goettert, J., and Hormes, J. (2007). The wet chemical synthesis of Co nanoparticles in a microreactor system: A time-resolved investigation by X-ray absorption spectroscopy. *Nuclear Instruments and Methods in Physics Research A,* 582, 239–241

APPENDIX

Total no. of Moles = Concentration * Volume of the sample collected

HPLC data for the control experiment carried out with HMFCA as the initial reactant:

	HMFCA		FDCA	
Experiment Time (h)	Peak area	Concentration (mM)	Peak area	Concentration (mM)
t = 0	1452618	1.44	0	0
t = 24	1302451	1.32	0	0

HPLC data for the control experiment carried out with HMF as the initial reactant:

	HMF		HMFCA		FDCA	
Experiment Time (h)	Peak area	Concentration (mM)	Peak area	Concentration (mM)	Peak area	Concentration (mM)
t = 0	313928	1.71	0	0	0	0
t = 24	242761	1.39	0	0	0	0

HPLC data for oxidation of HMF using millifluidic reactor:

Volume of sample collected at 10, 20, 30, 40, 50 minutes = 0.016, 0.033, 0.05, 0.066, 0.083 ml

	HMF		**HMFCA**			**FDCA**		
Sample	**Peak area**	**Conc. (mM)**	**Peak area**	**Conc. (mM)**	**Total Moles of product**	**Peak area**	**Conc. (M)**	**Total Moles of product**
ZONE 1 (10 min)	2673	0.349	15549	0.302	$4.83*10^{-9}$	NA	0	NA
ZONE 2 (20 min)	6410	0.355	30269	0.314	$1.03*10^{-8}$	3762	0.0106	$3.49*10^{-10}$
ZONE 3 (30 min)	3941	0.365	35273	0.318	$1.59*10^{-8}$	11647	0.0418	$2.09*10^{-9}$
ZONE 4 (40 min)	NA	NA	43511	0.324	$2.13*10^{-8}$	55491	0.05	$3.3*10^{-9}$
End (50 min)	NA	NA	16489	0.303	$2.51*10^{-8}$	155399	0.113	$9.37*10^{-9}$

HPLC data for oxidation of HMF using batch reactor:

Volume of sample = 15 ml

	HMF		**HMFCA**			**FDCA**		
Sample	**Peak area**	**Conc. (mM)**	**Peak area**	**Conc. (mM)**	**Total Moles of product**	**Peak area**	**Conc. (M)**	**Total Moles of product**
0 h		3	NA	NA	NA	NA	NA	NA
1 h	32161	0.478	1001498	0.369	$5.53*10^{-6}$	34143	0.0266	$3.99*10^{-7}$
2 h	NA	NA	46576	0.326	$4.89*10^{-6}$	126780	0.0924	$1.38*10^{-6}$
4 h	NA	NA	28135	0.312	$4.68*10^{-6}$	131353	0.0956	$1.43*10^{-6}$
6 h	NA	NA	24264	0.309	$4.63*10^{-6}$	138279	0.1006	$1.50*10^{-6}$
24 h	NA	NA	NA	NA	NA	152525	0.1107	$1.66*10^{-6}$

Calculation of Active sites of coated Au catalyst within the millifluidic reactor channel wall:

Surface area of Coated Au nanostructures:
Top surface area: $2.2*10^{-5}$ m^2
Left Side surface area: $6.05*10^{-6}$ m^2
Right Side surface area: $6.05*10^{-6}$ m^2
Length of the gold catalyst coated within the millifluidic chip reactor: $22*10^{-2}$ m
Height of the gold catalyst coated within the millifluidic chip reactor: $27.5*10^{-6}$ m
Breadth of the gold catalyst coated within the millifluidic chip reactor: $100*10^{-6}$ m
Length and breadth occupied by the gold atom = $3.48*10^{-10}$ m

No. of Au atoms on top surface
= (Breadth of the gold catalyst coated within the millifluidic chip reactor / Length and breadth occupied by the gold atom) + (Length of the gold catalyst coated within the millifluidic chip reactor / Length and breadth occupied by the gold atom)
= ($100*10^{-6}$ m / ($3.48*10^{-10}$ m)) + ($22*10^{-2}$ m / ($3.48*10^{-10}$ m)) = $1.81*10^{14}$ atoms

No. of Au atoms on right side surface
= (Height of the gold catalyst coated within the millifluidic chip reactor / Length and breadth occupied by the gold atom) + (Height of the gold catalyst coated within the millifluidic chip reactor / Length and breadth occupied by the gold atom)
= ($27.5*10^{-6}$ m) / ($3.48*10^{-10}$ m) + ($22*10^{-2}$ m / ($3.48*10^{-10}$ m)) = $4.99*10^{13}$ atoms

No. of Au atoms on left side surface
= (Height of the gold catalyst coated within the millifluidic chip reactor / Length and breadth occupied by the gold atom) + (Height of the gold catalyst coated within the millifluidic chip reactor / Length and breadth occupied by the gold atom)
= ($27.5*10^{-6}$ m) / ($3.48*10^{-10}$ m) + ($22*10^{-2}$ m / ($3.48*10^{-10}$ m)) = $4.99*10^{13}$ atoms

Total no. of atoms exposed = No. of Au atoms on top surface + No. of Au atoms on right side surface + No. of Au atoms on left side surface = $2.80*10^{14}$ atoms

Therefore the total no. of active sites of coated Au catalyst within the millifluidic reactor channel wall = $2.80*10^{14}$

Calculation of active sites of Au nanocatalyst prepared using batch reactor:

Catalyst mass = 5 mg = 0.005 g
Molecular weight of Au = 196.96 g/mol (196.96 amu, 1 amu = $1.66*10^{-24}$ g)
Active sites = Catalyst mass*(1/molecular wt. of catalyst)*(Avagadro number)
Active sites = 0.005 g * ($5.07*10^{-3}$ mol/g)*($6.023*10^{23}$ atoms/mol)
Maximum Active sites = $1.52*10^{19}$

Radius of the Au nanoparticle = 1 nm
Surface area of the Au nanoparticle = $4\pi r^2 = 4*3.14*(1*10^{-9}\ m)^2 = 1.256*10^{-17}$ m^2

Projected area of the Au atom = πr^2 = 3.14*(174*10^{-12} m)^2 = 9.50*10^{-20} m^2
Total no. of surface atoms in Au nanoparticle: 1.256*10^{-17} m^2/9.50*10^{-20} m^2 = 132.2 atoms

Volume of the Au nanoparticle = (4/3) πr^3 = (4/3)*3.14*(1*10^{-9})^3 = 4.18*10^{-27} m^3
Volume of the Au atom = (4/3) πr^3 = (4/3)*3.14*(174*10^{-12})^3 = 2.20*10^{-29} m^3
Total no. of atoms in Au nanoparticle: Volume of the Au nanoparticle/Volume of Au atom = 4.18*10^{-27} m^3/2.20*10^{-29} m^3 = 190 atoms

Dispersion of Au atoms = Total no. of surface atoms in Au nanoparticle / Total no. of atoms in Au nanoparticle = 69.5%

Total active sites: Maximum active sites*dispersion = 1.52*10^{19} * 0.695 = 1.05*10^{19}

Reaction rate:
Reaction rate = (Final concentration of product - initial concentration of product)/Time

Turnover frequency:
Turnover frequency = Total no. of moles of product at the specific time/(Active sites of the catalyst * Time of the reaction)

Millifluidic reactor at T = 50 minutes:
HMFCA Turnover frequency **= (**Total. no. of moles of HMFCA + Total no. of moles of FDCA)/ /(Active sites of the catalyst * Time of the reaction)
HMFCA Turnover frequency = **(**2.51*10^{-8} + 9.37*10^{-9})/((2.80*10^{14})*(50*60)) = 4.10*10^{-26} molecules s^{-1}
FDCA Turnover frequency **= (**Total no. of moles of FDCA)/ /(Active sites of the catalyst * Time of the reaction)
FDCA Turnover frequency = 9.37*10^{-9}/((2.80*10^{14})*(50*60)) = 1.11*10^{-26} molecules s^{-1}

Batch reactor at T = 50 minutes:
HMFCA Turnover frequency **= (**Total. no. of moles of HMFCA + Total no. of moles of FDCA)/ /(Active sites of the catalyst * Time of the reaction)
HMFCA Turnover frequency = (5.53*10^{-6} + 3.99*10^{-7})/((1.05*10^{19})*(50*60)) = 1.87*10^{-28} molecules s^{-1}
FDCA Turnover frequency **= (**Total no. of moles of FDCA)/ /(Active sites of the catalyst * Time of the reaction)
FDCA Turnover frequency **=** 3.99*10^{-7}/((1.05*10^{19})*(50*60)) = 1.26*10^{-29} molecules s^{-1}

VITA

Chelliah V. Navin was born in Chennai, India. He graduated in May 2009 with a Bachelor of Technology in Biotechnology from Karunya University, Coimbatore. Upon graduation, Navin worked as a Project Associate in the Dept. of Biotechnology at Indian Institute of Technology, Madras until July 2010. Navin concluded his work at IIT Madras to pursue his Master's degree in Chemical Engineering at Illinois Institute of Technology, Chicago in August 2010. He later transferred to Louisiana State University, Baton Rouge in January 2011 and pursued his research at the Center for Advanced Microstructures & Devices (CAMD) and graduated with a Master of Science by research in Biological and Agricultural Engineering in December 2012. Navin continued his research further at CAMD to pursue his Doctorate of Philosophy (Ph.D.) in Engineering Sciences with a major concentration in Biological Engineering and minors in Chemical Engineering and Chemistry at Louisiana State University, Baton Rouge. Navin will receive his Ph.D. in August 2015. His technical interests include Catalysis, Nanomaterials, Lab-on-a-Chip devices, In-situ time resolved investigations, Bio-Energy and Bio-Chemical Engineering.